Fast Neutron Scattering Analysis

by

Andy Buffler

Thesis presented for the degree of
Doctor of Philosophy
in the
Department of Physics
Faculty of Science
University of Cape Town

September 1998

Abstract

The scattering of a beam of fast monoenergetic neutrons is used to determine elemental compositions of small (0.2-1 kg) samples of materials. Particular emphasis is placed on the measurement of concentrations of the elements H, C, N and O, which are the principal constituents of contraband materials, such as explosives and narcotics. Scattered neutrons are detected by liquid scintillators located at forward and at backward angles, and different elements are identified by their characteristic scattering signatures derived either from a combination of time-of-flight and pulse height measurements or from pulse height measurements alone. Atom fractions for H, C, N, O and other elements are derived from unfolding analyses based on these scattering signatures and used to identify materials. Effects of neutron interactions in surrounding materials, either in the neutron beam or between the scatterer and the detectors, can be detected and allowed for in such a way as not to interfere significantly in the identification of the scatterer. The Fast Neutron Scattering Analysis technique provides a non-intrusive method for detecting and identifying sub-kilogram quantities of contraband materials. Methods for locating the positions of small contraband items in packages of volume up to about 0.5 m^3 are described and a two-stage screening system for detecting contraband hidden in small packages is proposed.

Acknowledgements

I thank my project supervisor and mentor, Frank Brooks, for his selfless assistance and guidance, constant encouragement throughout this work, and friendship; and for teaching me not to compromise in the pursuit of excellence.

In addition, I wish to express my gratitude to the following people:

David Aschman for his supervision, motivation and support;

Saalih Allie for his friendship and help with the experiments;

Krish Bharuth-Ram, Rudolph Nchodu and Mark Herbert, for their contributions to the running of the experiments; and also Sandy Perez, Roger Fearick, Peter Binns and Bruce Simpson;

The staff of the National Accelerator Centre, in particular René Pretorius for always welcoming us to the VDG, Karl Springhorn and his beam team, and Lawrence Ashworth;

Manfred Matzke of Physikalisch-Technische Bundesanstalt, Braunschweig, Germany, for supplying me with the HEPRO codes and assisting with their initial use;

The staff of the UCT Physics workshops: Danie Momsen, Dave Boulton, Graeme Fowle, Leon van Heerden and Kerwin Ontong;

My parents Cedric and Margie, and brother Simon, who need to be held at least partly responsible for the way I have turned out;

and my dear wife Paula, (temporary) Neutron Physics Widow, for putting up with far more than could reasonably be expected during the completion of this work.

This work was funded by the International Atomic Energy Agency's Co-ordinated Research Programme on 'Bulk Hydrogen Analysis, using Neutrons', and by the Foundation for Research Development (South Africa).

Contents

Appendices

List of figures

List of Tables

Chapter 1

Non-intrusive characterization using neutrons

Techniques for non-destructive screening and elemental characterization of bulk materials are of great practical importance in many industrial and commercial applications [Vo97]. There is a growing need for methods of non-invasive inspection of objects of all shapes and sizes. The situations in which these techniques need to be applied include the scanning of luggage and packages at airport terminals and other border posts for contraband such as narcotics and explosives, and trade regulation enforcement via shipping manifest verification by customs officials at freight depots. Other contexts include the non-intrusive examination of military ordnance, including conventional explosives, mines or chemical warfare agents; the on-line analysis of minerals such as coal, iron ore and oil; the characterization of foodstuffs at processing plants for the purposes of quality control; and the interrogation of nuclear or hazardous chemical waste-drums to support proper treatment and disposal of these materials. There is also a growing need to develop modern detection techniques to quickly scan the soil or waters of the earth for mines or other buried explosives.

In recent years, particular effort has been put into developing systems to detect and identify contraband, especially explosive material and narcotics, hidden in aircraft luggage or shipping containers [Kh91, Ma92, Vo94]. The smuggling of contraband has increased with the continuous growth in international travel and trade, and the threat of terror incidents is also ever present, many of which involve the placing of explosives in aircraft and other public places. The event that was particularly responsible [Sh90] for the increase in public pressure for governments to address this issue was the exploding of the bomb placed on Pan Am flight 103 shortly after take-off over Lockerbie, Scotland, in December 1988, killing 270 people. While it is theoretically possible to manually inspect every package, container or item of baggage passing across a border via an air, rail, or sea terminal or through a post office, such examination would be very costly in terms of wasted time and impeded commerce. For example, each year ports of entry in the United States process some 400 million passengers, 10 million cargo containers, 125 million cars and trucks, 450 thousand commercial aircraft, 100 thousand cargo ships and 170 thousand pleasure craft [Br94b]. Currently less than one percent of the two billion bags of airline luggage carried worldwide per annum are opened by security personnel. Furthermore, smugglers and terrorists frequently resort to the use of packages having hidden compartments or false bottoms which may be overlooked in even most careful inspection, as could contraband carefully hidden amongst a shipping container filled mainly with innocuous goods. The large volume of international traffic accentuates the problems associated with inspecting cargo for explosives and contraband at ports of entry. Modern, rapid systems are required for the effective inspection of containers of all shapes and sizes.

1.1 The elemental signatures of explosives and narcotics

Although there are more than 30 basic types of explosives which can be combined and diluted to make hundreds of variations [Ur84], most explosives consist almost exclusively of the elements H, C, N and O. Table 1-1 lists some common explosives together with their empirical chemical formulae and percentage atomic composition [Sa93a, Sh93]. The elements H, C, N and O are also found in different combinations in the various narcotics, a selection of which are listed in Table 1-2 [Si74, Sa93a, Sh93]. The ability to detect the presence of H, C, N and O and other elements in an inspected object is necessary but not sufficient for an inspection system to be effective. This stems from the fact that the key elements of interest for the detection of explosives and narcotics, i.e. H, C, N and O, are present in many common materials including foods, fabrics and polymers. A selection of everyday substances which consist only of these elements, their empirical formulae and percentage atomic composition is shown in Table 1-3 [Br94b, Sh93]. The ability of a system to distinguish explosives and narcotics from these common substances requires not only the identification of the *presence* of the elements H, C, N and O, but also a *measure* of the relative combinations of these elements. If the measurements are localized within the object under inspection, the elemental compositions determined for each volume element (voxel) may be used to form an image of the extended object. However, an object of large volume may dilute the required information with the result that the presence of the concealed substance could go unnoticed. Thus, an effective inspection system also has to be able to determine the relevant elemental distributions in the inspected sample so as to distinguish, with high selectivity, the contraband from the overwhelming majority of benign substances surrounding it.

Table 1-1 A selection of explosives, their empirical formulae and percentage atom fractions [Sa93a, Sh93]. Percentages in brackets are approximate and could depend on the ratio of the mixtures used.

Trade or popular name	***Chemical name / (Comment)***	***Empirical chemical formula***	***% atom fraction***			
			H	***C***	***N***	***O***
Ammo-Nite (AN)	Ammonium nitrate	$H_4N_2O_3$	44.4	0.0	22.2	33.3
EGDN	Ethylene glycol dinitrate	$H_4C_2N_2O_6$	28.6	14.3	14.3	42.9
HMX or Octogen	Cyclotetra-methylene tetranitramine	$H_8C_4N_8O_8$	28.6	14.3	28.6	28.6
Nitrocellulose		$H_7C_6N_3O_{10}$	26.9	23.1	11.5	38.5
Nitroglycerine (NG)	Glycerol trinitrate	$H_5C_3N_3O_9$	25.0	15.0	15.0	45.0
PETN	Pentaerythritol tetranitrate	$H_8C_5N_4O_{12}$	27.6	17.2	13.8	41.4
Picric acid	Trinitrophenol	$H_3C_6N_3O_7$	15.8	31.6	15.8	36.8
Research Division X (RDX)	Cyclotrimethylene trinitramine	$H_2CN_2O_2$	28.6	14.3	28.6	28.6
Tetryl	2,4,6,N-Tetranitro-N-methylanaline	$H_5C_7N_5O_8$	20.0	28.0	20.0	32.0
TNT	Trinitrotoluene	$H_5C_7N_3O_6$	23.8	33.3	14.3	28.6
Composition 4 (C-4)	(RDX with a plasticizer)	$(H_{16}C_8N_{11}O_{11})$	(34.8)	(17.4)	(23.9)	(23.9)
SEMTEX	(A variable mixture of RDX and PETN)	-	-	-	-	-
Composition B	(A 60:40:1 mixture of RDX:TNT:wax.)	$(H_{28}C_{23}N_{24}O_{30})$	(26.7)	(21.9)	(22.9)	(28.6)
Dynamite	(Commonly a mixture of EGDN and NG in a combustible pulp.)	$(H_{41}C_{12}N_{13}O_{38})$	(39.4)	(11.5)	(12.5)	(36.5)
Black powder	(Generally a mixture of sodium nitrate, sulphur and charcoal.)	-	-	-	-	-

Table 1-2 A selection of narcotics, their empirical formulae and percentage atom fractions [Si74, Sa93a, Sh93].

Popular name	***Empirical chemical formula***	***% atom fraction***			
		H	***C***	***N***	***O***
Cocaine	$H_{21}C_{17}NO_4$	48.8	39.5	2.3	9.3
Heroin	$H_{20}C_{17}NO$	51.3	43.6	2.6	2.6
LSD	$H_{25}C_{20}N_3O$	51.0	40.8	6.1	2.0
Mandrax	$H_{14}C_{16}N_2O$	42.4	48.5	6.1	3.0
Morphine	$H_{19}C_{17}NO_3$	47.5	42.5	2.5	7.5
PCP	$H_{51}C_{35}N_2$	58.0	39.8	2.3	0.0

Table 1-3 Some common materials, their empirical formulae and percentage atom fractions [Br94b, Sh93].

Popular name	***Empirical chemical formula***	***% atom fraction***			
		H	***C***	***N***	***O***
Ammonium acetate	$H_7C_2NO_2$	58.3	16.7	8.3	16.7
Acetamide	H_5C_2NO	55.6	22.2	11.1	11.1
Ethanol	H_6C_2O	66.7	22.2	0.0	11.1
Barley	$H_{52}C_{27}O_{22}$	51.5	26.7	0.0	21.8
Cotton	$H_{27}C_{18}O_{13}$	46.6	31.0	0.0	22.4
Dacron	$H_4C_5O_2$	36.4	45.5	0.0	18.2
Ethanol	H_6C_2O	66.7	22.2	0.0	11.1
Lucite (Perspex)	H_4C_2O	57.1	28.6	0.0	14.3
Melamine	$H_6C_3N_6$	40.0	20.0	40.0	0.0
Methanol	H_4CO	66.7	16.7	0.0	16.7
Neoprene	H_9C_{11}	45.0	55.0	0.0	0.0
Nylon	$H_{11}C_6NO$	57.9	31.6	5.3	5.3
Orlon	H_3C_3N	42.9	42.9	14.3	0.0
Paper	$H_{10}C_6O_5$	47.6	28.6	0.0	23.8
Polyester	H_2C_3O	33.3	50.0	0.0	16.7
Polyethylene	H_2C	66.7	33.3	0.0	0.0
Polyurethane	$H_{10}C_5N_2O$	55.6	27.8	11.1	5.6
PVC	H_3C_2	60.0	40.0	0.0	0.0
Rayon	$H_{10}C_6O_5$	47.6	28.6	0.0	23.8
Silk	$H_{13}C_8N_5O_4$	43.3	26.7	16.7	13.3
Soybean	$H_{36}C_{21}N_3O_{11}$	50.7	29.6	4.2	15.5
Sugar	$H_{24}C_{13}O_{12}$	49.0	26.5	0.0	24.5
Water	H_2O	66.7	0.0	0.0	33.3
Wood	$H_{31}C_{22}O_{12}$	47.7	33.8	0.0	18.5
Wool	H_3C_2NO	42.9	28.6	14.3	14.3

Explosives and narcotics are fortunately well-separated from most common materials in one or more elemental features. Figure 1-1 shows a stacked bar graph of the fraction of each constituent atom, as a percentage, for the explosives, narcotics and miscellaneous materials listed in Tables 1-1, 1-2 and 1-3, respectively. The figure shows that explosives are typically characterised by approximate H:C:N:O element fractions of 0.3 : 0.2 : 0.2 : 0.3, while the corresponding values for narcotics are about 0.5 : 0.4 : 0.05 : 0.05. Thus explosives are distinguished by relatively high proportions of nitrogen and oxygen and relatively low proportions of carbon and hydrogen. On the other hand, narcotics are rich in hydrogen and carbon and poor in nitrogen and oxygen. These distinct atomic compositions associated with explosives, narcotics and innocuous materials may be utilized as a basis for the non-intrusive screening of a closed container for the presence of contraband.

Furthermore, most explosives have densities in the range 1.2 to 2.0 g cm^{-3} [Ur84, Fa92] which is generally greater than most benign HCNO materials. Figure 1-2 is a plot of the molar density of oxygen versus nitrogen for a number of explosives and other HNCO materials [Gr91]. It can be seen from the figure that all the explosives fall within a single region on the nitrogen versus oxygen density plane that does not contain any of the non-explosives. This feature offers an additional means of identifying the presence of a possible explosive amongst the other substances inside a closed package.

Various ratios [Vo94] of the elements H, C, N and O may also be considered in order to discriminate between contraband and benign everyday materials. Figure 1-3 shows the atomic ratios (a) O:C versus N:C; (b) N:H versus N:C; and (c) O:H versus C:N for the explosives, narcotics and common materials listed in Tables 1-1, 1-2 and 1-3 respectively. Explosives are well characterised by their high O:C and N:H ratios while narcotics have high C:N and C:O ratios. It can be seen that the explosives are well separated from most other materials in figures 1-3(a) and (c), and the narcotics form groups in figures 1-3(b) and (c). A multiple of such elemental ratios may be considered in order to eliminate false positive and false negative readings. For example, orlon (H_3C_3N) has a C:N ratio of 3 which could lead this material to being mistaken for an explosive, which typically have similar C:N ratios. However, the O:N ratio of orlon is 0 which eliminates it from being identified as an explosive. In addition, the H:N ratio of orlon is 3, whereas typical explosives have lower H:N ratios. Melamine ($H_6C_3N_6$), due to its high concentration of nitrogen, could also be confused with an explosive in an analysis based only on a measurement of the nitrogen in the package. The H:N ratio of melamine is unity and its C:N ratio is 0.5 which might lead to it being mistaken as an explosive such as octogen. However, the O:N ratio of melamine is 0 which readily disqualifies it from being identified as an explosive material.

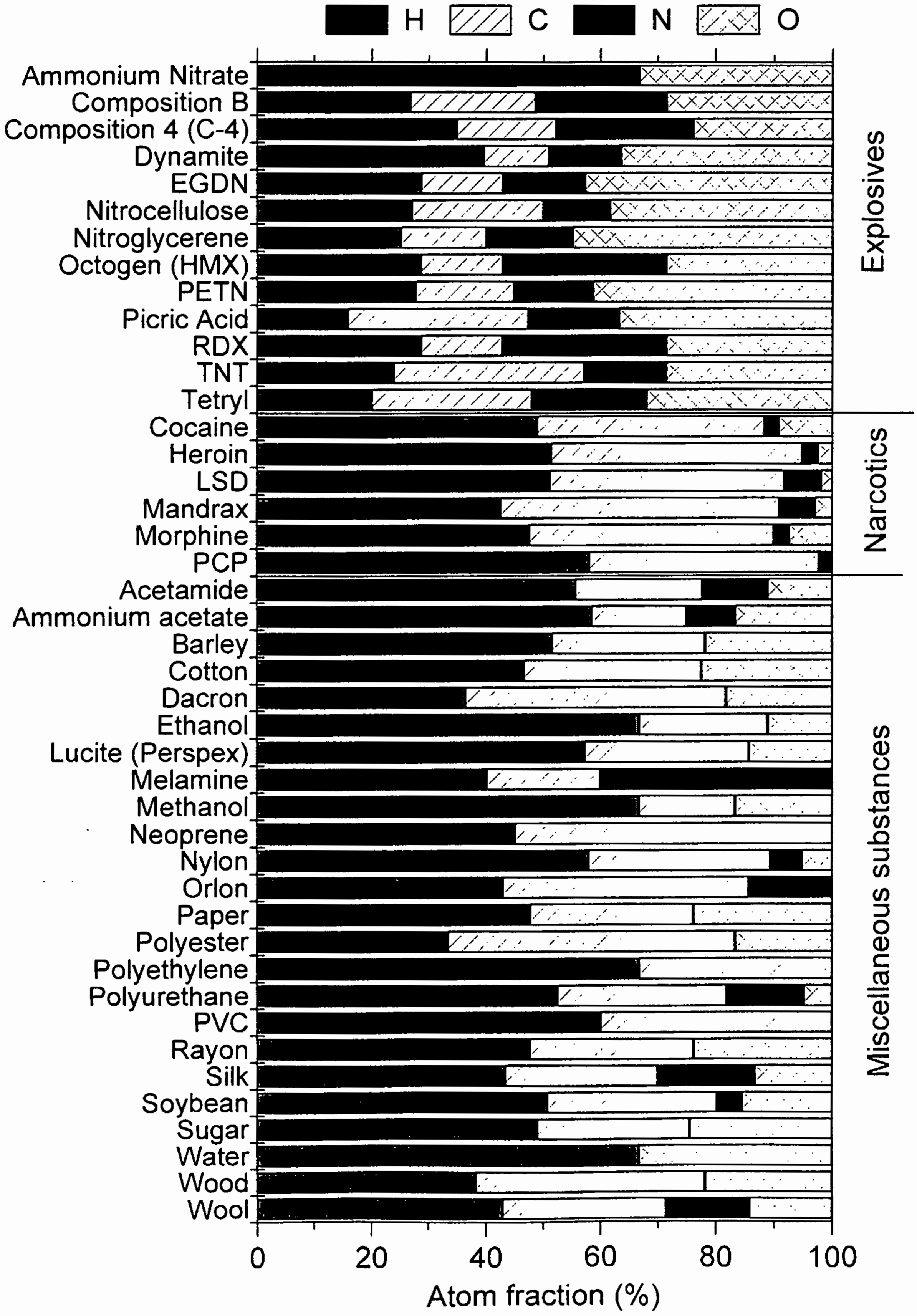

Figure 1-1 Atomic fractions (as a percentage) of the elements H, C, N and O, which constitute the explosives, narcotics and miscellaneous common substances listed in Tables 1-1, 1-2 and 1-3, respectively.

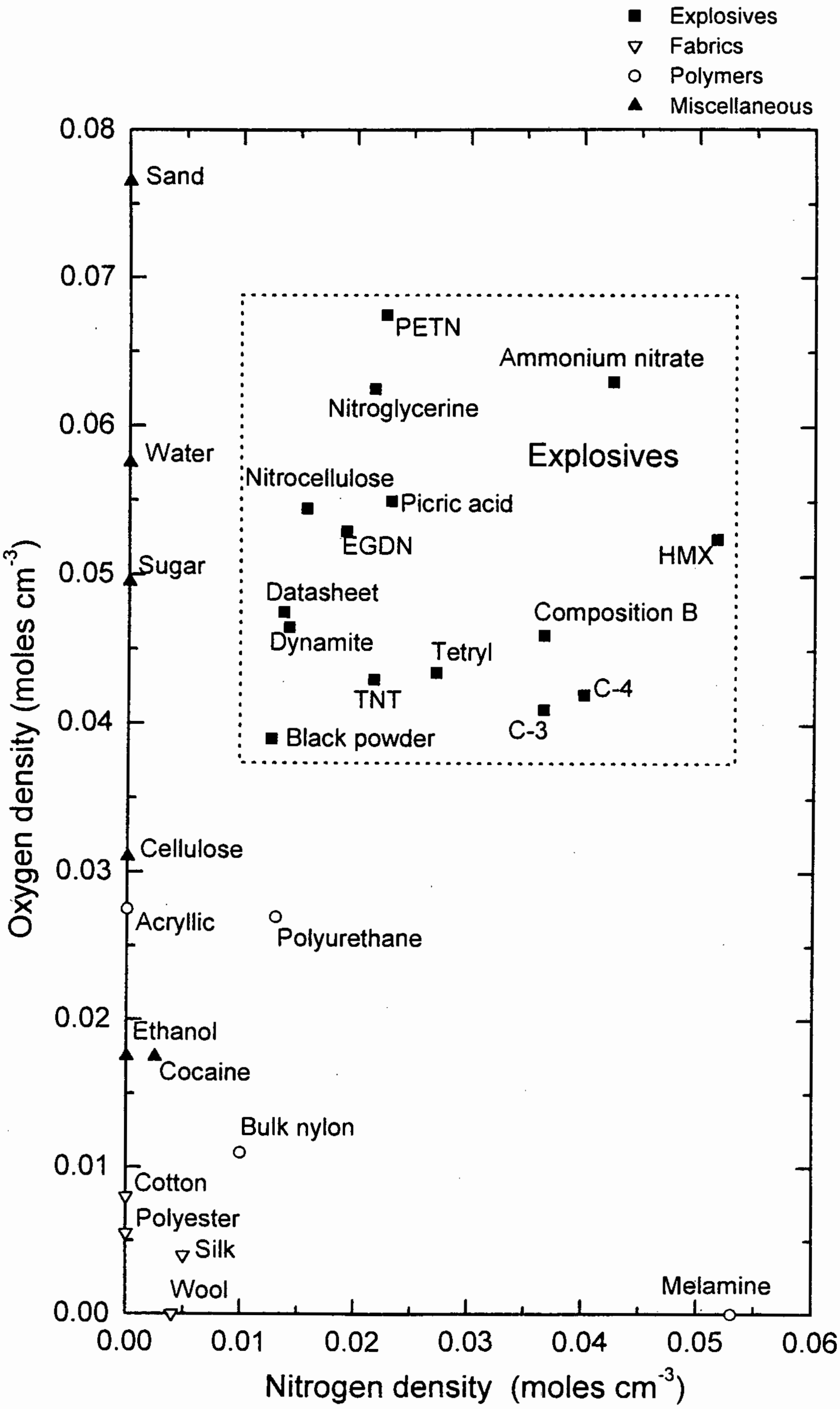

Figure 1-2 Nitrogen density versus oxygen density for a selection of explosives and common substances [Gr91]. All the explosives are grouped within a phase space that contains no non-explosive.

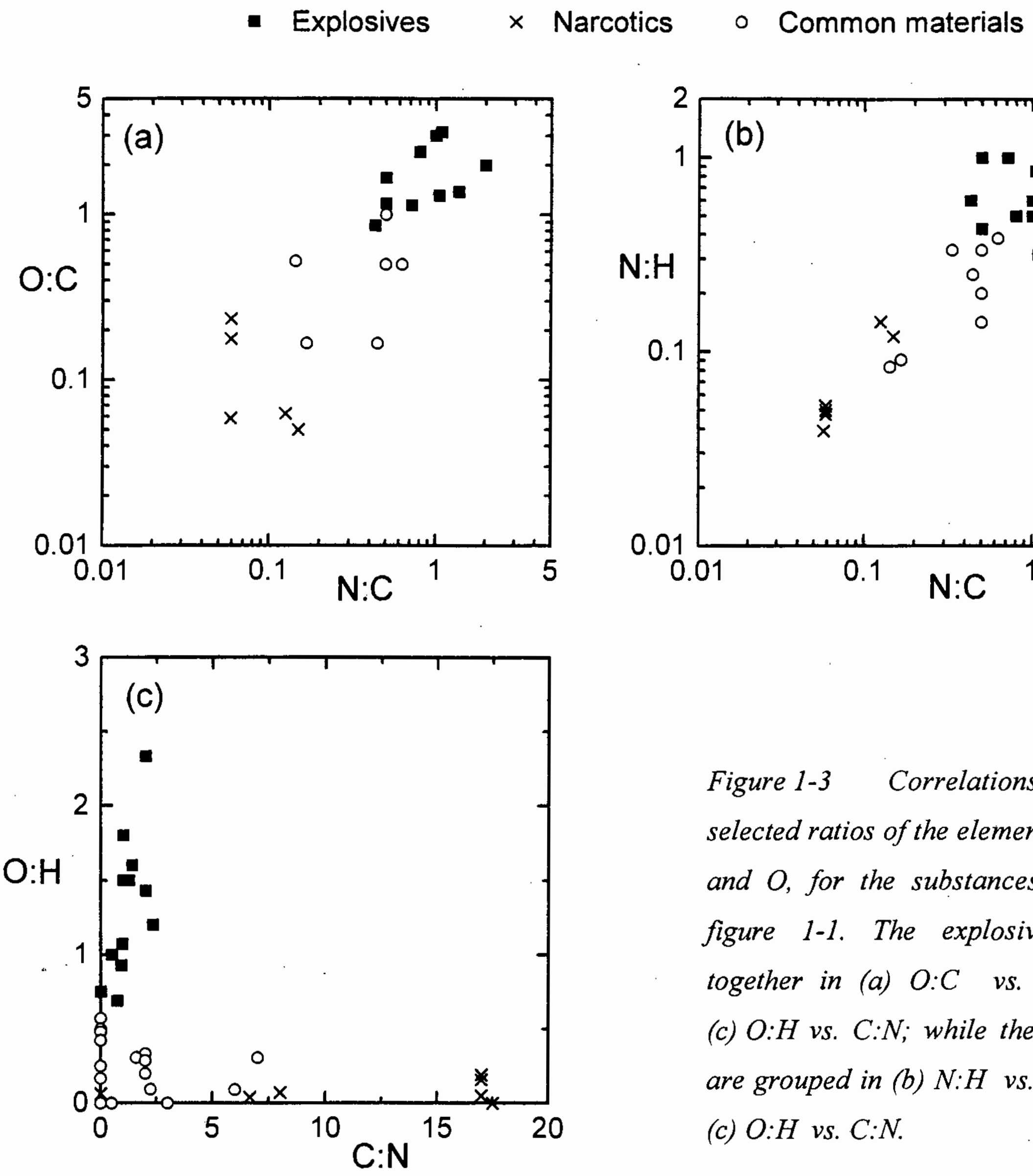

Figure 1-3 Correlations between selected ratios of the elements H, C, N and O, for the substances listed in figure 1-1. The explosives group together in (a) O:C vs. N:C, and (c) O:H vs. C:N; while the narcotics are grouped in (b) N:H vs. N:C and (c) O:H vs. C:N.

Another possible confounder is polyurethane ($H_{10}C_5N_2O$) which has a C:N ratio of 2.5. However, a C:O ratio of 5 and H:O ratio of 2 for polyurethane both serve to separate it from being identified as an explosive. All common goods may be excluded from being misidentified in this way and similar ratios of the elements H, C, N and O may be established for the unambiguous detection of narcotic contraband.

Certain contraband substances contain other elements apart from H, C, N and O which may assist in their detection or identification. For example, narcotics such as cocaine, heroin and morphine are most often found in their more natural derivatives that contain one chlorine atom per molecule [Br94b]. Chemical warfare agents such as sarin, mustard gas and lewisite are frequently found in black powder explosives [Fa92]. Elements such as boron and beryllium are present in nuclear devices; and chlorine, mercury and other heavy elements are often present in drums of containerised waste [Pe94]. Therefore analyses based on the detection of other elements, besides H, C, N and O, could be advantageous in particular situations.

1.2 Non-nuclear inspection techniques

Distinct atomic combinations of the elements H, C, N and O, and others, may be utilized as a basis for the unambiguous identification of explosives and narcotics. However, most of the techniques in use today for the screening of bulk packages for contraband are not able to determine elemental concentrations or ratios, as they depend on either visual imaging or odour sensing. Techniques based on X-rays are widely used for bulk package surveillance [Gr93]. X-rays have many advantages: the production and detection technology is well advanced and relatively inexpensive, the machines are of a reasonable size and their presence is accepted in public places. However, X-rays suffer from the main disadvantage of having a small interaction probability with the low-electron density elements from which explosive and organic materials, including most explosives and narcotics, are composed. Therefore all these substances have undistinguished X-ray absorption or incoherent scattering characteristics. In addition, although X-rays can produce a sharp image as well as a density-dependent shading of the interrogated object [Gr93a], narcotics and explosives can be molded or packed into any form. This makes their detection very difficult through shape recognition, the most commonly used feature in X-ray inspections. For example, X-rays would produce the same image of both a packet of sugar and of cocaine. Therefore, attempts are being made to extend the capabilities of X-ray methods in characterizing organic materials, such as using a multiplicity of energies [Kr91]. Other modern X-ray techniques display features such as refinements in spatial resolution [Gr93], coherent scatter imaging [Ha89, St93], and improvements in computer reconstruction of images including the use of stereoscopic viewing [Sh91].

Another approach to detect contraband relies on chemically detecting the minute amounts of vapours emitted by explosive materials and narcotics. At present, odour-sensing devices are still limited in their use by their low rate of operation as well as insufficient sensitivity to detect explosives having low vapour pressures [Fa92]. The earliest vapour detectors in commercial production were electron-capture devices which exploited the affinity of nitrogen for absorbing electrons and were only sensitive to the high vapour pressure explosives. More recent developments in fast gas chromatography [Je91] and ion mobility of nitrogen for absorbing electrons and were only sensitive to the high vapour pressure explosives. More recent developments in fast gas chromatography [Je91] and ion mobility spectrometry [Ch91] have resulted in improved devices that can also detect some plastic explosives.

A variant of this approach employs trained dogs, the original vapour detectors, to sniff suspicious pieces of luggage or sweep the interior of a building for hidden explosives. However, the high volume of luggage and parcels at venues such as airports makes the use of dogs prohibitively expensive. Moreover, a dog, like a human, has variable moods and behavioural variations and is typically unable to remain focussed for long before needing to rest. Even so, most experts feel [Fa92] that dogs are still more sensitive than the best electromagnetic vapour detectors, and they remain one of the most successful means of finding both hidden explosives and narcotics.

1.3 Neutron-based inspection techniques

The limitations of the inspection techniques described above have stimulated the need to develop alternative methods including *nuclear physics*-based techniques, which may be broadly understood as those approaches making use of incident particle or gamma radiation. In particular, neutrons are effective probes for elemental mapping of bulk samples [Kh94, Go97] since they are not affected by electromagnetic forces and can therefore penetrate deeply into matter, interacting only with nuclei. When a neutron does interact with a nuclide, it is affected in a unique way that depends on the neutron's incident energy and the species of the target nuclide. In particular, the principal elemental constituents of narcotic and explosive substances (H, C, N and O) differ strongly from one-another in their interactions with neutrons and can thus be characterized via these differences. Neutron interrogation techniques generally rely on bombarding the nuclei in the interrogated object with neutrons of particular energy or energies [†] causing them to emit characteristic γ-rays or alter the energy of the interrogating neutrons. The attributes of the probing neutrons and the energy and spatial distributions of the detected radiation (neutrons or de-excitation γ-rays) are used to determine the amounts and positions of the specific interacting nuclides, hence characterizing the interrogated object.

[†] Due to the strong energy dependence of neutron interactions, it has been customary to classify neutrons according to their energy, although no specific boundaries are prescribed between classes. For the present discussions, *fast* neutrons are considered to be those with energies above ~100 keV. Neutrons of energies between ~100 keV and ~0.1 eV are referred to as *epithermal*. At lower energies comparable to the thermal agitation energy at room temperature, neutrons are known as *thermal* or *slow*.

Neutron time-of-flight and γ-ray spectroscopy techniques have been extensively used to measure nuclear levels and neutron cross sections for the various interaction processes possible in the different nuclides. These known cross sections [Mc88, Ro91] and nuclear excitation levels [Le78, Lo81] now provide a foundation for the neutron physics-based techniques for element analysis. In addition, most nuclides exhibit distinctive structure in their scattering cross sections which enhances the probability of certain neutron interactions occurring at specific incident neutron energies and scattering angles. These features can be used to provide information on both the types and amounts of the scattering nuclides.

Some interrogation techniques using neutrons which are already in development are beginning to show the qualities which are essential to an effective detection system [Br94a, Kh94, Vo94, Go97]; these include penetrability (to examine large volumes), sensitivity (to produce a high detection rate with few false alarms), and specificity (to distinguish between materials of interest and background signals). The penetrability of a system is affected by the total and differential neutron cross sections for all the nuclides present in the interrogated sample, the neutron energy loss per elastic or inelastic interaction and the absorption and scattering cross sections for the scattered neutron or emitted photons. The sensitivity of a system is a function of the penetrability, the scattering cross sections and their angular distributions for the *desirable* elemental signatures and the type and size of detectors used to detect the exiting radiation. A system's specificity is affected by the sensitivity, the spatial resolution of the system, the collimation of the incident beam and the energy resolution of the detectors used.

The scanning of the object could be necessary in order to differentiate between the signature of the contraband and the signals from all the other material within the container. In such situations it is often advantageous to pulse the incident neutrons and use the neutron time-of-flight technique to sort the outgoing neutrons or γ-rays. The location of the interacting nuclide is then determined by measuring the flight time of the neutron from its point of creation in the target to the point of interaction with the specific nucleus of interest (if de-excitation γ-rays are detected) or to the point of detection of the scattered or transmitted neutron.

If those techniques that require nuclear reactors or high energy (>50 MeV) electron accelerators are excluded, it is possible to identify ten main nuclear physics-based approaches for elemental characterization of bulk samples. These are summarised in Table 1-4 where the acronyms refer to the operational names of the various techniques, as described in the text below. The approaches that are listed are currently at various levels of development, ranging from very early stages of conceptual or proof-of-principle design, to working prototypes, to fully operational status. Many aspects of these techniques have been patented, particularly in the United States [PAT], although often before displaying practical accomplishment. Some of these techniques inherently provide an elemental image of the object being interrogated, while others are only suitable for smaller parcels. A brief description of the salient features of each of these techniques is presented below.

Table 1-4 Selected features of the main nuclear physics-based techniques for the non-intrusive interrogation of bulk samples.

Technique (see text)	***Probing radiation***	***Radiation source***	***Main reaction type***	***Detected radiation***	***Primary (secondary) signatures***	***Refs.***
TNA	Thermalized neutrons	^{252}Cf ; or d-D or d-T generator source	(n,γ)	Prompt γ-rays produced from neutron capture	N, Cl (H, metals)	[Sh90] [Go91a] [Le94] [Le95]
FNA	Fast neutrons	Radionuclide sources; or generator sources	(n,n'γ)	γ-rays produced from inelastically scattered neutrons	C, N, O (H, Cl)	[So79] [Ca92] [Go94] [Sm95]
PFNA	Fast neutrons	ns pulsed d-D accelerator source	(n,n'γ)	γ-rays produced from inelastically scattered neutrons	C, N, O, Cl (metals, Si, others)	[Sa91] [Sa93] [Br95] [Go95]
PFTNA	Fast neutrons during pulse, and then thermalized neutrons.	μs pulsed d-T generator source	(n,n'γ) & (n,γ)	γ-rays from inelastic scattering, neutron capture and activation analysis	H, C, N, O (metals, others)	[Ba93] [Vo93] [Wo95] [Ba97]
FNTS	White spectrum of fast neutrons	ns pulsed accelerator	all avail-able	Attenuated source neutrons	H, C, N, O	[Ov87] [Ov95] [Ov97]
API	14 MeV neutrons with associated α particles	Associated particle d-T generator	(n,n'γ)	γ in coincidence with α	C, N, O	[Be90] [Go90] [Rh92]
NRA	9.17 MeV monoenergetic γ-rays	Proton accelerator ($E_p < 2$ MeV)	(γ,γ) reso-nance	Attenuated photon beam	N	[Va89] [Va94] [Sr97]
CSI	Monoenergetic γ-rays	γ-ray radionuclide sources	(γ,γ) & (γ,γ')	Attenuated or Compton scattered γ-rays	H, C, N, O (metals, others)	[So79] [Pr93] [Ar95]
PNA	> 13 MeV bremsstrahlung	Electron linear accelerator	(γ,n)	0.511 MeV γ-rays produced from β^+ annihilation	N	[Ha91] [Wh91]
NES	Variable monoenergetic neutrons or white (source) spectrum	Radionuclide sources; or ns pulsed accelerator	(n,n)	Elastically scattered neutrons; usually backscattering	H, C, N, O (others)	[Hu86] [Go91] [Ba94a] [Br94]
FNSA (present work)	Variable monoenergetic fast neutrons	ns pulsed or DC accelerator or generator	(n,n) & (n,n'γ)	Elastically and inelastically scattered neutrons	H, C, N, O, metals, others	[Bu97] [Br98]

1.3.1 Thermal neutron capture

Thermal neutron capture formed the basis of the first neutron-based technique [Sh90], known as Thermal Neutron Analysis (TNA), to be implemented for the detection of hidden explosives at airports. Neutrons produced by a radioactive source or sealed tube neutron generator utilizing the $^{2}H(d,n)^{3}He$ reaction are moderated to low energies (<0.025 eV) and allowed to interact with the bag contents [Le95]. A fraction of these neutrons capture with the nuclides within the bag and the resulting nuclides are typically left in an excited state will decay by emitting characteristic γ-rays [Le78]. The measured γ-ray spectra are related to the number of incident neutrons and the known capture rates [Lo81] for the appropriate nuclides to provide the elemental concentrations in the irradiated sample. The patented TNA technology [Go91a] is principally being developed by Science Applications International Corporation (SAIC) of Santa Clara, USA [SAIC]. TNA explosive detection systems, coupled to high resolution X-ray machines [Le94], have inspected more than two million passenger bags [Go97] at airports in the USA and other countries since 1986, including John F. Kennedy International Airport in New York, and Gatwick International Airport, near London. The application of TNA for the detection of explosives is primarily based on the identification of the nitrogen and hydrogen contained in most explosives [Le95]. The two capture reactions

$$^{14}\text{N} + \text{thermal neutron} \rightarrow {}^{15}\text{N} + \gamma\,(10.83\ \text{MeV})$$
$$^{1}\text{H} + \text{thermal neutron} \rightarrow {}^{2}\text{H} + \gamma\,(2.223\ \text{MeV})$$

produce prompt γ-rays which are detected in an array of detectors and tomographically analyzed to provide the spatial density distribution of nitrogen and hydrogen in the package. Figure 1-4 shows a typical TNA γ-ray energy spectrum measured using a NaI(Tl) detector for a suitcase containing an explosive simulant [Sh90]. The peaks marked in the figure are attributed to some of the elements present in the suitcase and the explosive. Identification of nitrogen in this way is simplified by the fact that the 10.83 MeV γ-ray is the highest energy capture quantum produced from any naturally occurring isotope [Lo81]. However, the other dominant element in explosives, oxygen, has a very small capture cross section [Wa89] for producing gamma emission, and the presence of significant amounts of nitrogen and hydrogen is not a unique identifier of explosives. It is also evident from figure 1-4 that TNA spectra need to be corrected for the substantial background resulting from the capture of thermal neutrons in the system shielding, detectors and other miscellaneous objects.

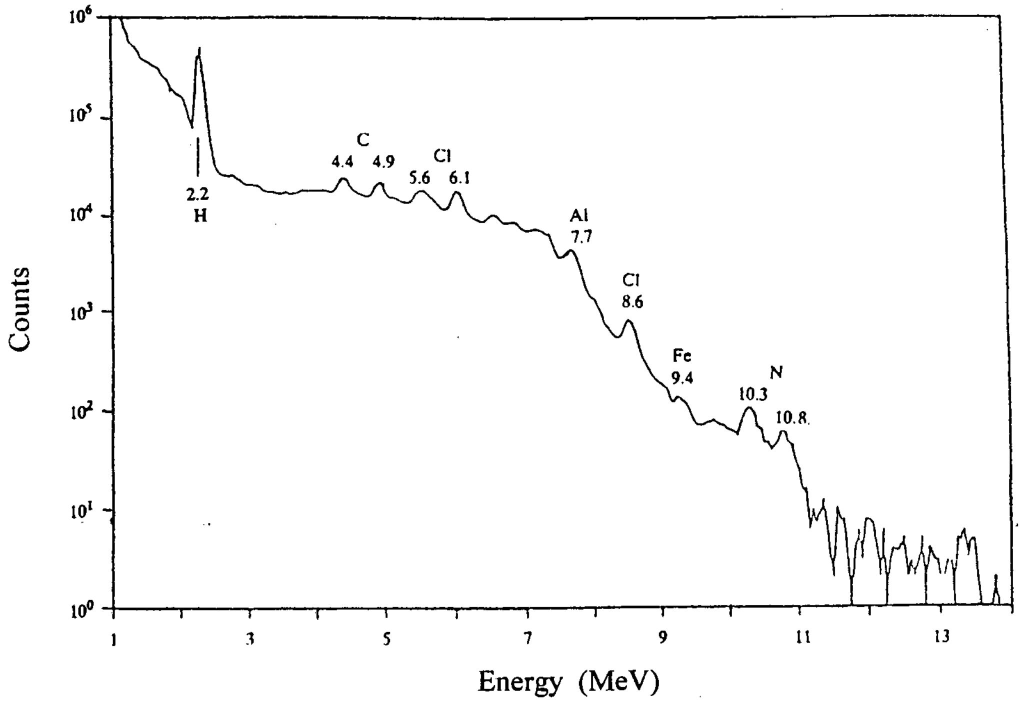

Figure 1-4 Thermal Neutron Analysis (TNA) pulse height spectrum [Sh90] measured by a NaI(Tl) detector for a suitcase containing an explosive simulant. The peaks indicated are associated with some of the elements present in the suitcase and explosive, most notably the 10.8 MeV ^{14}N capture γ-ray peak signaling the presence of the explosive.

1.3.2 Fast neutron inelastic scattering

The basic approach is very similar to TNA but involves bombarding the object under inspection with a collimated beam of continuous fast neutrons typically from a sealed tube neutron generator. The nuclei in the sample are excited through inelastic collisions to specific low-lying nuclear levels that decay by emitting discrete γ-rays [Lo81]. The strong γ-ray transitions which can be induced by fast neutrons ($E_n \leq 8$ MeV) in the nuclides which are important in contraband detection (^{11}B, ^{12}C, ^{14}N and ^{16}O) are shown in figure 1-5. The lack of any low-lying (< 5 MeV) state in ^{16}O is of particular note.

Inelastic neutron scattering forms the basis of a patented technique [Go92] known as Fast Neutron Analysis (FNA) which is illustrated in figure 1-6 [Sm95]. The de-excitation γ-rays released from nuclei activated in fast neutron inelastic scattering events are detected by an array

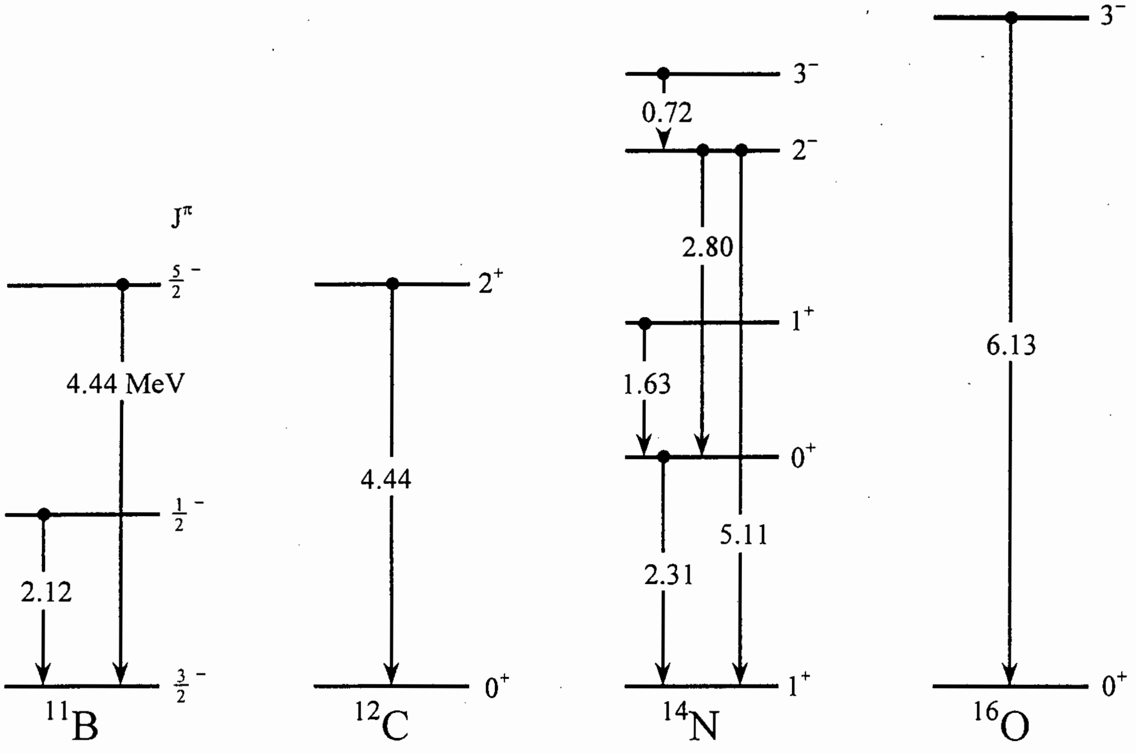

Figure 1-5 *The γ-ray transitions in ^{12}C, ^{14}N and ^{16}O induced by fast neutrons of energy less than 8 MeV. Also shown are the transitions in ^{11}B due to the $^{14}N(n, \alpha\gamma)^{11}B$ reaction.*

of collimated detectors surrounding the object and shielded from the direct exposure to source neutrons. Specific elements present in each voxel are identified through the de-convolution of the γ-ray spectra measured by each detector [Hu93]. The attenuation of fast neutrons within an object is much less than that of thermal neutrons, enabling better image reconstruction than the TNA technique. Figure 1-7 shows FNA spectra [Go94] measured with and without a test suitcase in the beam. The signature of the suitcase is obtained after subtracting the measured background spectrum. FNA imaging is limited to smaller objects due to the lack of geometrical definition when there are large distances between inner voxels and the detectors. Explosive detection systems based on fast neutron scattering are also being developed by SODERN [SODN], France, who are well-known for their range of fully automatic sealed tube neutron generators [Cl91, Ba93, Ba94], applicable to both laboratory and field use.

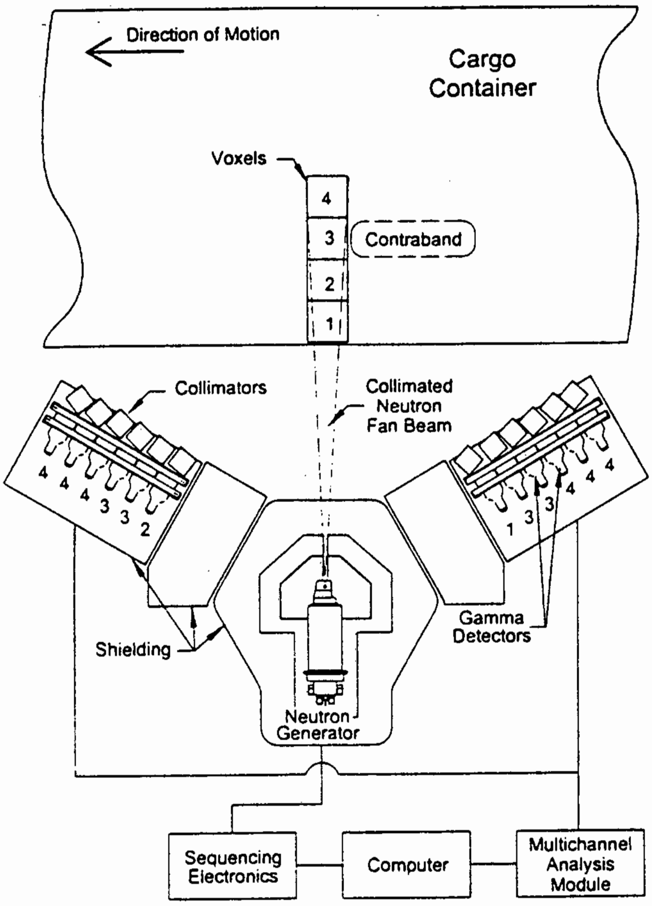

Figure 1-6

Schematic diagram [Sm95] of an inspection system based on Fast Neutron Analysis (FNA). A fan beam of 14 MeV neutrons illuminates voxels in the container at four depths. Collimators direct the gamma-detector fields of view to the voxels indicated by the numeric labels.

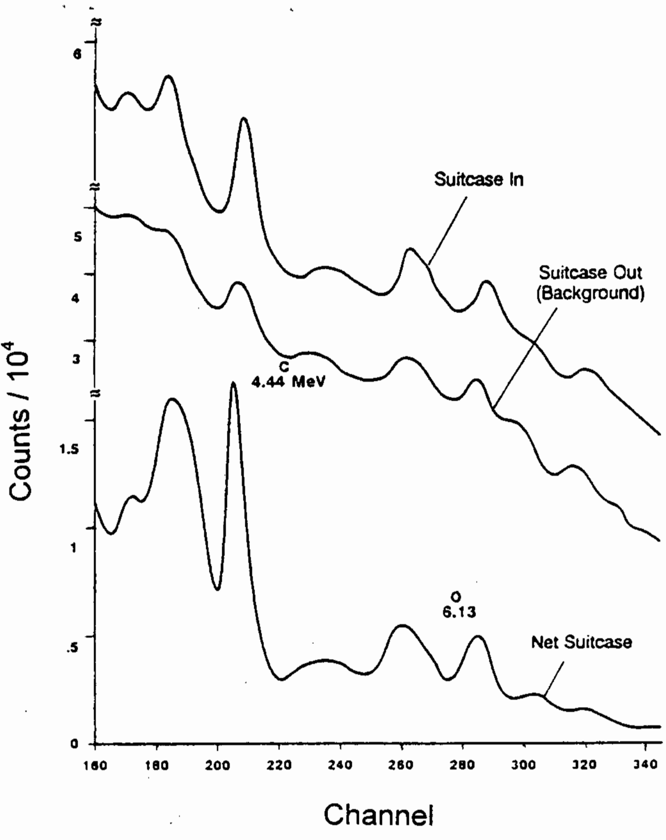

Figure 1-7

FNA γ-ray spectra measured [Go94] with a NaI(Tl) detector for a passenger suitcase. The signal for the net suitcase (lower spectrum) is obtained after subtracting the background. The peaks associated with the de-excitation γ-rays from ^{12}C and ^{16}O are indicated.

Radioactive sources such as ^{252}Cf, ^{241}Am/Be and ^{238}Pu/Be are alternative sources of fast neutrons which are particularly useful in field situations. Applications making use of ^{252}Cf sources are reviewed in [Hu97]. Thermal neutron capture and inelastic scattering have been applied to the identification of chemical warfare agents and high explosive munitons, and to the characterization of unexploded ordnance from firing ranges and former defense sites [Ca92]. The technique generally employs neutrons from a ^{252}Cf source to interrogate the contents of the munition, as illustrated in figure 1-8. The neutron passes through the steel casing of the shell to be captured or inelastically scattered by a nuclide within the munition, releasing one or more characteristic γ-rays [Lo81]. The composition of the munition is deduced from an analysis of the measured spectra of the capture and inelastic γ-rays from elements including As, B, C, Ca, Cl, Fe, H, K, Na, P, S, Ti and Zn [Ca92]. One form of this technology has been developed commercially as PINS (Portable Isotopic Neutron Spectroscopy) Chemical Assay System [PINS] and has been used by the United States army since 1992. Figure 1-9 shows typical PINS spectra measured [Ca92] with a HPGe detector for γ-rays emitted from an one ton container of mustard gas and an 155 mm high explosive artillery shell irradiated with neutrons from a ^{252}Cf source. The measurements feature peaks attributed to the chlorine and sulphur in the mustard gas and the nitrogen in the explosive. Also seen in both spectra are γ-ray peaks associated with neutron capture with the iron nuclides in the mustard gas container and shell casing.

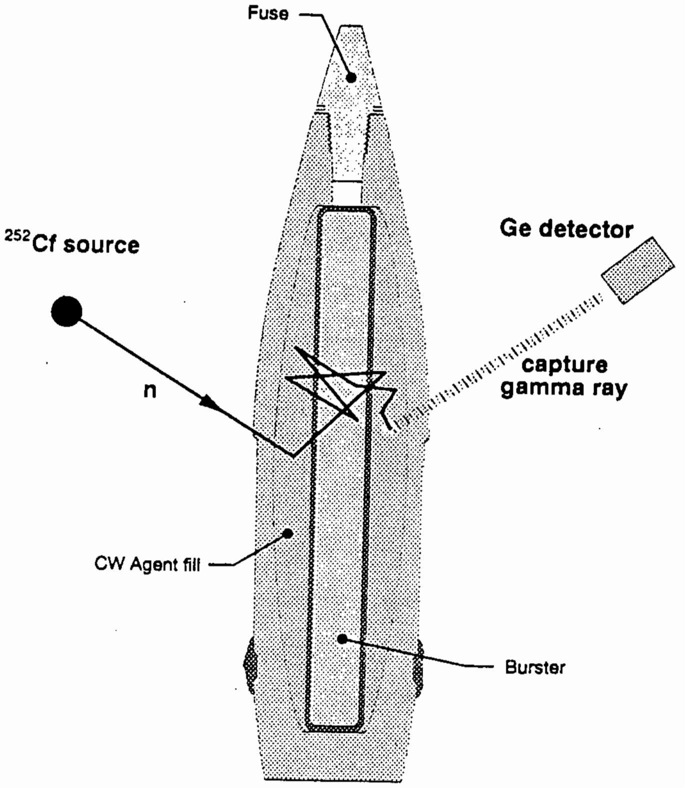

Figure 1-8 A schematic of the Portable Isotopic Neutron Spectroscopy (PINS) chemical assay system [Ca92]. Neutrons from a ^{252}Cf source induce inelastic scattering or capture events with the nuclides within the munition, releasing γ-rays characteristic of these nuclides.

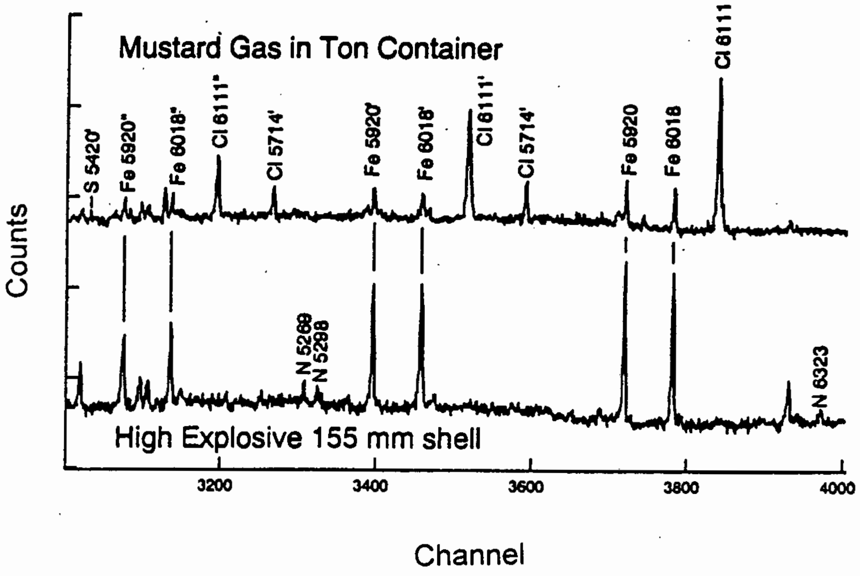

Figure 1-9
PINS γ-ray spectra measured with a HPGe detector for a container of mustard gas (above); and a 155 mm high-explosive shell (below). The characteristic lines are labeled in each spectrum.

Neutron-induced γ-ray techniques using radioactive sources have also been developed for use in the minerals industry, particularly for the on-line analysis of coal [So79, So93]. One such method [So82, So90], shown schematically in figure 1-10, makes use of a ^{238}Pu/Be source providing fast neutrons which interact with the nuclides within the coal hopper. The method for determining the specific energy [So79] of the coal is based on the detection of the 4.43 MeV γ-ray emitted in the inelastic excitation of ^{12}C. Ash and moisture content are determined by simultaneously measuring the 2.22 MeV neutron capture γ-rays from ^{1}H. Similar approaches have been recently developed for the on-line measurement of pre-reduction degree in iron ore [Li94, Li97].

Figure 1-10
Schematic of a system [So79] for the online characterization of bulk coal samples. Measurements are made of the γ-rays produced via inelastic scattering and capture events induced by neutrons from a ^{238}Pu source.

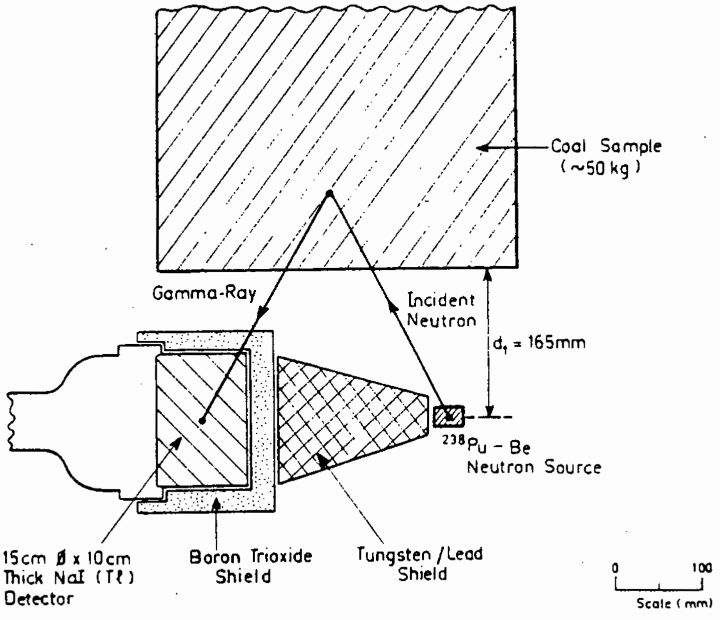

1.3.3 Pulsed fast neutron inelastic scattering

The two limitations affecting fast neutron inelastic scattering techniques, namely the high backgrounds and relatively poor imaging capabilities for large objects, are addressed by nanosecond pulsing the incident neutrons and implementing the method of neutron time-of-flight [Sa91, Go95]. This approach has been extensively developed by SAIC under the name of Pulsed Fast Neutron Analysis (PFNA), particularly for the interrogation of shipping containers. In their system [Br94a, Br95], a 5.5 MeV deuteron accelerator produces nanosecond bunches of approximately 8 MeV neutrons, which are collimated and caused to scan the container under investigation by mechanically rastering the deuteron beam line (see figure 1-11). The γ-rays produced in inelastic scattering events are detected in an array of NaI(Tl) crystals and sorted according to their energy and detection time with respect to the neutron pulse, resulting in a 3-dimensional image of the interrogated object.

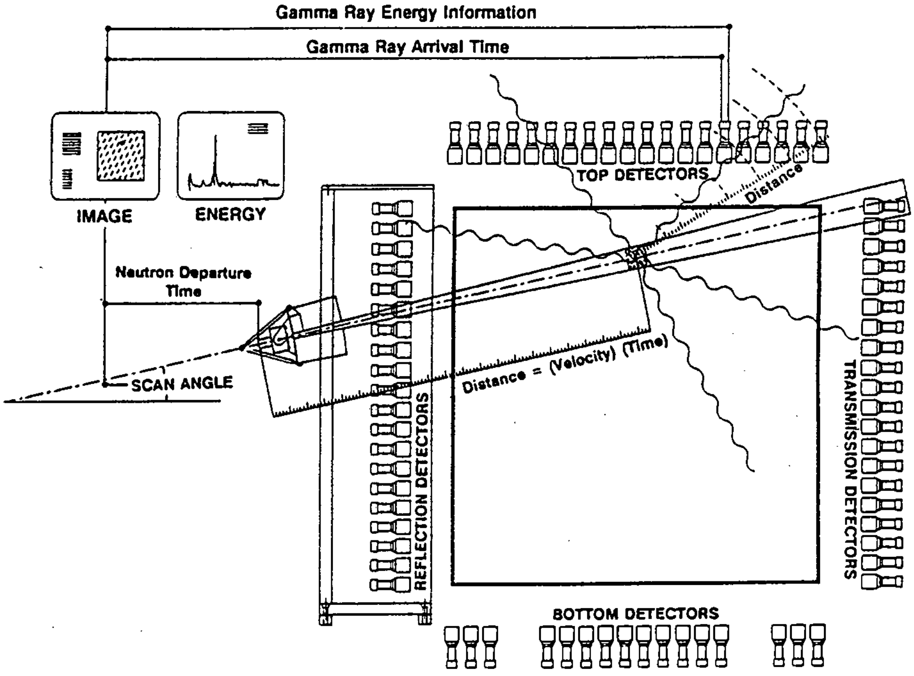

Figure 1-11 Schematic view of a cargo inspection system based on Pulsed Fast Neutron Analysis [Br95]. A beam of ns-pulsed 8 MeV neutrons is raster scanned across the face of the container. Banks of NaI(Tl) detectors measure both the pulse height spectra and arrival time of the de-excitation γ-rays.

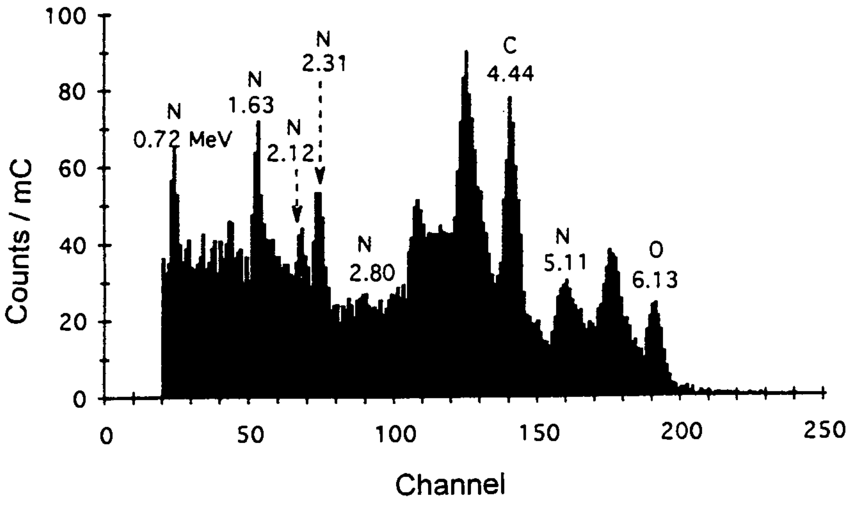

Figure 1-12 A PFNA γ-ray energy spectrum measured with a 7.6 cm ϕ × 7.6 cm NaI(Tl) detector for a small sample of C-4 explosive simulant in a test suitcase. The fingerprint lines of ^{16}*O (6.13 MeV),* ^{12}*C (4.44 MeV), and* ^{14}*N (0.72, 1.63, 212 and 2.31 MeV) are indicated. Also indicated is the weak 2.80 MeV line associated with* ^{14}*N. The 5.11 MeV line of* ^{14}*N coalesces with the second escape peak of the 6.13 MeV* ^{16}*O line.*

The PFNA technique has been applied to the detection of explosives [Sa93] and narcotics [Go94] in passenger luggage and to the characterization of containerized hazardous and nuclear materials [Pe94]. Figure 1-12 shows a PFNA γ-ray spectrum [Sa93], measured with a NaI(Tl) detector, for a small sample of C-4 explosive simulant embedded in clothes inside a test suitcase. The characteristic peaks associated with the inelastic γ-rays from ^{12}C, ^{14}N and ^{16}O are clearly visible. The strong nitrogen and oxygen lines indicate the presence of the explosive. The hydrogen content in the interrogated object is not directly measured by this technique, therefore neutron radiography using transmission measurements of the probing neutron beam has been investigated [Lo95] to be used in conjunction with PFNA systems.

1.3.4 Pulsed fast and thermal neutron analysis

A more complete picture of the elemental content of an object irradiated by neutrons may be obtained from the analysis of the γ-rays produced in both capture and inelastic scattering events. One such approach, Pulsed Fast-Thermal Neutron Analysis (PFTNA), is being developed at Western Kentucky University, USA, and utilizes [Vo93] a μs-pulsed sealed tube neutron generator. A train of 14.1 MeV neutron pulses, a few microseconds wide and produced

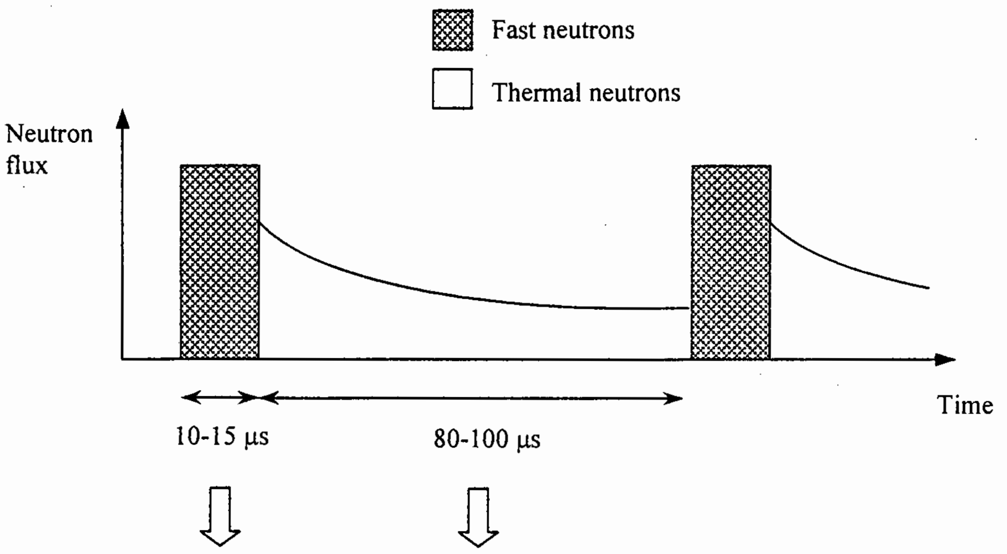

Interaction:	(n, n')	(n, γ)	(n, γ), (n, α), (n, p) ...
Gammas:	Prompt	Prompt	Delayed
Elements:	C, N, O	H, N, S, Cl, Fe	O, Na, Al, Si, P

Figure 1-13 Time sequence of the nuclear reactions taking place in the Pulsed Fast-Thermal Neutron Analysis (PFTNA) technique [Vo93]. A train of 14 MeV neutron pulses, a few μs wide and produced in a sealed tube neutron generator via the $^3H(d,n)^4He$ reaction, is used to irradiate the object under interrogation (see text).

via the ^{3}H(d,n)^{4}He reaction, is used to irradiate the object under interrogation. Figure 1-13 shows the time sequence of the nuclear reactions taking place. Fast neutrons incident upon the object initiate interactions such as (n,n') and (n,p) with elements including C, N and O. The de-excitation γ-rays are detected by high resolution γ-ray detectors such as BGO or HPGe, and the events stored via a gated ADC. The neutron beam is then turned off for about 100 μs during which time some of the fast neutrons remaining within the sample thermalize and are captured by elements such as H, N, Cl and Fe. The prompt capture γ-rays are detected by the same detectors and the events stored separately from the first events. This procedure is repeated with a frequency of approximately 10 kHz. Every few hundred pulses, the neutron beam is turned off for a longer time interval, such as 3 ms, and a different ADC collects the events associated with the delayed emission of γ-rays from the de-activation of elements such as O, Si, F and P. Therefore, by combining fast inelastic neutron scattering, thermal neutron capture and delayed activation analysis, a large number of elements contained in an object can be identified in a

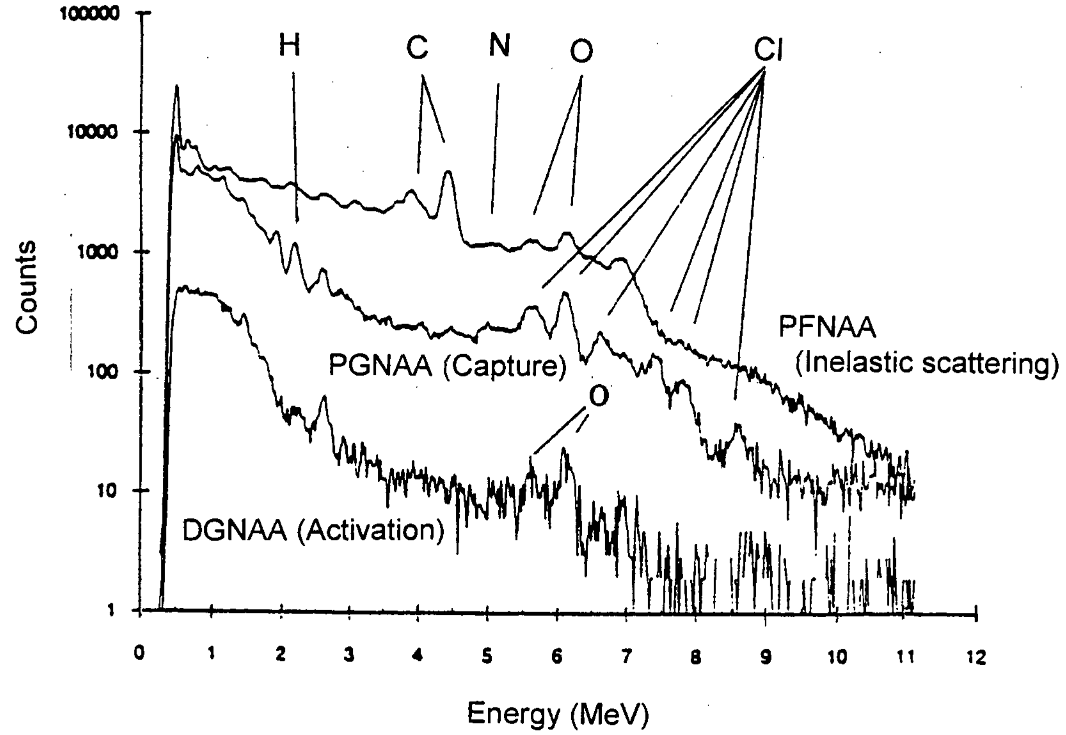

Figure 1-14 Gamma-ray energy spectra measured [Hu93] during the three phases of the PFTNA process for a sample of simulated cocaine hydrochloride. The γ-ray peaks associated with H, C, N, O and Cl are labeled.

continuous mode without sampling. The γ-ray detectors are also collimated and shielded so that the detector field of view and the incident neutron beam define the voxels from which the γ-rays are being received and recorded. The PFTNA signal is thus a composite of three individual γ-ray spectra measured during the three phases of the process. Figure 1-14 shows PFTNA spectra measured [Hu93] for a sample of cocaine hydrochloride showing the peaks associated with the presence of the elements H, C, N, O and Cl in the sample.

The PFTNA method is also being developed to assist with the dismantling of nuclear weapons and for on-line bulk coal analysis [Wo95]. More recently, the technique has been manifested in a reasonably compact probe to be used for the detection of unexploded objects [Vo97a] and has become known as PELAN (Pulsed Elemental Analysis with Neutrons). A group at SODERN [SODN] are developing a similar technique to be used, for example, for the non-destructive verification of sealed munitions [Ba93], the on line analysis of raw minerals [Be94, Ba97], and the detection of buried land mines [Ba97a].

1.3.5 Fast neutron transmission

The total scattering cross sections for fast neutrons are large for most nuclides (see Section 2.2), and also exhibit resonance structure which is unique to the particular nuclide. These features have been used to determine the H, C, N and O areal densities in bulk samples of various organic materials by deconvoluting the measured attenuation of a fast neutron spectrum using standard neutron time-of-flight analyses [Ov83, Ov85]. Figure 1-15 shows two time-of-flight spectra, one measured for neutrons emanating directly from a thick target ^{9}Be(d,n)^{10}B source reaction, and the other for neutrons transmitted by a HCNO sample. The structure in the source spectrum arises from the energy dependence in the neutron production cross sections and from sharp kinematic edges (seen at channels 600, 740 and 900) at the maximum neutron energies for each of the neutron groups produced for a given incident deuteron energy. In the transmitted spectrum, additional variations are observed which correspond to the structure in the

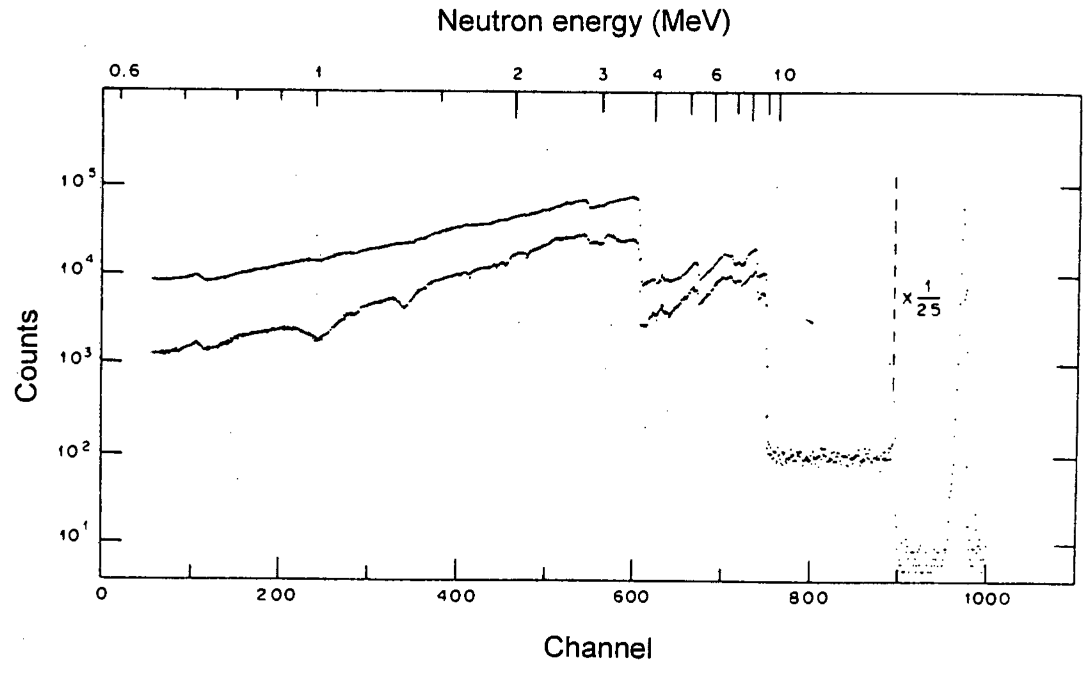

Figure 1-15 Neutron time-of-flight spectra [Ov85] measured for neutrons emanating directly from a thick target ^{9}Be(d,n)^{10}B source reaction (above), and for neutrons transmitted by a HCNO sample (below). Each spectrum was obtained with a 4.5 MeV incident deuteron beam and 1.2 mC of integrated beam current. Time-of-flight increases to the left at 0.954 ns/channel and neutron energy is shown by the upper scale. The additional structure in the transmitted spectrum corresponds to resonances in the total cross sections for the nuclides in the sample.

total cross sections for the elements in the sample. It has been demonstrated [Ov87] that many projections of the transmission spectra can be combined via computer tomography to produce spatial distributions of individual elements in an object. This technique, known as Fast Neutron Transmission Spectroscopy (FNTS), is being developed at the University of Oregon for the detection of explosives hidden in airline luggage [Ov95, Le97]. A continuous neutron spectrum with energies up to 8.2 MeV is produced by a nanosecond bunched 4.2 MeV deuteron beam slowing down in a thick beryllium target. With reference to figure 1-16, a fan beam of neutrons is directed through the suitcase under interrogation and the transmitted neutrons are detected in an array of plastic scintillators. A hydraulic lift transports the suitcase through the beam while individual neutron detectors record the neutrons transmitted through each pixel. The transmitted spectra are then deconvoluted to provide an elemental map of the suitcase [Ov97]. The development of an effective screening algorithm for the FNTS system is an ongoing project and has involved extensive Monte Carlo investigations. Monte Carlo simulations of FNTS experiments have also been completed at the Argonne National Laboratory [Mi94, Yu94]. These results also suggest that FNTS is promising for practical explosive detection [Fi95] as do calculations based on tomographic reconstruction algorithms using FNTS data from the Oregon group [Yu97].

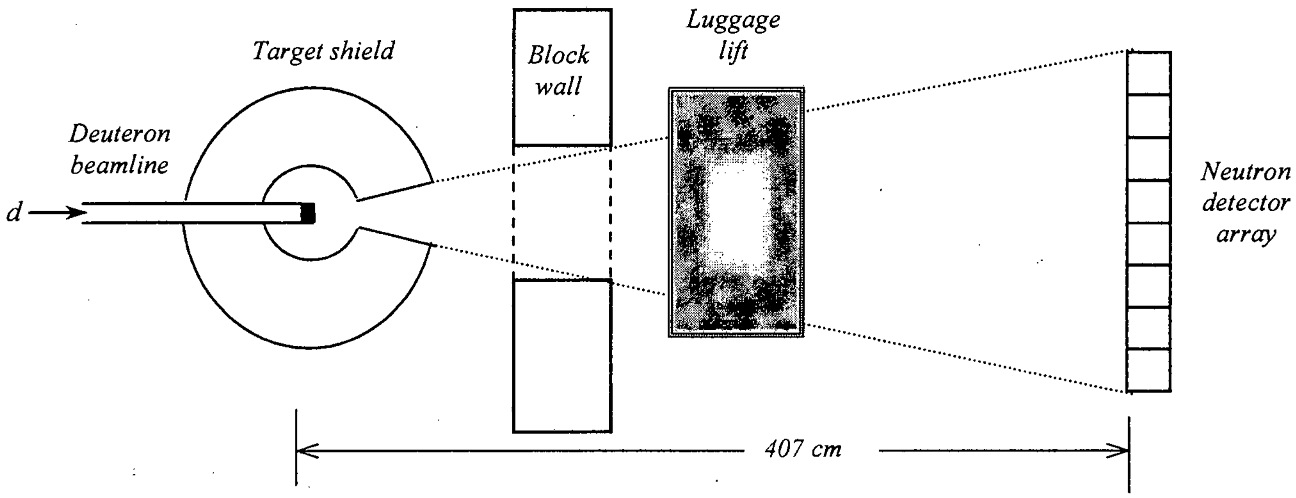

Figure 1-16 Schematic of a luggage screening system based on the Fast Neutron Transmission Spectroscopy (FNTS) technique. A ^{9}Be target is centred in the target shield comprised of water and lithium carbonate. A fan beam is formed by a high-density polyethylene collimator in the target shield and directed through a concrete block wall. A hydraulic lift transports the test suitcase through the beam and a 16-detector array records the neutrons transmitted through each pixel. Adapted from [Le97].

Transmission techniques involving radioactive sources have also been developed. A method for the detection of bulk explosives based on the transmission of fast neutrons from a ^{252}Cf source has been investigated [Hu90, Go97a]. The fission spectrum of ^{252}Cf is well characterized [Ro91] and is smoothly varying, therefore mapping of transmission and scattering measurements allows the bulk identification of materials. A fast neutron and γ-ray transmission (FNGT) technique has been used for the on-line determination of coke moisture at blast furnaces [So90]. A gauge has been developed consisting of a ^{252}Cf source and a Li-glass detector placed within a polyethylene moderator, mounted on either side of the conveyer belt. Since the transmission of fast neutrons depends predominantly on hydrogen concentration and mass per unit area, while γ-ray transmission depends only on mass per unit area, measuring both transmissions simultaneously allows the hydrogen content in the coke to be determined.

1.3.6 Associated particle imaging

The well-established associated particle technique [Ba52, Ba68, Sc69] is distinguished by the source neutrons being tagged in time and direction by the particles which are simultaneously emitted in the nuclear reaction generating the neutrons. Associated Particle Imaging (API) has been applied to bulk sample analysis [Rh92] due to the recent emergence of the associated particle sealed tube neutron generator (APSTNG) [Be90, Go90] making use of the ^{3}H(d,n)^{4}He reaction. In the APSTNG deuterons are accelerated to 100 keV, producing 14.1 MeV neutrons and 3.5 MeV alpha particles which are emitted in opposite directions, as illustrated in figure 1-17. Each alpha particle which is detected in the position sensitive detector tags the direction of the associated neutron. These neutrons then scatter inelastically off nuclei

Figure 1-17
The Associated Particle Imaging (API) technique. The direction of the incident neutron is determined by detecting the associated α-particle in a position-sensitive detector. The flight-time of the neutron determines the voxel within the object from which the γ-rays are emitted (also see figure 7-2).

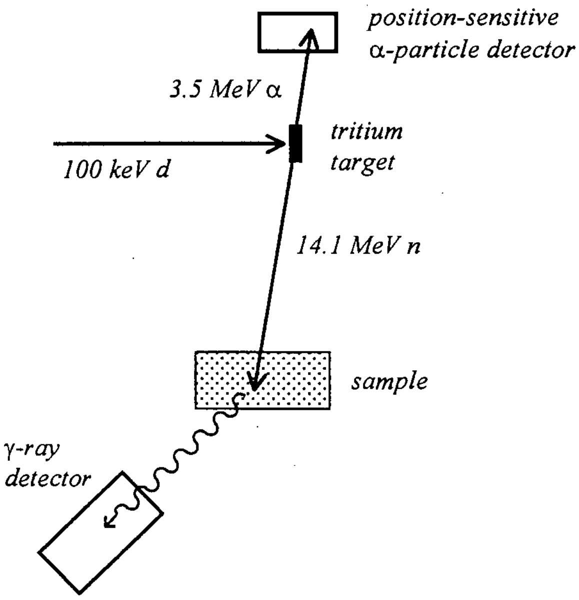

in the interrogated material producing characteristic γ-rays in a similar fashion to the FNA, PFNA and PFTNA techniques. Knowledge of the direction and speed (5 cm ns^{-1}) of the neutron and the speed of the γ-rays (30 cm ns^{-1}) allows the position of the scattering nuclide to be located in space. The main advantage of this approach is that the interrogating neutron beam does not need to be pulsed allowing the use of cheaper sealed tube neutron generators. However, these generators do have a finite lifetime and typically need to be replaced after 200 hours if operated to produce 10^7 neutrons per second [Rh92].

1.3.7 Non-neutron nuclear techniques

A number of nuclear approaches are being developed which are not based on the use of neutrons which is viewed as an advantage in certain circumstances. For example, Nuclear Resonance Absorption (NRA) uses the ability of certain isotopes to selectively absorb γ-rays of a specific, precisely defined energy. The technique has been pioneered at the Soreq Nuclear Centre, Israel [Va89, Va90, Va93] and makes use the well-studied 9.172 MeV level in ^{14}N which may be excited by the direct, resonant capture of 1.748 MeV protons. The $^{14}N^*$ nucleus is created with a kinetic energy of 125 keV and γ-rays which are emitted from the recoiling nucleus are Doppler shifted with an energy uniquely correlated with the angle between the emitted photon and the incident proton beam. With reference to figure 1-18, γ-rays of energy 9.172 MeV which are emitted in a 0.5° wide cone centred about 80.7° are then "in resonance" and will excite the nitrogen nuclei in the interrogated sample with a cross section of about one barn. The transmitted γ-rays are detected and related to the nitrogen concentration in each pixel of sample [Va94, Sr97].

Figure 1-18 Schematic diagram of a method to detect explosives based on the nuclear resonance absorption of γ-rays in ^{14}N [Va94]. Gamma radiation of energy 9.17 MeV is produced by the resonant capture of 1.75 MeV protons in a ^{13}C target. The recoiling $^{14}N^*$ nuclei decay in flight and a flux of 9.17 MeV γ-rays is obtained on the periphery of a cone with polar angle 80.7° to the beam. These 9.17 MeV γ-rays are in turn resonantly absorbed by the ^{14}N nuclei within the interrogated object.

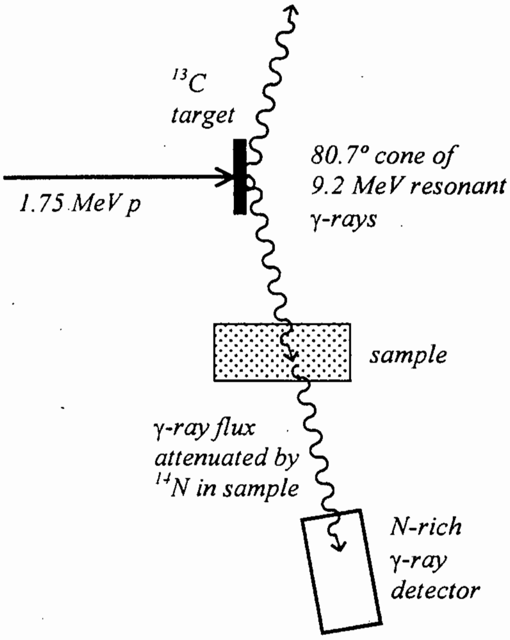

Another technique, Photo-nuclear Activation (PNA) makes use of a radio-frequency linear accelerator [Wh91] to produce an electron beam with an energy of at least 13.5 MeV [Ha91]. The electrons strike a tantalum target producing bremsstrahlung radiation with an endpoint energy equal to the electron beam energy. These X-rays interact with the nitrogen in the explosive via the photo-nuclear reaction $^{14}N(\gamma,n)^{13}N$ which is followed by the decay of ^{13}N via positron emission. The positron immediately annihilates producing two 511 keV photons that are detected in coincidence and related to the amount and position of the nitrogen in the sample under interrogation. This type of imaging, called positron emission tomography (PET), is similar to that used in modern medical diagnostics. The need for a high dose rates due to the low $^{14}N(\gamma,n)^{13}N$ cross section and the self absorption of the signal (0.511 MeV) γ-rays lead to long measurement times which presently limit the possibilities of implementing a PNA system in a situation such as an airport.

Techniques for non-destructive testing and imaging have also been developed using gamma radiation from radioactive sources such as ^{60}Co or $^{241}Am/Be$ [Hu86a, Ar95]. Tomographic Compton Scatter Imaging (CSI) of the electron density of a sample is possible through the analysis of the spectrum of which have been scattered from the sample [Ba81, To81, Pr93]. Gamma ray transmission techniques using radionuclide sources have also been developed for applications such as online analysis in the coal, oil and mineral industries [So79, Cu90, So93].

1.4 Neutron scattering for element analysis

The neutron-based techniques described above either involve the detection of the gamma radiation induced via inelastic scattering (FNA, PFNA, PFTNA and API) or the capture of thermalized neutrons (TNA and PFTNA), or the detection of neutrons (FNTS) which are transmitted through the sample. An alternative approach which has received comparatively less attention to date is to use an incident neutron beam and to detect, directly, *the neutrons scattered out of the beam.* When monoenergetic neutrons are scattered from the nuclides in a sample, the energy spectrum of the neutrons scattered at a given angle contains information which can, in principle, be used to determine the position and type of the scattering nuclides. The scattered neutrons undergo a change in energy which is dependent upon the energy of the incident neutrons, the angle of scatter, as well as the mass of the target nuclide through the kinematics of neutron scattering. The intensity distribution of the neutrons scattered from a specific nuclide is also a function of the incident neutron energy and scattering angle, and is governed by the total and differential cross sections for neutron scattering.

Certain features of neutron scattering applicable to element analysis have already been demonstrated in the laboratory, in particular with respect to the energy changes of elastically scattered neutrons ('NES' in Table 1-4). For example, measurements have been made [Br94] of the neutrons scattered at 150° from small samples containing the elements C, N and O. The scattered neutrons were detected by a deuterated anthracene crystal (10 mm $\phi \times 21$ mm) [Br88] which detects neutrons by n-d elastic scattering. The spectrometer utilizes the anisotropy of the scintillation characteristics [Br74] of anthracene crystal scintillators to select the forward peak in the angular distribution of recoil deuterons associated with n-d elastic scattering. Figure 1-19 shows pulse height (L) spectra measured with the deuterated anthracene crystal for 14 MeV neutrons scattered at 150° from samples of graphite, liquid nitrogen, water and alcohol, ranging in mass between 0.3 and 0.9 kg. Also shown in figure 1-19 is a background spectrum measured without a sample and an open beam calibration spectrum measured at 14 MeV. The spectra obtained with the scatterers show the expected increase in the upper limit of L as the scattering element is changed from C to N to O, due to the increase in backscattered neutron energy with increasing target nuclide mass. The strong peak at pulse height $L = 320$ in the spectra obtained for samples which contain carbon arises from inelastic scattering to the 4.43 MeV excited state in ^{12}C. The weaker peak observed at $L = 380$ for nitrogen is similarly attributed to inelastic scattering to the low levels of ^{14}N (see figure 1-5). The relative intensities of the elastic and inelastic peaks for carbon and nitrogen agree with estimates based on scattering cross-section data (see Section 2.2) and the calculated variation of detection efficiency with neutron energy for the crystal. The curves in figure 1-19 are the result of least squares fits [Br94] to the data using calculated components based on the lineshapes measured for monoenergetic neutrons.

A method of elemental analysis has been reported [Go91] based on the kinematics of neutron elastic backscattering and making use of the resonances in the neutron scattering cross sections for different nuclides. Scattering samples containing the elements C, N, O and Si were irradiated with monoenergetic neutron beams of different energies. Backscattered neutrons were detected and sorted according to their flight times between the source and the detector. Figure 1-20 shows neutron time-of-flight spectra [Go91] measured for neutrons backscattered from a sample of melamine ($H_6C_3N_6$) reinforced with fibreglass (comprising of oxygen and silicon). Data were collected at three incident neutron energies: 1.78 MeV (figure 1-20(a)), 1.93 MeV (figure 1-20(b)) and 2.08 MeV (figure 1-20(c)). The peaks associated with the detection of neutrons that were elastically scattered from carbon, nitrogen, oxygen and silicon nuclei are visible at all three energies and are labeled in the figure. The broad peak at low energy may be associated with a background component. It can be seen that an enhanced yield is measured for

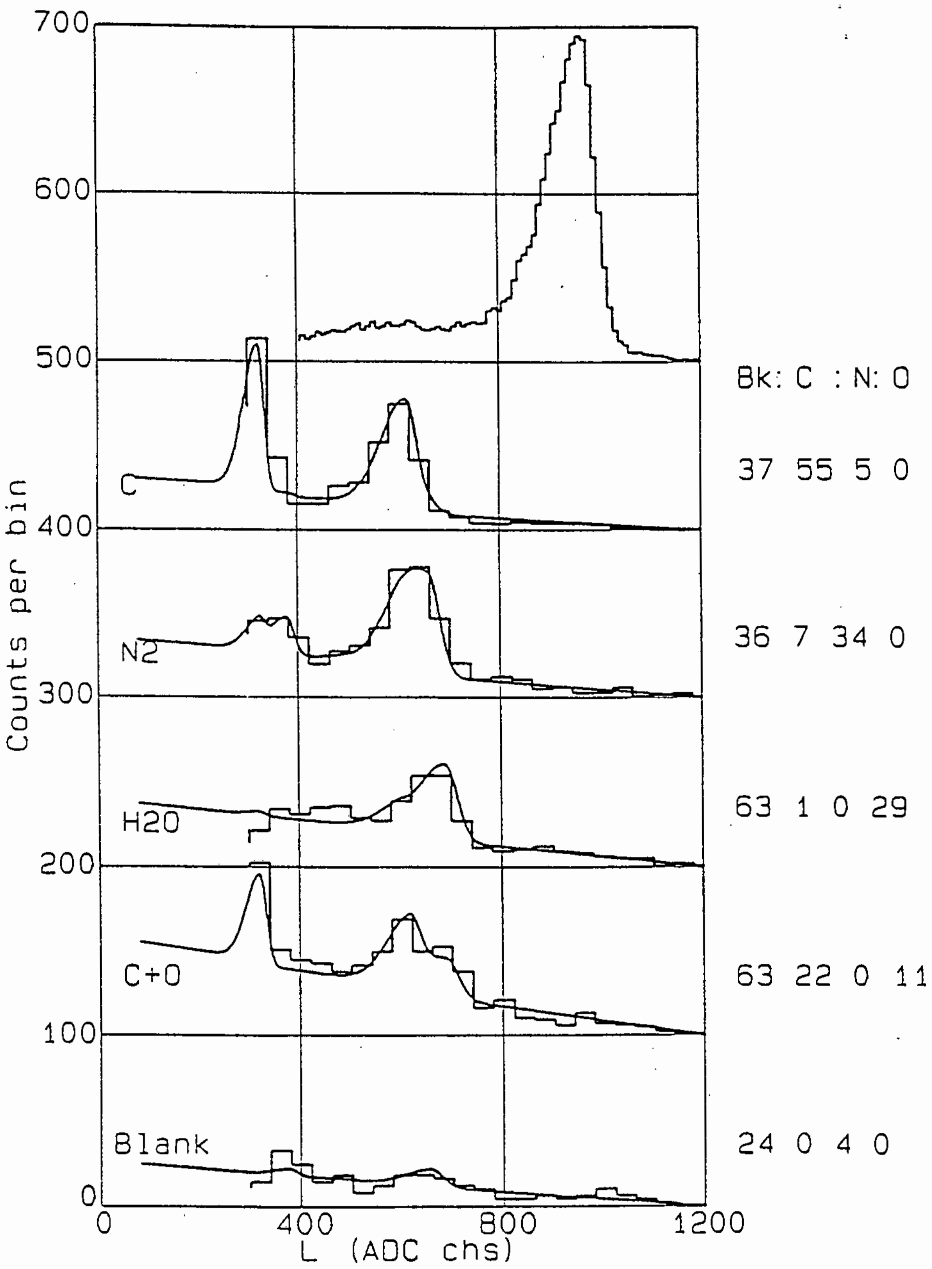

Figure 1-19 Measured forward recoil spectra (histograms) showing a calibration peak for 14.1 MeV neutrons (top) and scattering spectra for no sample (blank) and for four scatterers: graphite; liquid nitrogen; water and methanol. Successive spectra are offset in multiples of 100 on the ordinate scale. The curves show least squares fits to the data. The numbers on the right indicate the relative proportions of the background and of the elements C, N and O respectively, determined from the fitting [Br94].

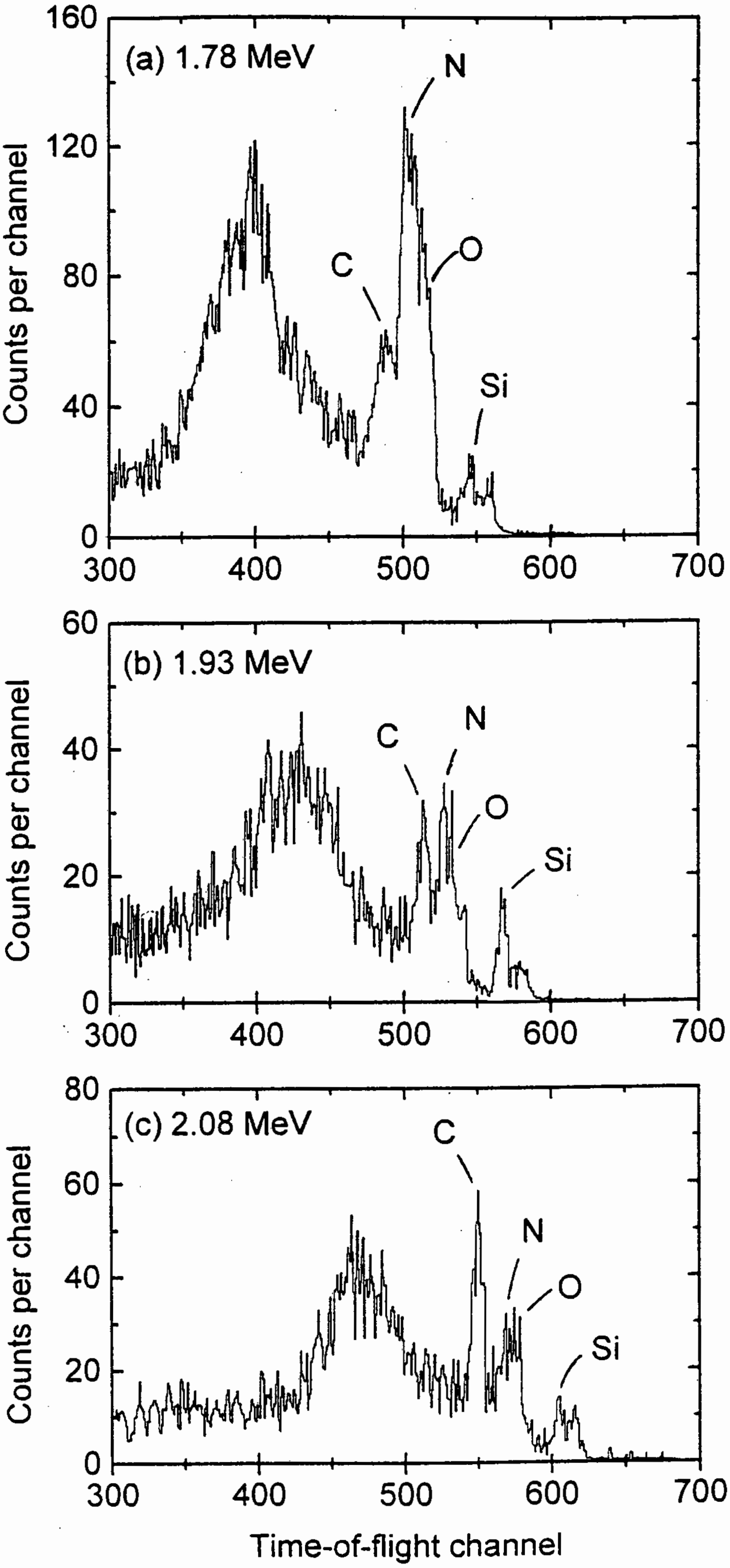

Figure 1-20 Neutron time-of-flight spectra measured [Go90a] for neutrons backscattered from a sample of melamine reinforced with fibreglass at the incident neutron energies: (a) 1.78 MeV, (b) 1.93 MeV, and (c) 2.08 MeV. Peaks associated with the detection of neutrons elastically scattered from carbon, nitrogen, oxygen and silicon are indicated. The broad distribution at low energy is associated with a background component.

nitrogen at 1.78 MeV, silicon at 1.93 MeV and carbon at 2.08 MeV, in accordance with resonance peaks in the neutron scattering cross section curves for the three elements, respectively, at these energies (see Section 2.2). It has been suggested [Go91] that by comparing spectra measured at two energies, off and on a resonance in the cross section for a particular nuclide, a quantitative measure of the scattering nuclide may be determined. A technique for the detection of explosives based on the kinematics of neutron elastic backscattering has been patented [Go89, Go90a] although no practical system has been developed.

A beam of 14 MeV neutrons has been used in a single-exposure neutron tomography (SENT) technique [Hu86, Hu86a] which was developed for measuring the density distribution of a gas-liquid (two phase) flow system in a pipe. The technique employs a well-collimated neutron source with an array of liquid scintillators to detect the neutrons elastically scattered mainly from the hydrogen in the test section of the pipe. Radioactive sources, most notably ^{252}Cf, have been used to measure the hydrogen content in materials by detecting the thermalized neutrons scattered from the sample. Noteworthy applications of this approach include the measurement of moisture in soil [Gr81], and the fat content in meat [Ba94a]. A portable device using a ^{252}Cf source and Li-glass detector in backscattering geometry has been developed for the detection of hydrogen-rich narcotics [Tu94]. The void fraction of boiling water flow in a metallic pipe has also been measured in a similar way [Hu88] as has the volume fractions in a three-phase flow of oil, water and gas [Hu95].

1.5 The present work

The present laboratory studies explore ways in which the elemental content of a small object such as a suitcase (< 0.5 m^3) may be determined by analyzing measurements of the neutrons scattered from the object when it is irradiated by a beam of fast monoenergetic neutrons. The characteristics which can be used to identify the nuclides responsible for the neutron scattering, and hence the elements comprising the object, are governed by the differential neutron scattering cross sections (elastic and inelastic) of the different nuclides, and the kinematic dependence of the neutron energy loss on scattering from a target nuclide. The various possibilities of element identification by the detection of scattered fast neutrons were systematically explored using liquid scintillators, incorporating some features which have already shown promise in other approaches for package screening, such as time-of-flight analyses used in PFNA. Pulse height and time-of-flight data were measured at discrete scattering angles using monoenergetic neutron beams incident on various samples. Nuclide-specific scattering information was incorporated into a distinctive 'scattering signature' for each nuclide studied which were used to analyze scattering measurements made using scatterers of unknown composition. Studies were also completed to examine the effects of neutron interactions in any other material close to the sample, especially material in the incident neutron beam, or between the sample and the detectors. Methods of locating contraband hidden within a larger volume were also investigated in order to assess the possibilities of implementing an FNSA system in practical situation such as an airport.

Chapter 2

Nuclide identification from neutron scattering

The neutrons scattered from a sample carry information which can be used to identify the positions and concentrations of the nuclides in the sample which are responsible for the scattering. A number of approaches are possible for identifying and measuring nuclides in this way which are based on observations of the *energy* and *intensity* distributions of both the elastically and inelastically scattered neutrons. The energy spectrum of the neutrons scattered from a specific nuclide is a function of the incident neutron energy and the scattering angle. The *energy* of the scattered neutrons depends on the mass of the target nucleus through the *kinematics* of neutron scattering, while the *intensity* of scattered neutrons is governed by the *differential cross sections* for neutron scattering from the particular nuclide.

2.1 Energy changes in neutron scattering

2.1.1 Kinematics of elastic scattering

For a beam of neutrons impinging on a target nuclide, the neutrons elastically scattered in a particular direction have a unique reduced energy determined by the mass of the nuclide. The kinematics of elastic scattering in the non-relativistic limit [Ba61, Mi67, Me67] leads to the expressions

$$E_n = \frac{1}{2}E_o\{(1+\xi) + (1-\xi)\cos\Theta\} \qquad (2.1)$$

and

$$\cos\theta = \frac{A\cos\Theta + 1}{\sqrt{A^2 + 1 + 2A\cos\Theta}} \qquad (2.2)$$

where

$$\xi = \left(\frac{A-1}{A+1}\right)^2$$

and A is the mass number of the scattering nuclide, E_o and E_n are the energies of the incident and scattering neutrons, respectively, after neutron scattering at an angle θ in the laboratory system, and Θ is the corresponding angle in the centre-of-mass system. It can be seen from equations 2.1 and 2.2 that there is a direct relationship between the scattered neutron energy and angle of scattering for a particular nuclide. Figure 2-1 shows (a) the ratio E_n / E_o versus A for various values of θ ; and (b) E_n / E_o versus θ for various scattering nuclides. Table 2-1 lists the ratios E_n / E_o , calculated (equations 2.1 and 2.2) for a number of scattering nuclides at $\theta = 45°$, 90° and 150°. Two important features of elastic scattering are evident from figure 2-1 and Table 2-1. Firstly, from figure 2-1(a) it can be seen that for a given laboratory angle, the scattered neutron energy is greater for the heavy nuclides than for the light nuclides; and secondly, from figure 2-2(b) it can be seen that the energy difference for elastically scattered neutrons increases between the nuclides as the laboratory angle increases towards the backward direction.

From equations 2.1 and 2.2 it follows that the energy E_n of the scattered neutron is bounded in range between

$$\xi E_o < E_n < E_o \qquad (2.3)$$

where the limits correspond to scattering at $\cos\Theta = +1$ and -1, or $\theta = 0°$ and 180°, respectively. For $A > 1$, the energy E_n of elastically backscattered neutrons ($\theta = 180°$), is given by the formula

$$E_n = E_o\,\xi . \qquad (2.4)$$

Therefore, if E_n can be measured sufficiently accurately then the kinematics of this process provides a basis for determining the mass of the scattering nuclide. For $\theta \to 180°$ the situation is analogous to the well-known technique of Rutherford backscattering (RBS) in which energetic charged particles are used to analyze the elemental composition of thin films or surfaces. The neutrality of the neutron gives neutron scattering the capacity for analyzing an extended sample

$$E_n = \frac{1}{2} E_o \{(1+\xi) + (1-\xi)\cos\Theta\} \tag{2.1}$$

and

$$\cos\theta = \frac{A\cos\Theta + 1}{\sqrt{A^2 + 1 + 2A\cos\Theta}} \tag{2.2}$$

where

$$\xi = \left(\frac{A-1}{A+1}\right)^2$$

and A is the mass number of the scattering nuclide, E_o and E_n are the energies of the incident and scattering neutrons, respectively, after neutron scattering at an angle θ in the laboratory system, and Θ is the corresponding angle in the centre-of-mass system. It can be seen from equations 2.1 and 2.2 that there is a direct relationship between the scattered neutron energy and angle of scattering for a particular nuclide. Figure 2-1 shows (a) the ratio E_n / E_o versus A for various values of θ; and (b) E_n / E_o versus θ for various scattering nuclides. Table 2-1 lists the ratios E_n / E_o, calculated (equations 2.1 and 2.2) for a number of scattering nuclides at $\theta = 45°$, 90° and 150°. Two important features of elastic scattering are evident from figure 2-1 and Table 2-1. Firstly, from figure 2-1(a) it can be seen that for a given laboratory angle, the scattered neutron energy is greater for the light nuclides than for the heavy nuclides; and secondly, from figure 2-2(b) it can be seen that the energy difference for elastically scattered neutrons increases between the nuclides as the laboratory angle increases towards the backward direction.

From equations 2.1 and 2.2 it follows that the energy E_n of the scattered neutron is bounded in range between

$$\xi E_o < E_n < E_o \tag{2.3}$$

where the limits correspond to scattering at $\cos\theta = +1$ and -1, or $\theta = 0°$ and 180°, respectively. For $A > 1$, the energy E_n of elastically backscattered neutrons ($\theta = 180°$), is given by the formula

$$E_n = E_o \xi . \tag{2.4}$$

Therefore, if E_n can be measured sufficiently accurately then the kinematics of this process provides a basis for determining the mass of the scattering nuclide. For $\theta \rightarrow 180°$ the situation is analogous to the well-known technique of Rutherford backscattering (RBS) in which energetic charged particles are used to analyze the elemental composition of thin films or surfaces. The neutrality of the neutron gives neutron scattering the capacity for analyzing an extended sample

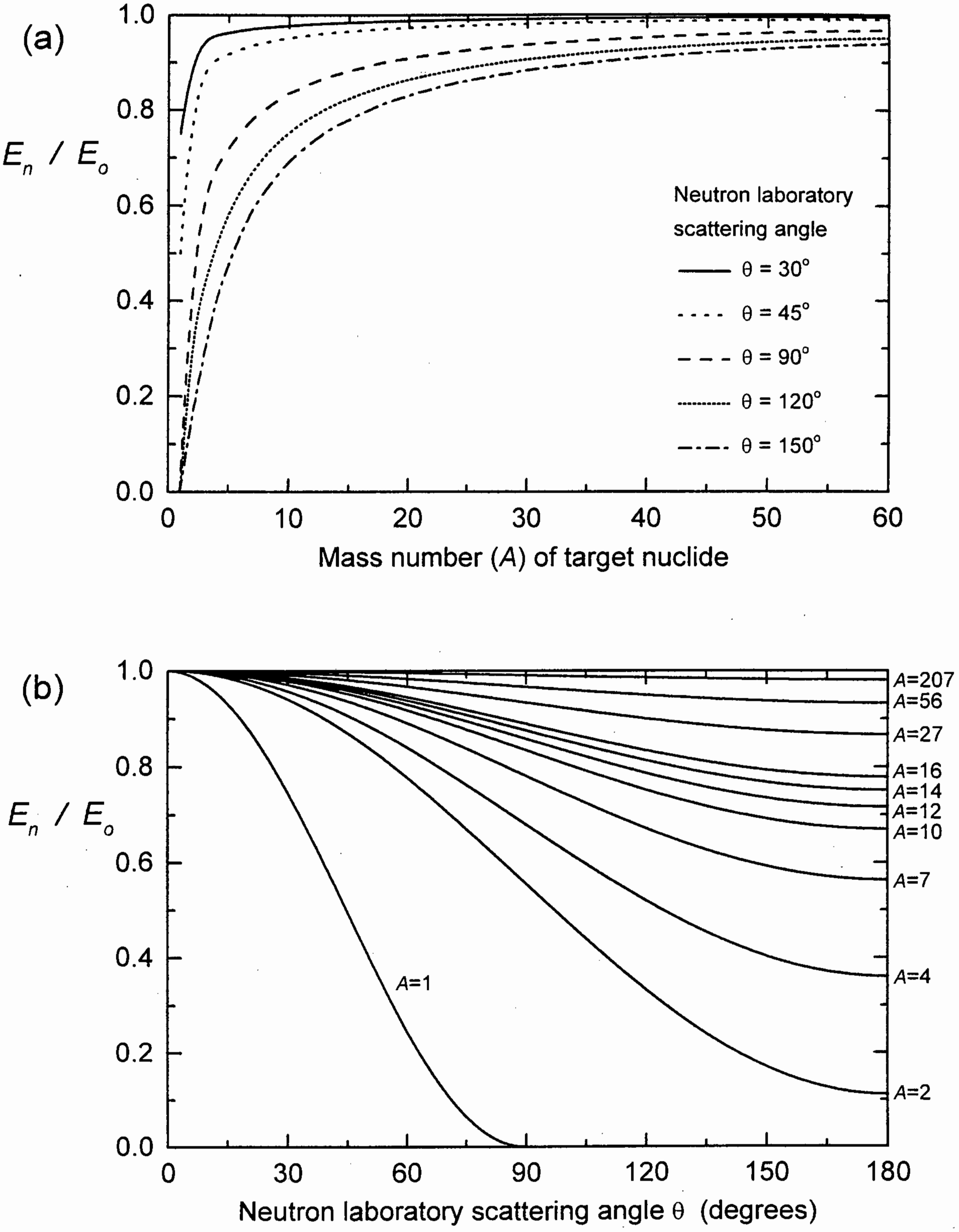

Figure 2-1 *(a) Ratio of scattered (E_n) to incident (E_o) neutron energies as a function of mass number (A) of target nuclide, calculated for the laboratory angles θ = 30°, 45°, 90°, 120° and 150°; and (b) ratio of scattered to incident neutron energies as a function of laboratory scattering angle for a range of target nuclides.*

in depth, thus suggesting the possibility of using this method for non-intrusive interrogation of bulk materials. For scattering from a hydrogen nucleus ($A = 1$), it follows from equations 2.1 and 2.2 that

$$E_n = E_o\left(\frac{1+\cos\Theta}{2}\right) = E_o \cos^2\theta \qquad (2.5)$$

where θ is kinematically confined to angles in the forward direction ($\theta < 90°$). Therefore, any system based on the detection of scattered fast neutrons requires detectors in the forward direction if the presence of hydrogen in the interrogated object is to be monitored.

Table 2-1 Ratios E_n / E_o calculated at laboratory angles $\theta = 45°$, $90°$ and $150°$ for selected scattering nuclides.

Scattering nuclide	ξ	E_n / E_o		
		$\theta = 45°$	$\theta = 90°$	$\theta = 150°$
^{1}H	0.000	0.500	-	-
^{4}He	0.360	0.862	0.596	0.382.
^{7}Li	0.563	0.919	0.748	0.582
^{9}Be	0.640	0.937	0.799	0.656
^{11}B	0.694	0.947	0.832	0.709
^{12}C	0.716	0.951	0.844	0.729
^{14}N	0.751	0.962	0.865	0.763
^{16}O	0.779	0.963	0.881	0.790
^{23}Na	0.840	0.975	0.916	0.849
^{27}Al	0.862	0.978	0.928	0.869
^{28}Si	0.867	0.979	0.931	0.874
^{32}S	0.882	0.981	0.939	0.888
^{40}Ca	0.905	0.985	0.951	0.910
^{48}Ti	0.920	0.988	0.959	0.924
^{52}Cr	0.926	0.988	0.961	0.929
^{56}Fe	0.931	0.990	0.964	0.935
^{63}Cu	0.938	0.991	0.968	0.941
^{118}Sn	0.967	0.996	0.983	0.966
^{184}W	0.978	0.997	0.989	0.981
^{207}Pb	0.981	0.997	0.991	0.982

2.1.2 Inelastic scattering

The data in Table 2-1 illustrate how the energy of elastically scattered neutrons decreases with increasing scatterer mass number A. At $\theta = 150°$, for example, the ratio of the elastically scattered and incident neutron energies is 0.729 for ^{12}C, 0.763 for ^{14}N and 0.790 for ^{16}O. For ^{27}Al, ^{28}Si, ^{56}Fe and ^{208}Pb the corresponding ratios are 0.869, 0.874, 0.935 and 0.982 respectively. Neutron spectrometers based on charged particle recoil detection in organic scintillators have been shown [Br94] to be capable of distinguishing between neutrons *elastically* scattered from the elements C, N and O. However, the limited pulse height resolution of particle recoil spectrometers makes them unsuitable identifying heavier elements ($A > 20$) by this method. Nevertheless, energy spectra measured for neutrons scattered from a sample may also include lower energy contributions from inelastically scattered neutrons, these energies being determined by the level structure of the target nucleus [Le78] and the energy of the incident neutrons. These additional inelastic features could facilitate the identification of medium and heavy elements, as well as the enhancing the identification of light elements.

2.2 Neutron scattering cross sections

2.2.1 The interference of partial waves

The wave function ψ_{scat} for neutrons elastically scattered from a central potential may be written, in the limit of large r, in the form [Ei88, Wo90, Kr88]

$$\psi_{\text{scat}} = \frac{A}{2ikr}\sum_{l}(2l+1)\,P_l(\cos\Theta)\,\{\,1-\eta_l\,\} \tag{2.6}$$

where k is the scattering wave number, l labels the angular momentum in the partial-wave decomposition, Θ is the centre-of-mass scattering angle, and A and η_l are complex constants related to the amplitudes of the incident and l^{th} scattered waves respectively. The amplitudes of the partial waves are not in general isotropic having an angular distribution governed by the Legendre polynomials $P_l(\cos\Theta)$.

Introducing a partial transition amplitude T_l defined as

$$T_l = \frac{1-\eta_l}{2i}, \tag{2.7}$$

the differential cross section for elastic scattering into solid angle element $d\Omega$ is then simply

$$\frac{d\sigma}{d\Omega} = \left|\frac{1}{k}\sum_{l}(2l+1)\,P_l(\cos\Theta)\,T_l\right|^2 . \tag{2.8}$$

The elastically scattered neutrons for each partial wave component therefore have an angular distribution given by the square of the l^{th} Legendre polynomial, which means, for example, that in the case of pure s-wave scattering ($l = 0$), the scattering is isotropic. On the other hand, predominantly p-wave scattering ($l = 1$), gives an angular distribution proportional to $\cos^2\Theta$.

When more than one partial wave is present, in addition to the terms associated with the individual partial waves, the summation in equation 2.8 also gives rise to cross-terms which may be understood physically as resulting from interference between pairs of partial waves. The general expression for the differential cross section is then given by

$$\begin{aligned}\frac{d\sigma}{d\Omega} &= \frac{1}{k^2}\sum_l (2l+1)^2\,[P_l(\cos\Theta)]^2\,|T_l|^2 \\ &+ \frac{1}{k^2}\sum_{l,l'} (2l+1)(2l'+1)\;P_l(\cos\Theta)P_{l'}(\cos\Theta)\;T_lT_{l'}{}^*\quad (l \neq l')\ .\end{aligned} \tag{2.9}$$

If there are only two partial waves present, equation 2.9 contains two principal terms and one interference term, for example in a situation where there is only s-wave ($l = 0$) and p-wave ($l = 1$) scattering. In this case, the differential cross section is simply

$$\begin{aligned}\frac{d\sigma}{d\Omega} &= \frac{1}{k^2}\left\{|T_0|^2 + 9(\cos^2\Theta)|T_1|^2 + 3(\cos\Theta)(T_0T_1{}^* + T_1T_0{}^*)\right\} \\ &= \frac{1}{k^2}\left\{|T_0|^2 + 9(\cos^2\Theta)|T_1|^2 + 6(\cos\Theta)\,\mathrm{Re}\,T_0T_1{}^*\right\}.\end{aligned} \tag{2.10}$$

The first two terms in equation 2.10 both have backward-forward symmetry, but if the interference term is positive in the forward hemisphere, it is negative in the backward hemisphere and vice versa. This type of forward-backward asymmetry is likely to occur whenever partial waves of even l interfere with partial waves of odd l.

For example, figure 2-2 shows Legendre polynomial coefficients P_l determined [Kn82] for the Legendre polynomial expansion of the differential ^{12}C(n,n)^{12}C cross section, for $l = 0$ to 4. The curves in the figures are the results of fits to the data based on R-matrix calculations [Kn82]. The structure in these curves is attributed to the anisotropies present in the differential cross section for ^{12}C(n,n)^{12}C which also varies as a function of incident neutron energy. Such variations are present in the differential cross sections for neutron scattering from all species of nuclide.

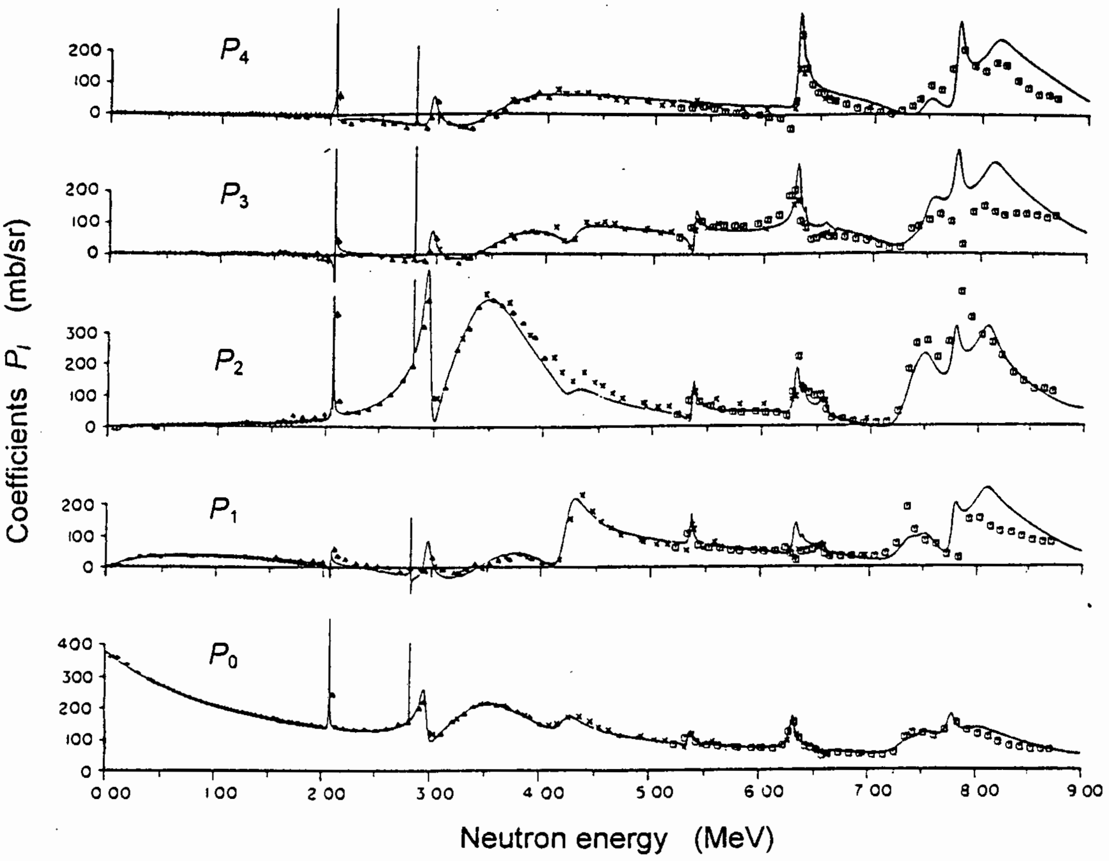

Figure 2-2 *Coefficients* P_l *in the Legendre polynomial expansion of the differential* $^{12}C(n,n)^{12}C$ *cross section for* $l = 0$ *to 4 [Kn82]. The coefficients are given in the centre-of-mass system while neutron energies are in the laboratory system. The curves are a result of R-matrix fits to the experimental data. References to the data may be found in [Kn82].*

The total cross section for elastic scattering from a central potential may be obtained by integrating the elastic scattering differential cross section over the whole solid angle of 4π steradians, giving

$$\begin{aligned} \sigma_{\text{elastic}} &= \frac{1}{k^2}\sum_l (2l+1)^2 \left|T_l\right|^2 \int_{4\pi} \left[P_l(\cos\Theta)\right]^2 d\Omega \\ &= \frac{4\pi}{k^2}\sum_l (2l+1)^2 \left|T_l\right|^2 \end{aligned} \tag{2.11}$$

which is a much simpler expression due to the absence of interference terms. In other words, the interference terms simply shift intensity from one part of the angular distribution to another, without changing the total intensity of scattering.

2.2.2 Resonant elastic scattering

If the energy of the incident neutron is low enough, typically less than 10 MeV, the neutron and target nuclide may combine to form an intermediate compound nucleus state. The process will display the characteristics of a resonance, which from a wave point of view, is caused by the interference between the wave emerging from the nucleus and the diffracted and reflected waves of the incident neutron. Often a compound nucleus state can break up in several different ways, or it may be possible to form a given intermediate state from several different sets of initial particles. These different sets of initial or final conditions are called *channels*; entrance channels for the initial particles and exit channels for the final particles. In the case of elastic scattering, the entrance and exit channels are identical.

Once the compound nucleus is formed, the nucleons have a chance of interacting with each other many times, resulting in a loss of identity of the original neutron and target. The decay of the system is then determined primarily by the amount of excitation energy available to each exit channel. At low energies (< 4 MeV), the lifetimes of the excited states in a system are relatively long, of the order of 10^{-14} s, since the number of open exit channels is small. This results in the level width Γ of the compound state being narrow, as it is related to the lifetime τ of the state by the Heisenberg relation

$$\tau = \frac{\hbar}{\Gamma} . \tag{2.12}$$

A phenomenological description of the energy dependence of a single resonance in the case of pure elastic scattering is given by the Breit-Wigner level one formula [Bl52, Ei88]

$$\sigma_{\text{resonance}}(E) = \frac{\pi}{k^2}(2l+1)\,\frac{\Gamma^2}{\left\{(E-E_o)^2 + \frac{1}{4}\Gamma^2\right\}} \tag{2.13}$$

where E_o is the energy corresponding to the peak of the resonance. When one entrance channel can lead to more than one exit channel, each process will have its own cross section and it becomes necessary to modify equation 2.13.

In summary, the elastic channel of the neutron scattering cross section has two components, a nonresonating part with an amplitude proportional to k^{-2} (equation 2.11) and a resonating part (equation 2.13) containing the energy dependent factor $(E-E_o)$ in the denominator. The resonant term $\{(E-E_o)^2 + \frac{1}{4}\Gamma^2\}$ in equation 2.13 describes the basic shape of the resonances but it is not the only energy-dependent term, since k^{-2} also varies as E^{-1} (equation 2.11). Nonresonating potential scattering contributes a smooth, or shape-elastic, component to the elastic cross section, while as $E \rightarrow E_o$ the elastic cross section is dominated by resonant scattering.

2.2.3 Features in the HCNO cross sections for FNSA

Considerable effort has been devoted to the accurate measurement of total cross sections, angular distributions, phase shifts, resonance parameters, and other observables, which are necessary to describe the physics of the various neutron-induced interactions possible with different nuclei. These data are continuously being evaluated and made available from bureaus such as the International Atomic Energy Agency [IAEA] in useful forms such as neutron cross section libraries, for example ENDF [Ro91] and JENDL [Na95].

Figures 2-3 to 2-6 show measurements [Mc88] of the total cross sections for neutron interactions with ^{1}H, ^{12}C, ^{14}N and ^{16}O respectively, and curves which result from the ENDF/B-V evaluations [Mc88] of these data. A more recent evaluation (ENDF/B-VI) [Ro91] of the total cross sections for neutron scattering from ^{1}H, ^{12}C, ^{14}N and ^{16}O are shown together in figure 2-7. Since the density of states in the compound nuclei formed in neutron capture by these nuclides is small for incident neutron energies between 0.1 MeV and 5 MeV, the mean spacing between states is typically much larger than Γ, and isolated sharp resonances dominate the elastic cross sections. Resonance structure is seen, for example, at 2.1 MeV, 2.9 MeV, 6.3 MeV and 7.7 MeV for $^{12}C(n,n)^{12}C$; 2.9 MeV, 3.6 MeV and 4.2 MeV for $^{14}N(n,n)^{14}N$; and in the many sharp peaks between 0.4 MeV and 9.0 MeV for $^{16}O(n,n)^{16}O$. Figure 2-8 shows perspective plots of the ENDF-VI evaluations [Ro91] of the differential cross sections for neutron elastic scattering from (a)^{12}C , (b)^{14}N and (c)^{16}O as a function of incident neutron energy between 1.0 MeV and 8.0 MeV. These cross sections display considerable structure both as a function of incident neutron energy and angle of scattering. Figure 2-9 shows the differential cross sections for $^{12}C(n,n)^{12}C$, $^{14}N(n,n)^{14}N$ and $^{16}O(n,n)^{16}O$ selected at (a) $\theta = 45°$ and (b) $\theta = 150°$ from the data of the form shown in figure 2-8 at the appropriate centre-of-mass angle. The variations in these differential cross sections suggest that scattering measurements made at two or more suitably chosen incident neutron energies will be characteristic of the scattering nuclide. Moreover, the intensities of these cross sections also vary distinctively with scattering angle. This is illustrated in figure 2-9(c) which shows the ratios of the differential cross sections at 45° (figure 2-9(a)) to those at 150° (figure 2-9(b)). Thus if the incident energy is suitably chosen and scattered neutrons are detected at two or more angles, one forward (e.g. 45°) and the other backward (e.g. 150°), then the ratio of the intensities of forward to backward scattering will also be characteristic of the scattering nuclide.

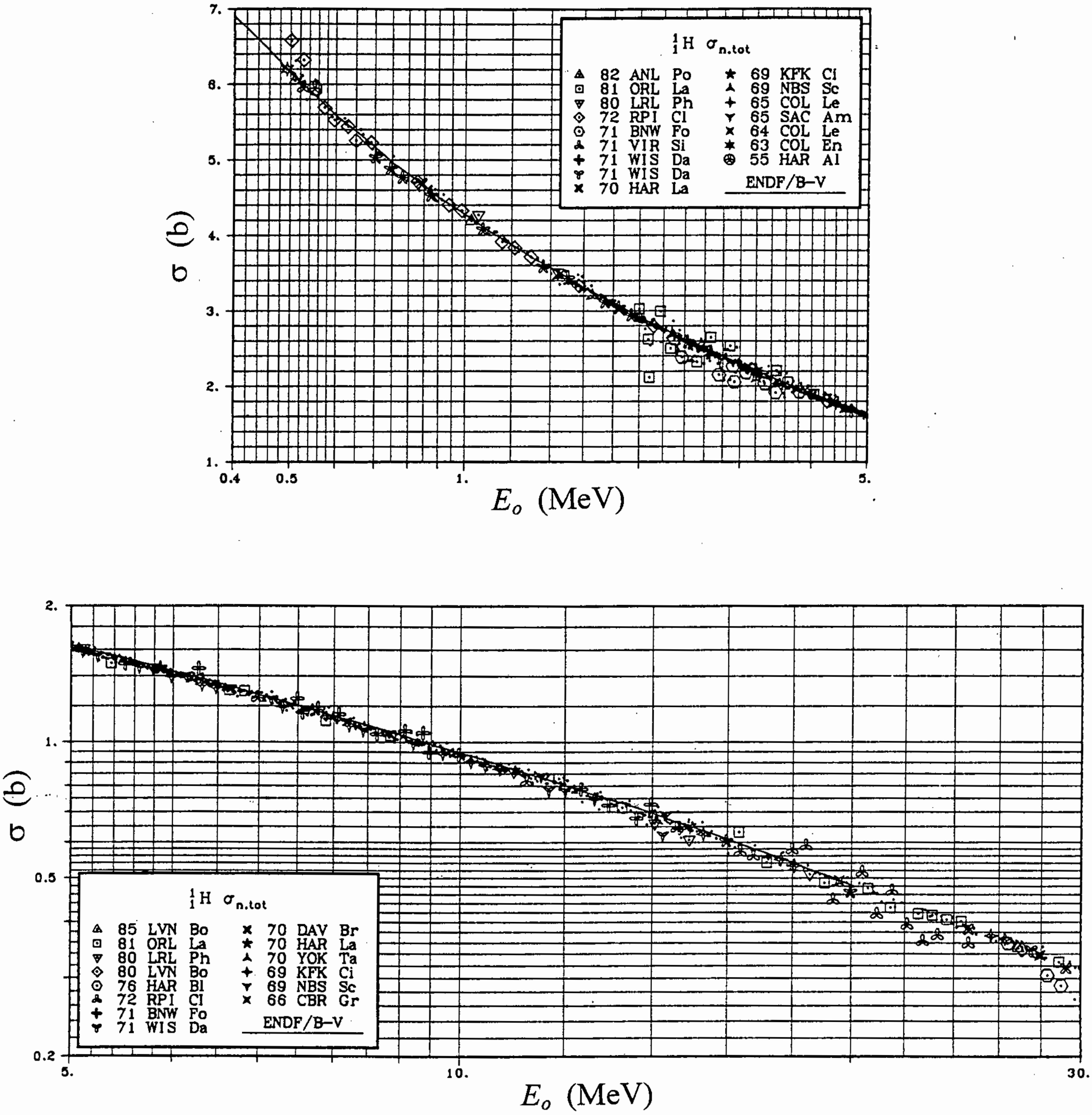

Figure 2-3 *Total cross section for neutron interactions with ^1H as a function of incident neutron energy [Mc88]. The curve shows the ENDF/B-V evaluation of the data [Mc88].*

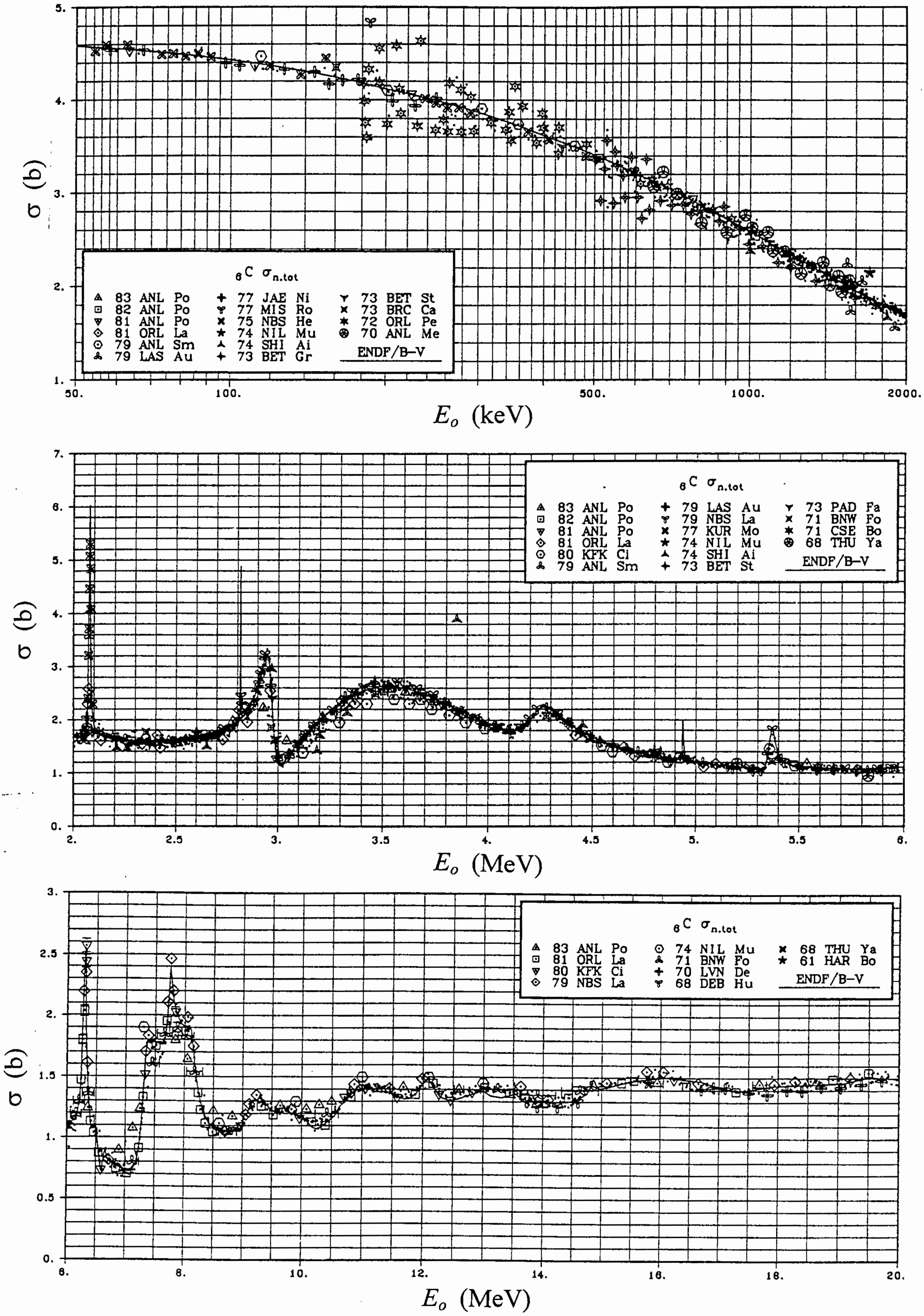

Figure 2-4 *Total cross section for neutron interactions with ^{12}C as a function of incident neutron energy [Mc88]. The curve shows the ENDF/B-V evaluation of the data [Mc88].*

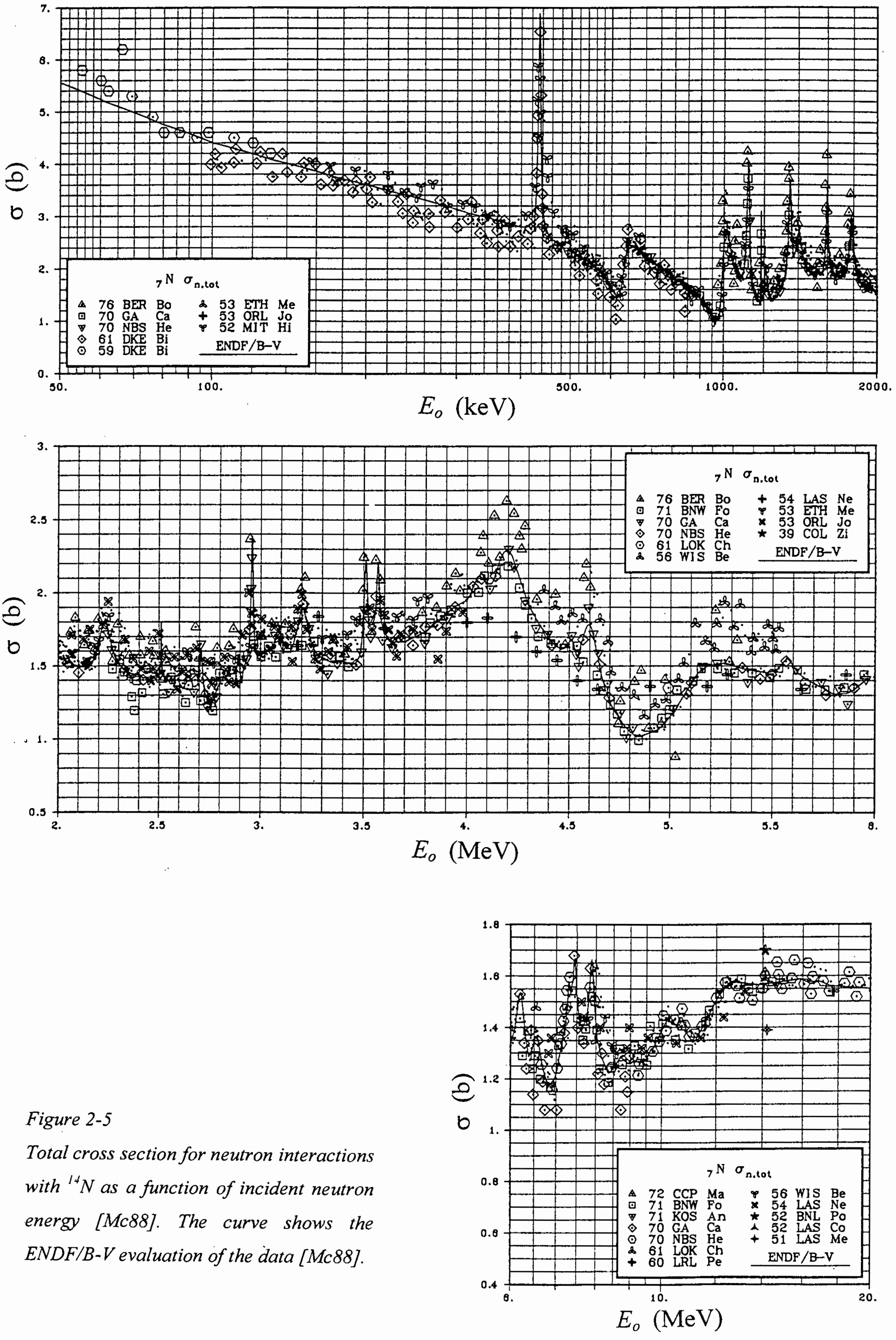

Figure 2-5

Total cross section for neutron interactions with ^{14}N as a function of incident neutron energy [Mc88]. The curve shows the ENDF/B-V evaluation of the data [Mc88].

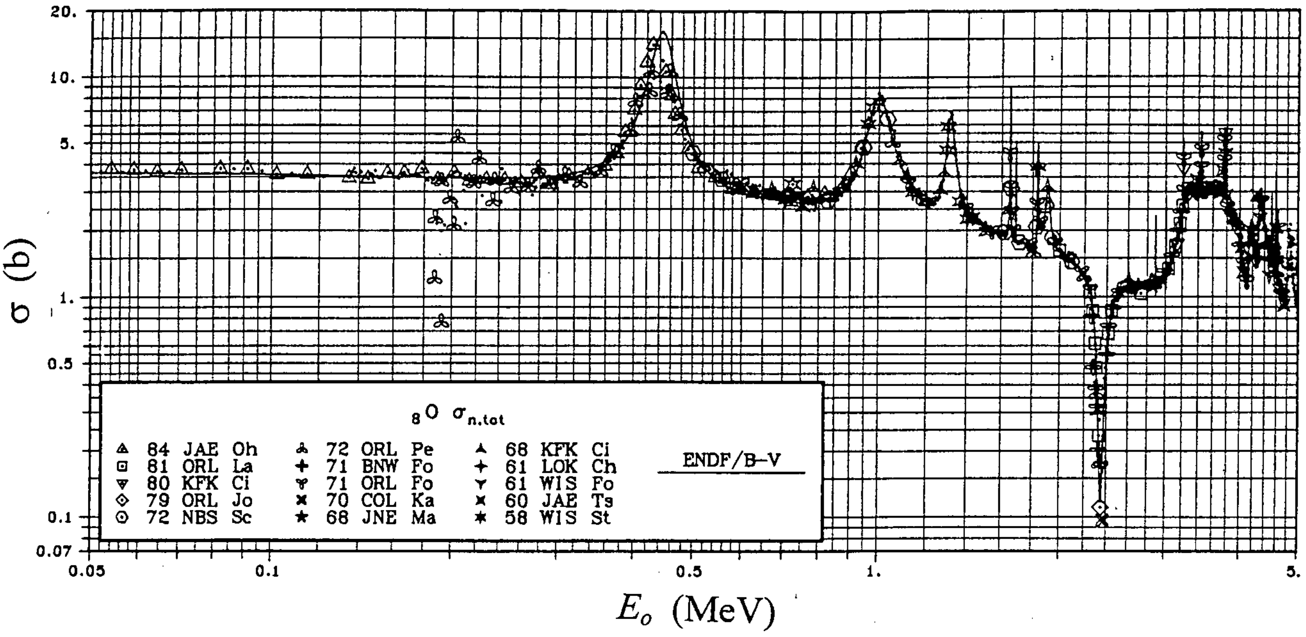

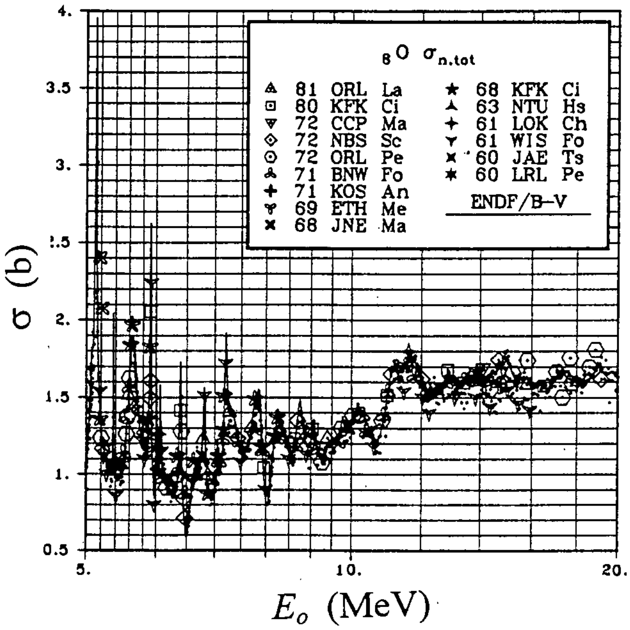

Figure 2-6 *Total cross section for neutron interactions with ^{16}O as a function of incident neutron energy [Mc88]. The curve shows the ENDF/B-V evaluation of the data [Mc88].*

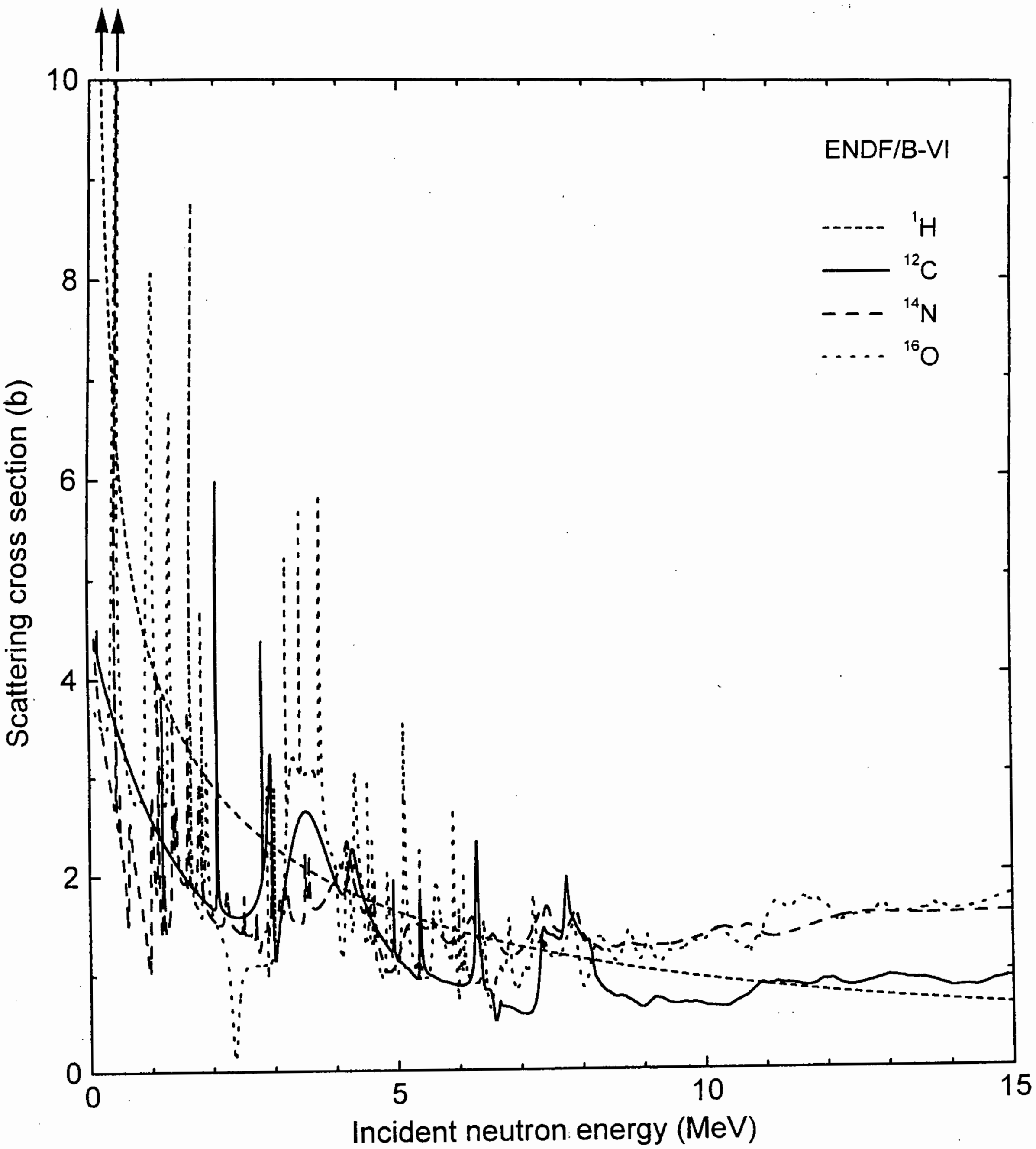

Figure 2-7 *ENDF/B-VI evaluations [Ro91] of the cross sections for neutron scattering from ^1H, ^{12}C, ^{14}N and ^{16}O.*

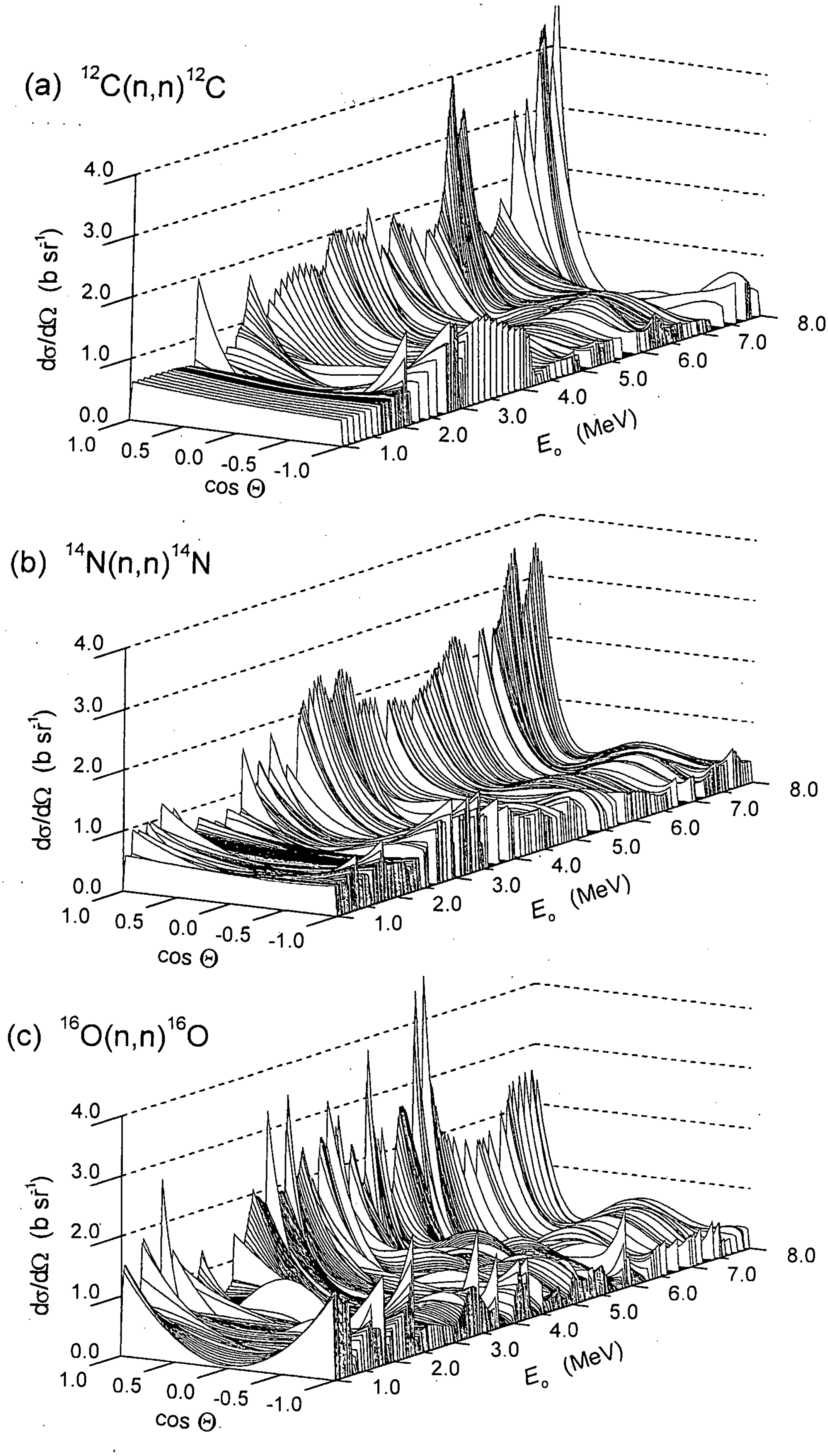

Figure 2-8 ENDF/B-VI evaluations [Ro91] of the differential cross sections for (a) $^{12}C(n,n)^{12}C$; (b) $^{14}N(n,n)^{14}N$; and (c) $^{16}O(n,n)^{16}O$, for incident neutron energies between 1.0 MeV and 8.0 MeV.

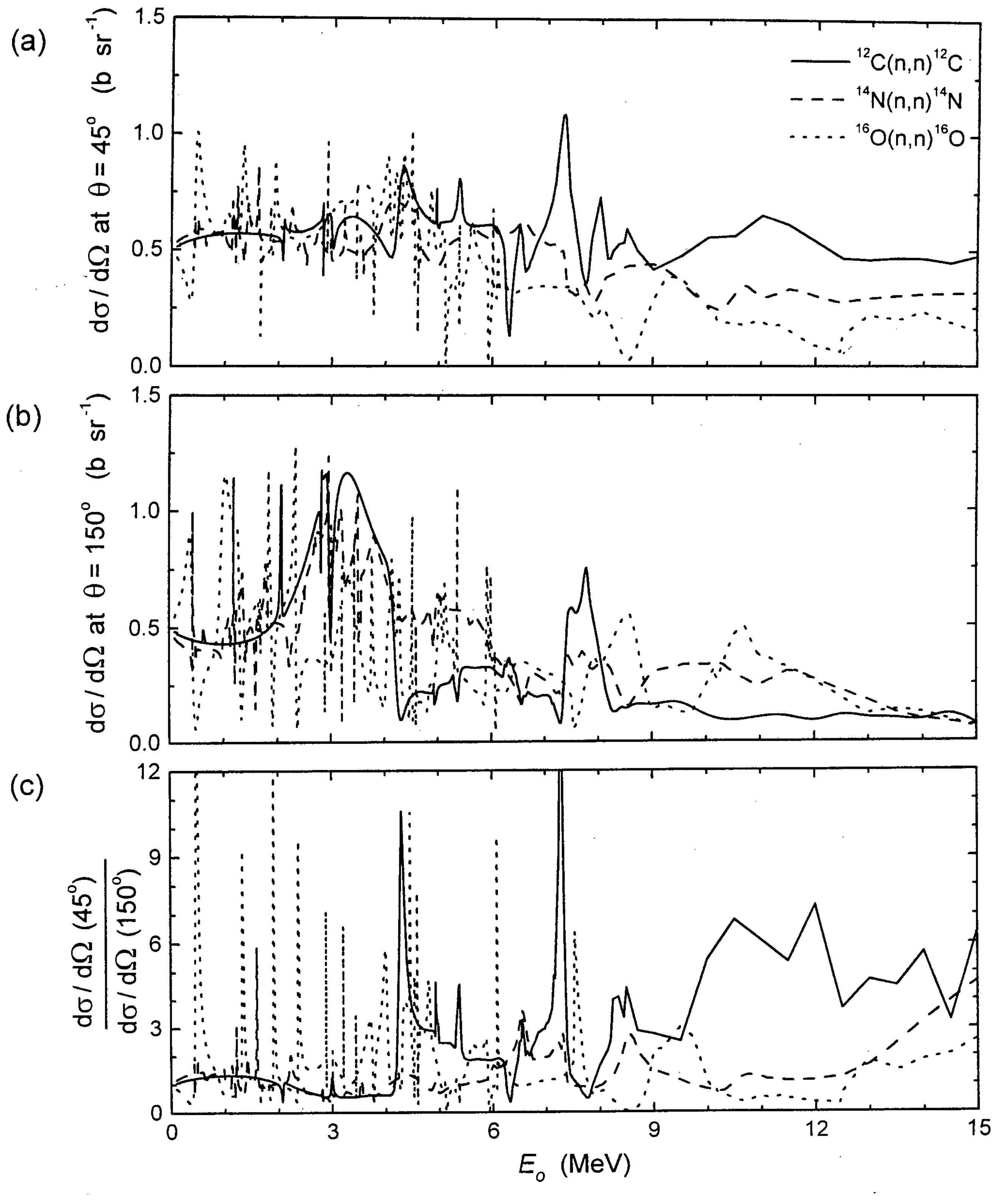

Figure 2-9 ENDF/B-VI evaluations [Ro91] of the differential cross sections for $^{12}C(n,n)^{12}C$, $^{14}N(n,n)^{14}N$ and $^{16}O(n,n)^{16}O$ for incident neutron energies between 0.1 MeV and 15.0 MeV at the laboratory scattering angles of (a) 45° and (b) 150°. Panel (c) shows the ratios of the differential cross sections at 45° to the differential cross sections at 150°.

2.3 Preliminary experiments

The differential cross sections of the form illustrated in figure 2-9 are convenient in that they succinctly provide summaries based on the evaluations of the data from many different experiments. The structure evident in these differential cross sections may be used as a guide to select energies suitable for FNSA applications. However, caution needs to be applied when interpreting the data from these libraries and the features in the cross sections can only be used with confidence after being assessed through independent measurement. Consequently exploratory time-of-flight measurements were made for neutrons of incident energy between 5 MeV and 28 MeV scattered from samples comprised of the nuclides ^{12}C, ^{14}N, and ^{16}O, in order to facilitate the selection of particular neutron energies for further FNSA study.

2.3.1 Measurements

Scattering experiments were carried out using the k = 200 separated-sector cyclotron facility at the National Accelerator Centre [NAC], South Africa. The main features of the experimental arrangement are shown schematically in figure 2-10. A pulsed neutron beam of energies up to 28 MeV was produced via the ^{9}Be(p,n)^{9}B reaction (Q-value of −1.85 MeV [Go72]) by directing bursts of 30.0 MeV protons, of time dispersion 264.6 ns, onto a 5.0 mm thick beryllium target. The target consisted of natural beryllium metal compressed between 2.0 μm Havar foils and mounted on a water cooled copper block which also served as a beam dump for the protons which were transmitted through the target.

A collimated neutron beam was formed at 0° in the experiment vault by an aperture (50 mm × 50 mm) in a shielding wall comprised of 2.0 m of iron and 0.9 m of borated wax. Scattering samples of graphite, liquid nitrogen and water were placed in turn on a light aluminium stand at 0°. The graphite (52 mm ϕ × 100 mm) and water (65 mm ϕ × 110 mm) samples were orientated such that their axes were perpendicular to the incident beam direction and the liquid nitrogen was contained in a spherical Dewar of internal diameter 8 cm. The profile of the beam was previously measured [Al96] to have a uniform width of more than 7 cm at the sample position.

A deuterated NE230 liquid scintillator (detector B, see Section 3.1.1) of dimensions 40 mm ϕ × 30 mm was mounted at scattering angle 150° at a distance of 20 cm from the sample position. An NE102 scintillator (25 mm × 25 mm × 5 mm) was mounted 3.5 m from the target near the exit of the collimator, as indicated in figure 2-10, to monitor the incident neutron beam. The counts from this detector in a time-of-flight window were proportional to the number of

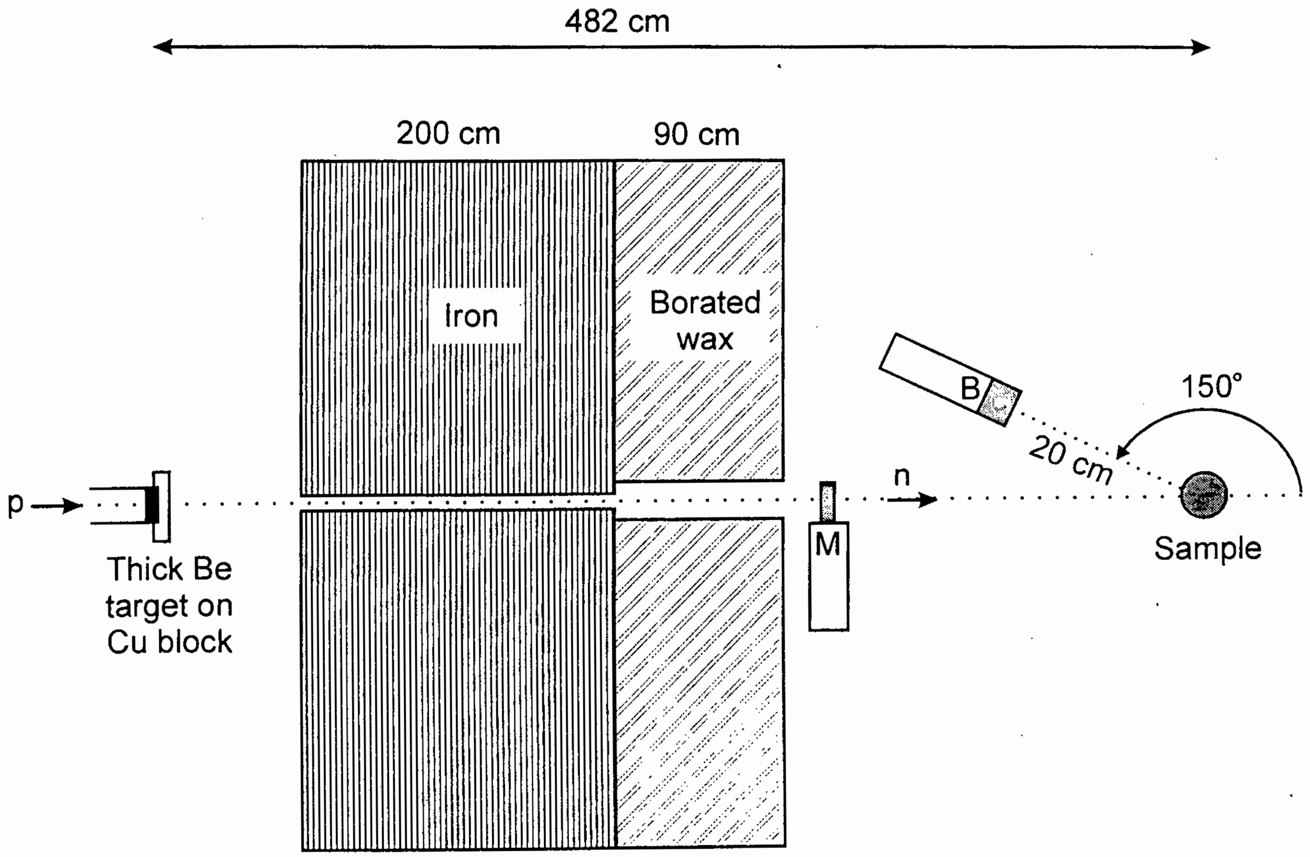

Figure 2-10 *Schematic representation of the experimental layout used for the time-of-flight scattering studies using the neutron spectrum obtained from bombarding a 30 MeV proton beam onto a 5.0 mm thick natural beryllium target. The neutrons scattered from samples mounted at 4.8 m from the target were detected by a NE230 liquid scintillator (40 mm ϕ × 30 mm) placed at laboratory angle 150°.*

neutrons produced in the target. Since the acceptance angle of the scattering samples remained the same throughout the experiment, the counts measured by the monitor were therefore also proportional to the number of neutrons irradiating the samples. Furthermore, as the number of nuclei in the beryllium target remained constant, the neutron dose was proportional to the integrated beam current on the target. The beam current integrator was therefore used to check the data given by the monitor detector.

Details of the data acquisition system are described later in Section 3.1.3. Pulse shape discrimination was used to suppress backgrounds in detector B arising from the interactions of γ-rays. The outputs from the anode of the photomultiplier of detector B were fed directly into a modified [Sm86] Link Systems Model 5010 Pulse Shape Discriminator (LINK) [Ad78] which provided two outputs, L and F (see Section 3.1.3). The LINK also provided a timing pulse for each processed event which was used to start the time-to-amplitude converter (TAC) that measured the scattered neutron time-of-flight T_n. This TAC was stopped using a pulse synchronised to the radio frequency of the cyclotron. The neutrons scattered from the vault walls and floor, from the sample supports, and through the collimator wall produced random and time-dependent background in detector B. Therefore background was measured for the empty sample container, the empty Dewar and for no sample in position.

The scattering data were replayed off-line and analyzed event by event in multiparameter mode. A scintillation pulse shape parameter S [Sm86, Sm87] was derived from the L and the F parameters by combining them in the form

$$S = L - kF + C$$

where k and C are arbitrary constants which are set in the off-line analysis of the data. The value of k determines the angle of the loci in the L-S distributions (see below) and the value of C sets the position of the data on the S-axis.

Figure 2-11 shows a perspective plot of counts (vertical) as a function of L and S, for neutrons scattered from the graphite sample and measured by detector B at 150°. Each charged particle recoiling from neutron induced interactions in detector B has a particular combination of pulse height (L) and pulse shape (S) values which characterizes its type and energy. This results in distinct well-defined ridges being resolved on the L-S plane, which are clearly distinguished at higher values of L but merge with decreasing pulse height due to poorer photomultiplier statistics. The ridges, as labeled in figure 2-11, are associated [Bu90] with protons (p) produced in the breakup of the deuterons and carbon nuclei, deuterons (d) recoiling from n-d elastic scattering and n-^{12}C reactions, and alpha particles (α) produced in ^{12}C(n,α)^{9}Be and ^{12}C(n,n')3α reactions in the detector. The presence of these loci allows the selection of a particular type of charged particle through the means of a software cut imposed onto the L-S plane. One such cut (also shown in figure 2-11) was used to select those events associated with the detection of deuterons in detector B and only these events were accepted for further analysis.

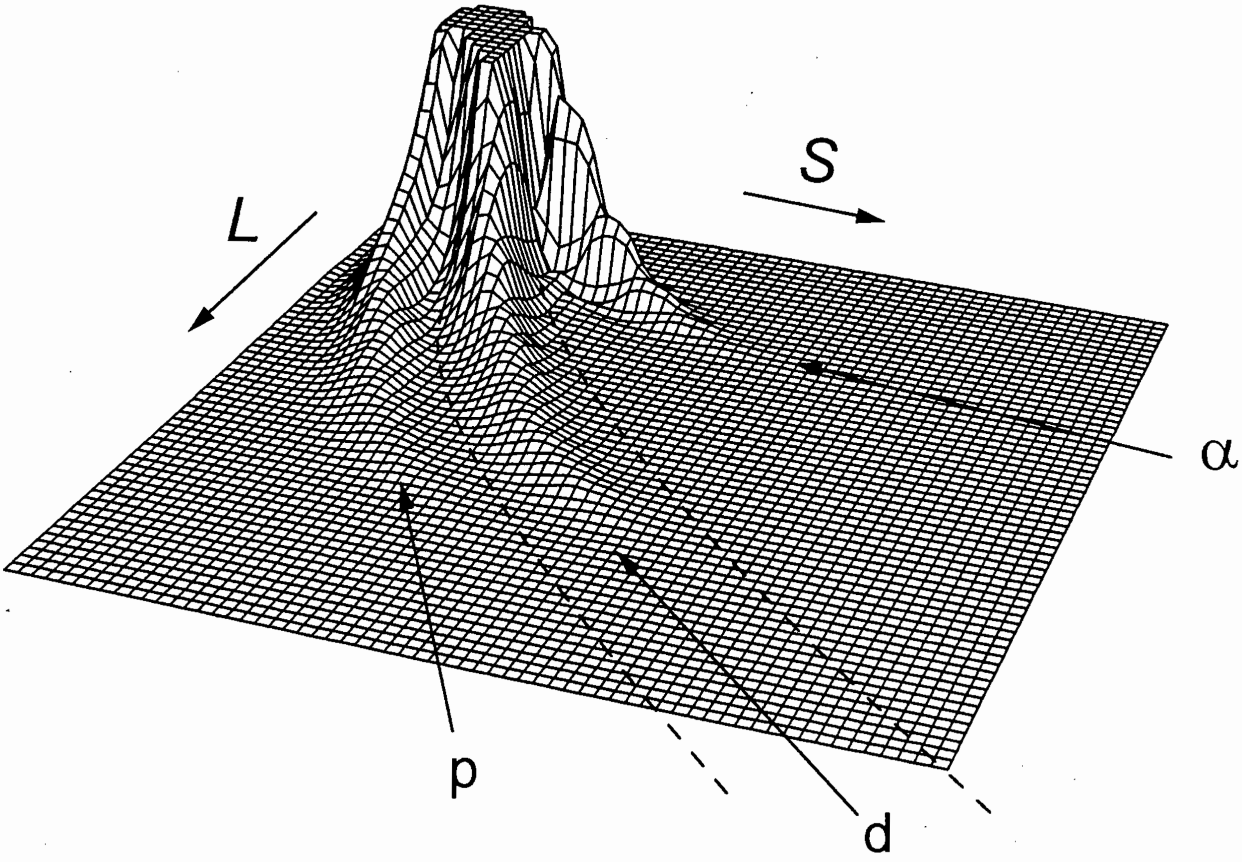

Figure 2-11 Counts (vertical) as a function of pulse height parameter (L) and pulse shape parameter (S) for events in an NE230 liquid scintillator (40 mm ϕ × 30 mm) when exposed to the neutrons scattered from a graphite sample (52 mm ϕ × 100 mm). The incident neutron beam was produced by bombarding a 5.0 mm thick beryllium target with 30 MeV protons. The loci are associated with the detection of (p) protons, (d) deuterons and (α) alpha particles recoiling from neutron-induced interactions in the detector. Also shown is a cut selecting only those events associated with recoiling deuterons.

Figure 2-12 shows an event density plot of pulse height L versus time-of-flight parameter T_n measured by detector B for neutrons scattered from the water sample. The events shown have been selected by the PSD deuteron cut illustrated in figure 2-11. A software cut was chosen as indicated in figure 2-12 to select the ridge on the L-T_n plane, labeled D_f, which is attributed to deuterons recoiling forward from n-d elastic scattering events in the scintillator, and exclude those events associated with n-^{12}C interactions. The contours in the event distribution bounded by the D_f cut reflect the structure in the n-^{16}O total scattering cross-section at this laboratory angle of 150°. Identical software cuts were imposed for the scattering data recorded for the graphite and liquid nitrogen scatterers.

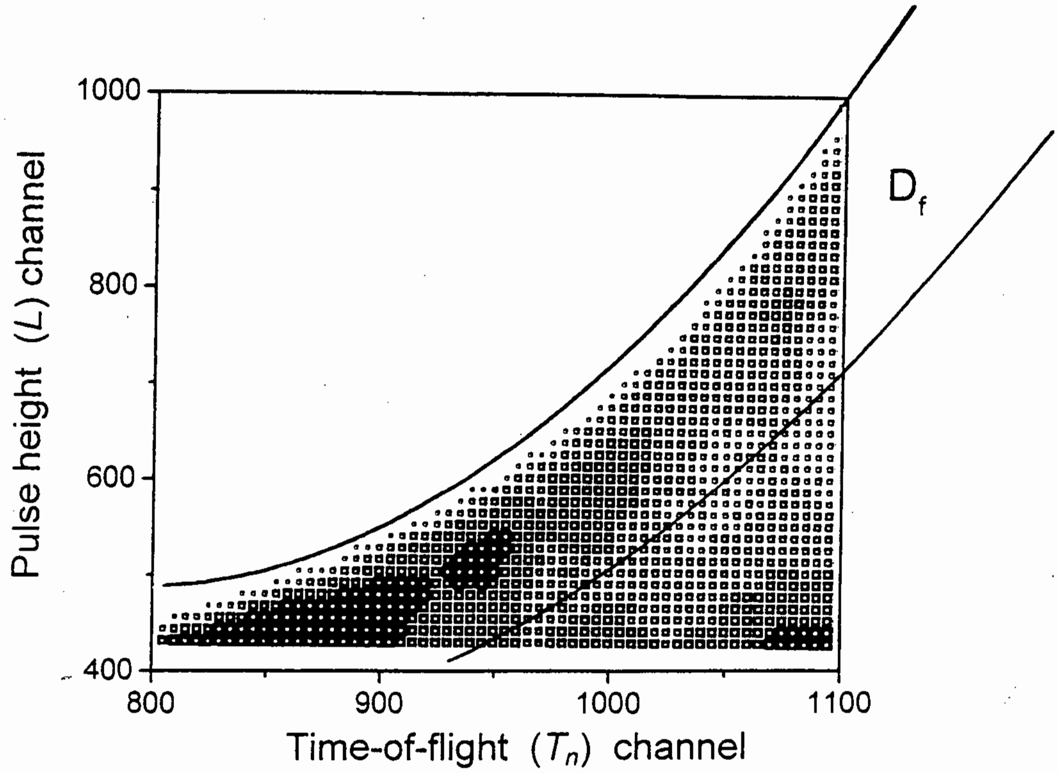

Figure 2-12 Density plot of pulse height parameter (L) versus time-of-flight parameter (T_n) for events in an NE230 liquid scintillator (40 mm ϕ × 30 mm) selected by the deuteron cut shown in figure 2-11, for neutrons scattered from a water sample (65 mm ϕ × 110 mm). Also shown is a cut (D_f) chosen to select only the data associated with deuterons recoiling forward from n-d elastic scattering events in the detector. The points, in order of increasing size, represent count thresholds of 32, 64, 128 and 256.

2.3.2 Features in the scattering yield for FNSA

Figure 2-13 shows time-of-flight (T_n) spectra measured by detector B at 150° for neutrons scattered from the graphite, liquid nitrogen and water samples, and selected by both the deuteron *L-S* cut (figure 2-11) and the forward deuteron recoil L-T_n cut (figure 2-12). The scales in figure 2-13 have been normalized so as to correspond to the counts that would be registered for the same number of incident neutrons (indicated by a standard count from the monitor detector) and to $100N_A$ target nuclei (^{12}C, ^{14}N or ^{16}O) in the scattering sample, where N_A is Avogadro's number. The decreasing yield at T_n channels less than about 850 in figure 2-13 is due to the pulse height threshold used for the measurements, corresponding to a recoil deuteron energy of approximately 3 MeV. An energy scale (in MeV) for the T_n-spectrum, calculated using the standard neutron time-of-flight relationships [Kn89], is also indicated in the figure.

The specific neutron yield at 0° for a thick beryllium target varies smoothly with energy [Lo81] as does the neutron detection efficiency of liquid scintillators over this energy range

[Ve68]. Therefore the features in the measured scattering yield (figure 2-13) are primarily governed by the differential scattering cross sections at this laboratory angle. This allows comparisons to be made over narrow energy ranges between the relative scattering yields measured for each of the three nuclides studied. The most striking feature in figure 2-13 is the strong peak centred at 7.5 MeV in the carbon spectrum. The relative (C:N:O) scattering yield at 7.5 MeV is measured to be approximately 2.9 : 1.5 : 0.7 , while at 6.8 MeV, the corresponding values are 0.8 : 1.4 : 1.2. These values are consistent with the predictions made by the differential cross sections at these energies (figure 2-9(b)). Based on these results, the two incident neutron energies of 6.8 MeV and 7.5 MeV were chosen for further FNSA studies. Chapter 3 describes the various approaches of elemental analysis which were explored based on the detection of scattered neutrons. Although subsequent focus was mainly at these two energies, it was recognized that an elemental analysis system based on the detection of scattered neutrons could make use of incident neutron beams of lower or higher energies.

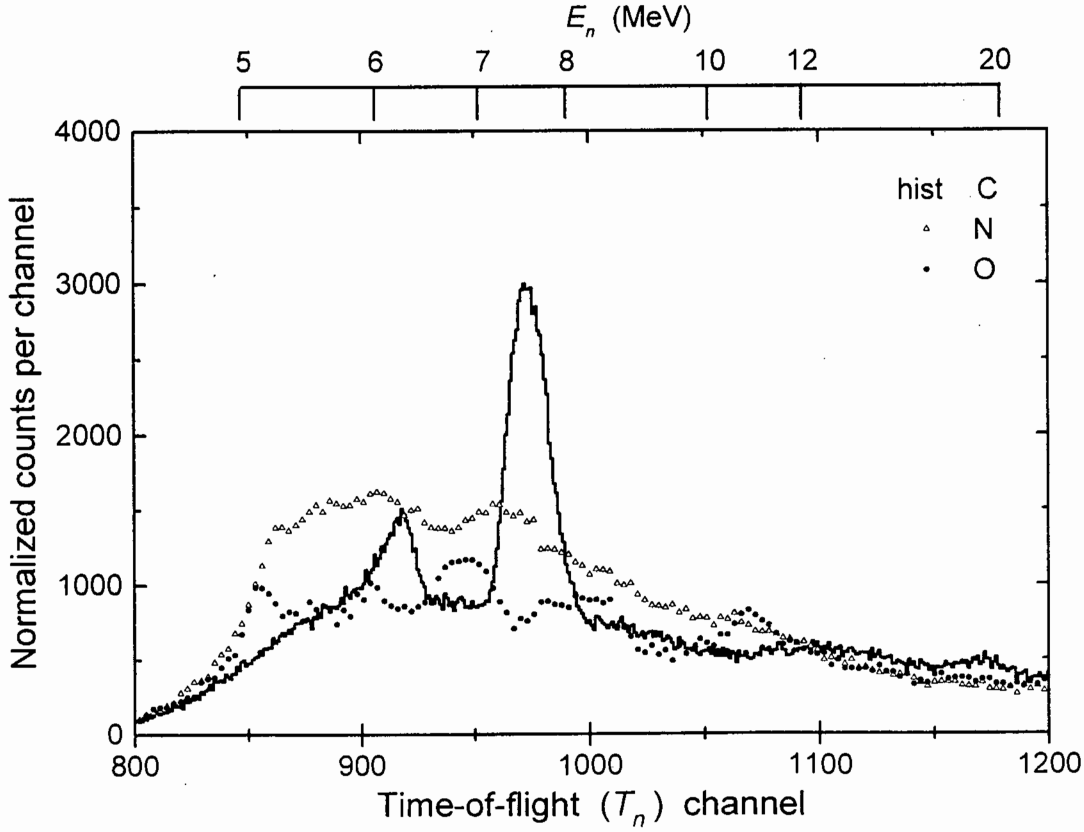

Figure 2-13 Neutron time-of-flight (T_n) spectra measured for neutrons scattered from samples of graphite, liquid nitrogen and water. The data have been corrected for background and normalized so as to correspond to the counts that would be registered for a standard number of incident neutrons and to $100N_A$ scattering nuclides (^{12}C, ^{14}N or ^{16}O) in the scatterer. Time-of-flight increases to the left at a rate of 0.241 ns/channel and neutron energy is shown by the upper scale.

Chapter 3

Element analysis by FNSA

Table 3-1 summarizes selected features of the 14 run series during which data described in the present work were measured. The experimental work was primarily undertaken at the facilities of the National Accelerator Centre [NAC], South Africa, during the period from December 1995 to March 1998, representing a total of about 1600 hours of beamtime. Section 2.3 described preliminary time-of flight measurements which were completed in order to facilitate the selection of suitable incident neutron energies (6.8 MeV and 7.5 MeV) for further FNSA studies. The subsequent work divides into two distinct phases (see Table 3-1). The initial studies (Phase 1), the subject of this chapter and the next, explored various approaches of elemental analysis based on the detection of scattered neutrons, which were introduced in Chapter 2. The exploratory (Phase 1) experiments focussed mainly on the elements H, C, N and O and were aimed at demonstrating that information on the type of scattering nuclide may be obtained from an analysis of measurements of scattered neutron energy spectra. Pulse height and time-of-flight measurements were made of neutrons which were elastically and inelastically scattered from mono-elemental samples. Distinctive nuclide-specific features in the scattering data were used to produce *scattering signatures* for the elements H, C, N and O. These scattering signatures facilitated the deconvolution (Chapter 4) of scattering signatures measured for HCNO samples of unknown composition in order to measure the relative proportions of each species of nuclide in the sample.

Table 3-1 *Summary of experimental runs.*

	Date	***Run code***	***Acc. ions***	***Target***	***Neutron energy at 0° (MeV)***	***Shielding***	***Detector angles***	***Comment***
	July 1995	CNG	p	thick Be	5 – 28	Collimator	150°	Selection of incident neutron energies .
Phase 1	Oct 1995	CNH	d	D_2 gas (1.0 atm)	7.5	Shadow shield	150°	Exploratory scattering runs.
	Dec 1995	CNI	d	D_2 gas (1.0 atm)	6.8 & 7.5	Shadow shield	150°	Beam failure.
	Jan 1996	CNJ	d	D_2 gas (1.0 atm)	6.8 & 7.5	Shadow shield	150°	Development of geometry.
	Mar 1996	CNK	d	D_2 gas (1.0 atm)	6.8 & 7.5	Shadow shield	150°	Pulse height (L) and TOF measurements.
	Apr 1996	CNL	d	D_2 gas (1.0 atm)	6.8 & 7.5	Shadow shield	150°	Element analysis by backscattering.
	Sept 1996	CNM	d	D_2 gas (1.0 atm)	6.8 & 7.5	Shadow shield	150° & 45°	First scattering signatures.
Phase 2	Mar 1997	CNN	d	D_2 gas (1.0 atm)	7.5	Collimator	150° & 45°	New geometry.
	Apr 1997	CNP	d	D_2 gas (1.0 atm)	6.8	Collimator	150° & 45°	Multiple samples.
	May 1997	CNQ	d	D_2 gas (1.0 atm)	6.8 & 7.5	Collimator	150° & 45°	Automatic energy cycling.
	Sept 1997	CNR	d	D_2 gas (1.0 atm)	6.8 & 7.5	Collimator	150° & 45°	New scattering signatures.
	Oct 1997	CNS	d	D_2 gas (1.0 atm)	7.5	Collimator	150° & 45°	Preliminary runs with RT-scanner.
	Dec 1997	CNT	p	thin Li	variable 2.2 - 2.5	Collimator	150°, 45° & 0°	Exploratory runs at low energies.
	Mar 1998	CNU	d	D_2 gas (0.5 atm)	4.0 & 4.5	Collimator	150°, 45° & 0°	RT-scan measurements.

3.1 Equipment and calibrations

3.1.1 The neutron detectors

Two types of liquid scintillator, NE213 † and (deuterated) NE230, chosen primarily for their pulse shape discrimination (PSD) abilities and response characteristics, were used for neutron detection in the present investigations. A few physical properties of these scintillators are listed in Table 3-2.

Table 3-2 A few physical characteristics of NE213 and NE230 scintillators [NE].

	NE213 (BC-501A)	*NE230 (BC-537)*
Light output (relative to anthracene)	78%	60%
Density	0.874 g cm^{-3}	0.945 g cm^{-3}
No. of H atoms per cm^3	4.82×10^{22}	3.55×10^{20}
No. of D atoms per cm^3	-	4.06×10^{22}
No. of C atoms per cm^3	3.98×10^{22}	4.10×10^{22}
No. of electrons per cm^3	2.87×10^{23}	2.87×10^{23}
H:C Ratio (NE213) / D:C (NE230)	1.212	0.984
Wavelength of maximum emission	425 nm	425 nm
Decay time of fast component	3.7 ns	3.0 ns

Many papers concerning the light output of organic scintillators, their detection efficiencies and response to neutrons and photons have been published and reviewed in articles such as [Br79, Br97]. Deuterated scintillators are considerably more expensive than natural organic scintillators, but might nevertheless be preferred for FNSA applications since their response functions for neutrons exhibit an enlarged (peaked) edge region (see Section 3.1.4) which arises from the enhanced probability for forward deuteron recoil from n-d elastic scattering events, the dominant detection mechanism in this scintillator.

---

† NE213 and NE230 were registered trademarks of Nuclear Enterprises Technology Inc. (Edinburgh, Scotland). These products are unfortunately no longer available. Bicron (Newbury, Ohio, USA) offer the equivalent products of BC-501A (NE213) and BC-537 (NE230) which are claimed to have the same chemical, physical and optical properties. The relative performance of NE213 and BC-501A is compared favourably in [Mo94].

The physical features of the different liquid scintillators employed in the present work are summarized in Table 3-3. Detectors A, B, and C were cylindrical glass cells (Nuclear Enterprises type VH1) made from Pyrex glass (~ 2 mm thick) and filled with NE213 (detectors A and C) and NE230 (detector B) liquid scintillator. To allow for the difference in the expansion of the scintillator and glass, there exists a small expansion chamber (~3.0 cm^3) joined to the main volume via a constricted neck. The size of the constriction and shape of the expansion chamber were designed so that the detector could be used in different orientations without the gas bubble in the expansion chamber passing into the main cell. The glass cells were externally painted with several coats of NE560 white reflector paint and light-tight aluminium covers were fitted around each scintillator. Detector M was a standard Nuclear Enterprises BA1-type cell of NE213 scintillator, encapsulated in an aluminium casing and internally coated with white diffuse NE561 reflector paint. The expansion chamber is a polyethylene tube which is wound around the circumference under the aluminium casing and the cell was sealed with a glass window on one face. Each scintillator was optically coupled to a 5.1 cm diameter 12-stage RCA-8850 photomultiplier tube using silicone jelly and mu-metal screens were used to shield all photomultipliers. The voltage divider circuit used was based on the standard network recommended [RCA] for these photomultipliers.

Table 3-3 *Physical characteristics of the scintillators used in present work.*

Detector name	***Scintil-lator type***	***NE type***	***Capsule***	***Outer diam. (cm)***	***Outer length (cm)***	***PM type***
A	NE213	VH1	glass	4.4	3.4	RCA-8850
B	NE230	VH1	glass	4.4	3.4	RCA-8850
C	NE213	VH1	glass	5.4	5.4	RCA-8850
M	NE213	BA1	aluminium	6.4	5.4	RCA-8850

3.1.2 Experimental arrangement

The experimental arrangement used for the Phase 1 scattering studies (see Table 3-1) is shown schematically in figure 3-1. The CN Van de Graaff accelerator at the NAC supplied a beam of 4.7 MeV deuterons which was pre-acceleration pulsed and bunched by a Klystron system [Kr72] into bursts with a time dispersion of less than 2.0 ns FWHM. The deuteron beam was directed through a 3 μm Havar window into a cylindrical stainless steel target cell

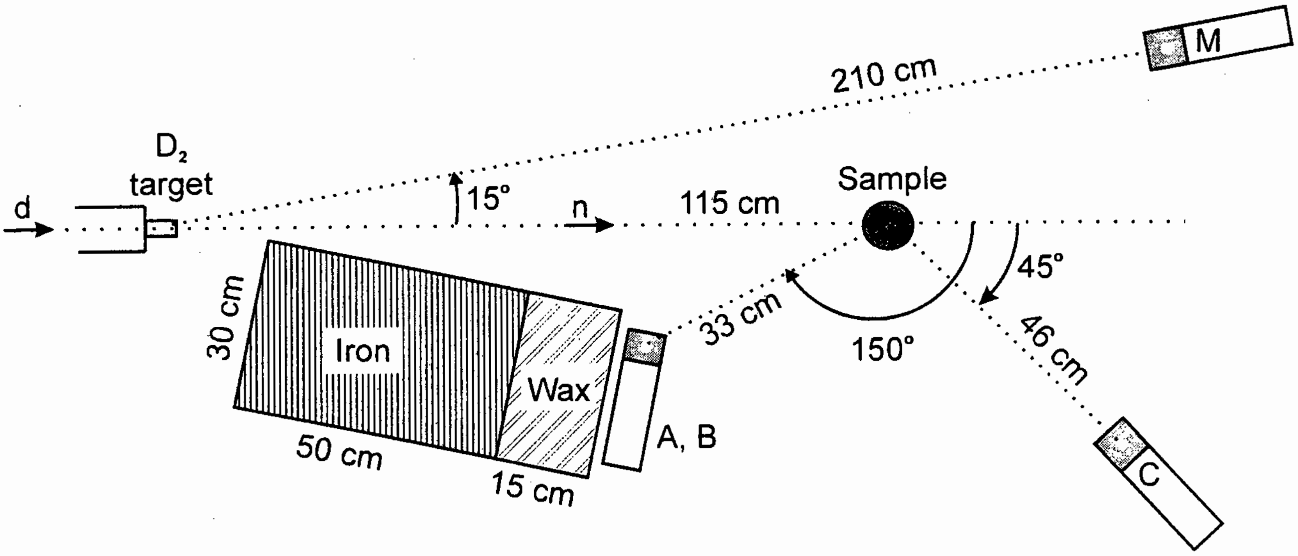

Figure 3-1 Schematic diagram of the experimental arrangement used for scattering measurements made using neutrons of incident energies 6.8 MeV and 7.5 MeV.

(12 mm ϕ × 30 mm), filled with deuterium gas at 1.0 atm pressure which produced pulsed 7.5 MeV neutrons via the $^{2}H(d,n)^{3}He$ reaction (Q-value of +3.269 MeV [Go72]). The average beam current at the target was 1.2 μA at a pulse repetition rate of 2.0 MHz. Beam deuterons passing through the gas were stopped by a 0.5 mm platinum disc. The target was mechanically wobbled to reduce heating effects, and was further cooled by a pressurized jet of air directed onto the front face of the cell. The neutron energy was calculated from the kinematics [Mi67] of the $^{2}H(d,n)^{3}He$ reaction at 0° to be 7.52 ± 0.07 MeV allowing for the energy loss [Ji84] of the deuterons in the 3 μm Havar window and deuterium gas. In addition to the incident neutron energy of 7.5 MeV, measurements were also made at an alternate energy of 6.8 MeV by dropping the deuteron beam energy to 4.0 MeV. Neutrons emitted at 0° relative to the deuteron beam were used for the scattering studies. In order to detect nearly backscattered neutrons, detector A (40 mm ϕ × 30 mm, NE213) and detector B (40 mm ϕ × 30 mm, NE230) were positioned at laboratory scattering angle 150° relative to the incident beam behind an iron and wax shadow shield. In later experiments (Section 3.3) detector C (50 mm ϕ × 50 mm, NE213) was also positioned at scattering angle 45°.

Absorption coefficients calculated for various materials are shown as a function of neutron energy in figure 3-2 [Ho67]. It can be seen from the figure that inelastic scattering from W, Cu and Fe is the most effective mechanism for slowing neutron of energies greater than about 5 MeV. Hydrogenous material is often used together with heavy shielding, since the total scattering cross section for $^1H(n,n)^1H$ increases smoothly with decreasing neutron energy (see figure 2-3). The shadow shield constructed for these experiments (figure 3-1) consisted of blocks of natural iron (30 cm × 30 cm × 50 cm) and borated paraffin wax (30 cm × 30 cm × 15 cm), mounted so as to shield detectors A, B and C from neutrons emanating directly from the deuterium target, and from secondary sources such as the deuteron beam collimators.

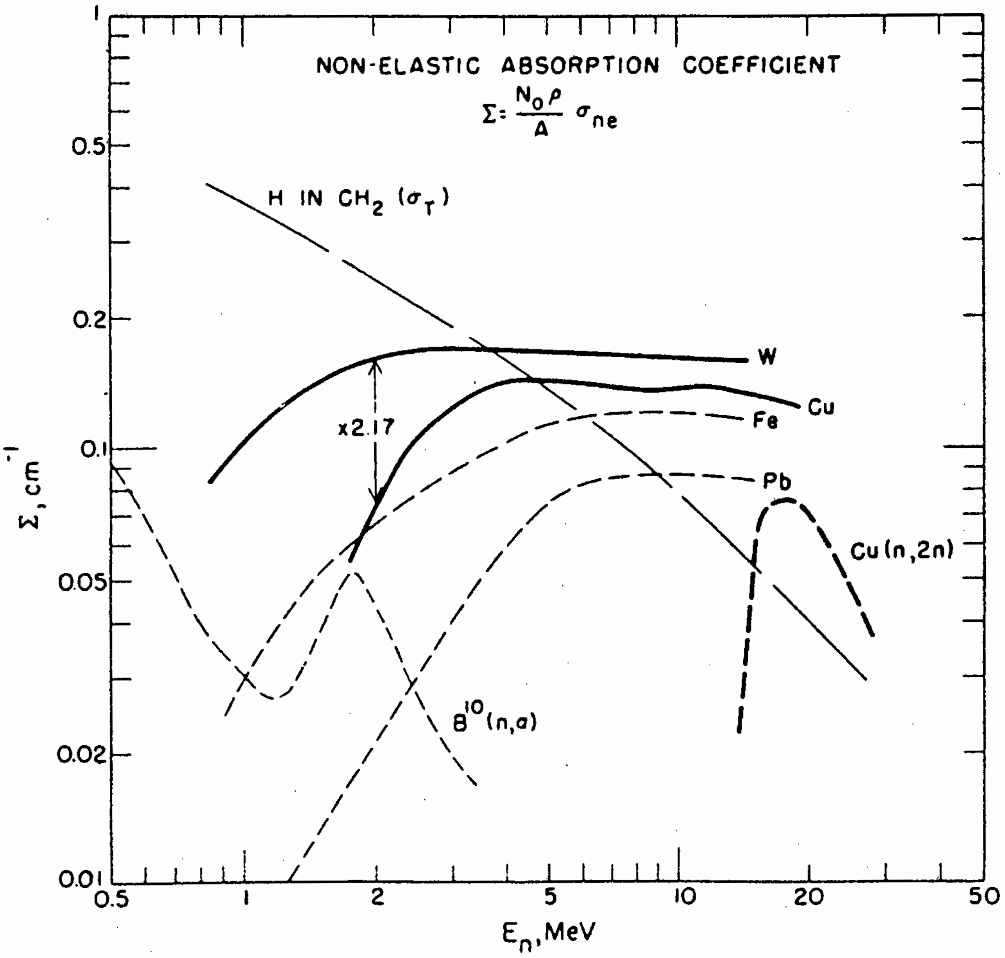

Figure 3-2 Absorption coefficients for neutron shielding by W, Cu, Fe, Pb and ^{10}B calculated [Ho67] using nonelastic cross sections, and for H in the density of polyethylene (CH_2), using the total cross section. The factor 2.17 is the ratio of tungsten to copper densities.

Most of the scattering samples used were powders or liquids of mass between 0.3 kg and 1.3 kg, which were encapsulated in thin, cylindrical aluminium containers (65 mm ϕ × 110 mm). The samples were suspended 115 cm from the target from a light aluminium frame, with their axes perpendicular to the incident beam direction. The set of samples used for the present studies is listed in Table 3-4. Measurements for nitrogen and oxygen were made using liquid nitrogen and liquid oxygen contained in a spherical Dewar flask of internal diameter 10 cm. Impurities in the samples listed in Table 3-4 were estimated to be less than 1% of the total mass. Care was taken to regularly recycle the liquid nitrogen and oxygen in the scattering Dewar and ice build-up on the Dewar was monitored and removed where necessary. The chemical compounds may be regarded as anhydrous, unless otherwise stated. Fresh supplies of these chemicals were used to fill the aluminium containers which were immediately sealed to prevent any contamination by water vapour.

Table 3-4 *Details of the scattering samples used in the present work.*

Sample	***Empirical formula***	***Mass (g)***	***Diameter (mm)***	***Length (mm)***
Graphite	C	365	52	100
Liquid nitrogen *	$N_2(l)$	400	100	
Liquid oxygen *	$O_2(l)$	570	100	
Water	H_2O	340	65	110
Aluminium	Al	1250	75	105
Silicon	Si	247	60	90
Sulphur	S	326	65	110
Iron	Fe	2400	50	149
Copper	Cu	1890	113	20
Lead	Pb	2890	50	125
Methanol	H_4CO	288	65	110
Ammonium nitrate	$H_4N_2O_3$	298	65	110
Acetamide	H_5C_2NO	212	65	110
Ammonium acetate	$H_7C_2NO_2$	272	65	110
Paraffin wax	C_2H_8	309	65	110
Aluminium oxide	Al_2O_3	618	65	110
Silicon nitride	Si_3N_4	189	65	110
Carbon tetrachloride	CCl_4	568	65	110
Lithium chloride	LiCl	405	65	110
Copper sulphate	$CuSO_4(xH_20)$	460	65	110
Iron sulphate	$Fe_2(SO_4)_3(xH_20)$	284	65	110
Empty container		41	65	110
* Empty Dewar		185	100	

Background measurements were made for each of the following conditions: using an empty aluminium container; using the empty Dewar; and with no sample in position. The shadow shield, detectors and scattering samples were mounted in a plane at 2.7 m above the floor and about 6 m from the nearest wall, following the standard practice at the NAC VDG to minimize the diffuse background arising from neutrons scattered from the concrete walls and floor of the experiment vault. A fourth NE213 scintillator (detector M), placed about 2.1 m from the target at 15° to the incident beam, was used to monitor the neutron output from the target. The counts from this detector selected by a time-of-flight window were proportional to the number of neutrons produced in the target. Since the acceptance angle of the scattering samples remained the same throughout the experiments, the counts measured by detector M were therefore also proportional to the number of neutrons impinging on the scattering sample.

3.1.3 Data acquisition system

Figure 3-3 shows a detailed schematic diagram of the data acquisition system, the main features of which are summarized in figure 3-4. Signals were produced from three sources, namely the primary neutron detectors (A, B and C), the beam monitor (M) and a beam reference signal from the Van de Graaff. The fast outputs from the anodes of the photomultipliers of detectors A, B and C were coupled together and fed directly into a modified [Sm86] Link Systems Model 5010 Pulse Shape Discriminator (LINK) [Ad78] which provided two outputs, L and F [Sm86, Sm87]. The pulse height L was generated by integrating the scintillation pulse over a period of 500 ns while the F pulse was obtained by integrating over 30 ns [Sm87]. A scintillation pulse shape parameter S was later derived off-line for each event from the L and the F parameters by combining them in the form

$$S = L - kF + C$$

where k and C are constants as described earlier in Section 2.3.1. The LINK also provided a timing output which was used to start the time-to-amplitude converter (TAC) which measured the scattered neutron time-of-flight T_n. The signals from the 4th dynodes of the photomultipliers of detectors A, B and C were each directed through a pre-amplifier and amplifier chain for an independent pulse height measurement (parameter D). The L-threshold was set on the LINK and the D-thresholds for each detector were adjusted using timing single channel analyzers (TSCA). With the LINK thresholds set at a pulse height corresponding to 0.1 MeV electron energy, the LINKs were typically processing events at approximately 3 kHz. Signals from the dynode outputs of each photomultiplier were also used to generate logic pulses which were recorded via a pattern register R to facilitate off-line separation of the events recorded by each detector.

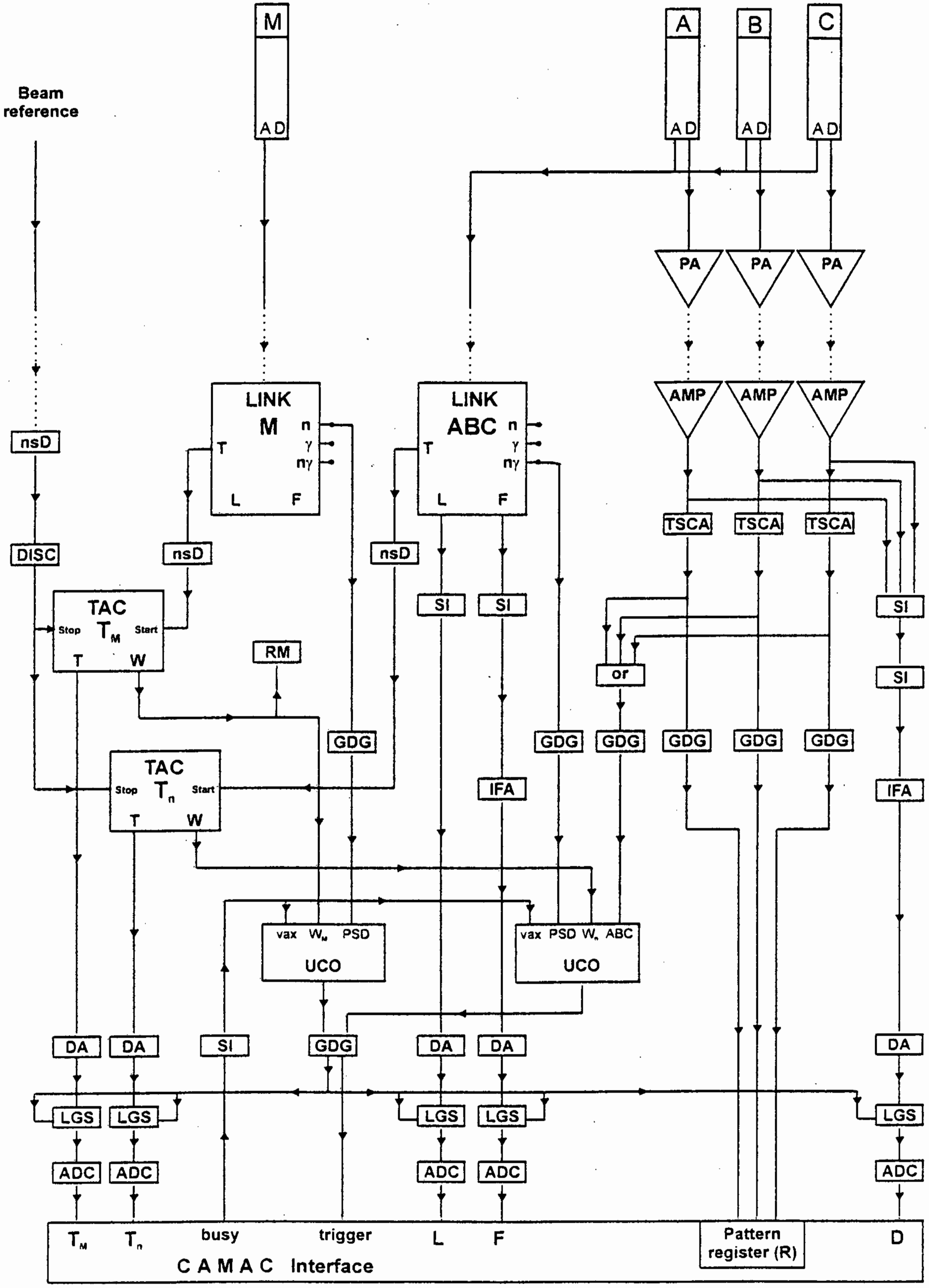

Figure 3-3 Schematic diagram showing the details of acquisition electronics (see text). The outputs from the ADC's were routed via a CAMAC interface through a Micro-programmable Branch Driver (MBD-11) to a VAX 11/730 acquisition computer running XSYS software.

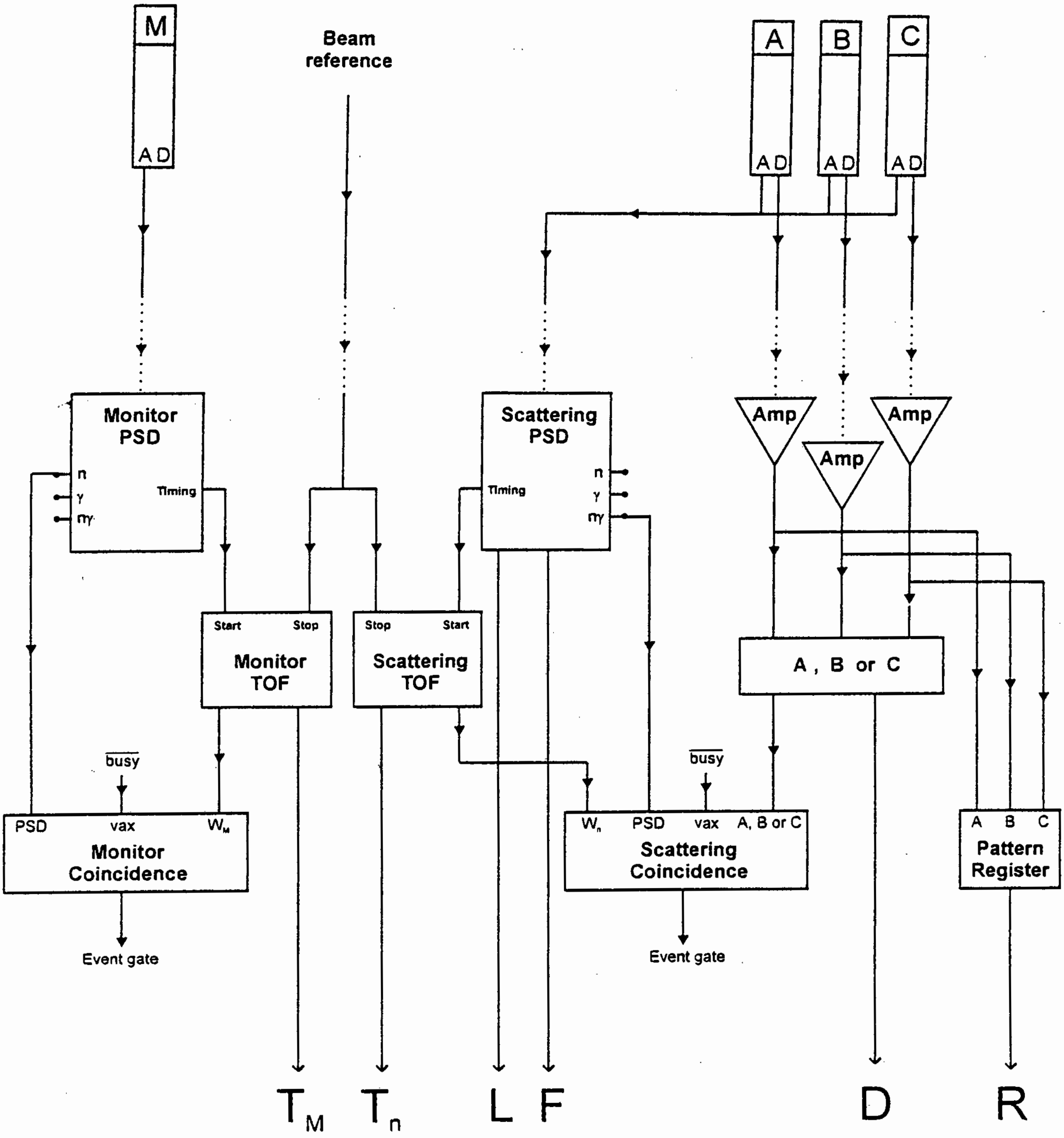

Figure 3-4 Schematic diagram of the main features of the acquisition system. Six parameters were buffered for each accepted event.

The signals from the anode of the monitor detector M were fed directly into a separate LINK which selected those events identified as resulting from the detection of neutrons. This LINK also provided a timing output which was used to start the TAC that measured the time-of-flight T_M of the neutrons detected by the monitor detector. The stop pulses for both the T_n and T_M TACs were derived from an inductive pick-up coil installed on the deuteron beam-line near to the target cell. Standard nanosecond delays were used to calibrate each TAC.

Two universal coincidence (UCO) units were used to gate the experiments, one for the scattering events (recorded by detectors A, B or C) and one for the monitor events (detector M). For the scattering events, logic pulses from the LINK, the T_n TAC and the dynode of detector A, B or C were required in coincidence. For the monitor events, logic pulses from the monitor LINK (for events identified as neutrons) and from the T_M TAC (for events within the time-of-flight window) were required simultaneously. The outputs from the UCOs were used to gate the linear gate and stretcher (LGS) units allowing the data to be passed to the ADCs for analogue to digital conversion, and also to trigger the acquisition computer. A busy logic level was produced when required by the acquisition computer which was included as an anti-coincidence requirement in both UCOs.

All phases of the data acquisition were monitored on a system of displays and scalers to detect any electronic drifts. After electronic signal processing, the data signals were fed via CAMAC through a Micro-programmable Branch Driver (MBD-11) to a VAX 11/730 acquisition computer running the XSYS data acquisition software under the VMS operating system. Event by event data were recorded in memory and buffered to disk in 4k blocks. The six parameters recorded for each event are summarized in Table 3-5. Data reduction was completed off-line using custom-written FORTRAN analysis programs.

Table 3-5 Parameters recorded for each buffered event.

Parameter	***Description***
L	Pulse height (long time integral) from LINK serving detectors A, B and C.
F	Fast integral of anode pulse processed by LINK.
D	Pulse height derived from 4th dynode of each photomultiplier (A, B or C).
T_n	Neutron time-of-flight for detectors A, B or C.
T_M	Neutron time-of-flight for beam monitor detector (M).
R	Pattern register used to separate events from each detector.

3.1.4 Detector calibrations

Various calibrations were performed using the neutron beam as well as with an ^{241}Am/^{9}Be (AmBe) source. These included time and pulse height calibrations as well as measurements of the response functions [†] of each detector for known sources of monoenergetic neutrons and γ-rays in order to inspect their overall performance and energy resolution.

AmBe sources provide a neutron spectrum predominantly below 10 MeV as well as a photon of 4.44 MeV from the decay of the corresponding ^{12}C state populated in the ^{9}Be(α,n)^{12}C reaction. An AmBe source was used to adjust the detector thresholds and gains, as well as the PSD settings on the LINK modules, including measurements [Ol92] of the true zero of the LINK pulse height parameter (L). The response function of an organic scintillator depends on the type and energy spectrum of the incident radiation [Bu90] as well as the size, shape and geometry of the detector. Figure 3-5 shows pulse height spectra measured for the 4.44 MeV γ-ray from an AmBe source (selected by pulse shape discrimination), using (a) detector A (NE213) and (b) detector B (NE230). The principle features of these response functions, labeled in figure 3-5(a), are the Compton edge (at 4.20 MeV) and 3.42 MeV double escape peak which arises from the pair interaction of the 4.44 MeV γ-ray on the carbon component of the organic scintillator. This peak provides an unambiguous calibration reference for small scintillators such as detectors A and B, as its mean value is insensitive to both multiple scattering and the detector pulse height resolution. The mean free path of 0.511 MeV photons is approximately 9 cm in liquid scintillator, thus the photons created in positron annihilation events are highly likely to escape from the volume of these detectors. If the 0.511 MeV photon does interact, the probability that it deposits all its energy is very low, and therefore a single escape peak does not appear. The energy of the Compton edge E_C of the 4.44 MeV γ-ray was calculated to be 4.20 MeV using [Kn89]

$$E_C = \frac{2E_\gamma^2}{2E_\gamma + m_e c^2} \tag{3.1}$$

where $m_e c^2$ is the electron rest mass energy (0.511 MeV). The features in the response functions are affected by the geometrical dimensions of the sensitive volume of the detector. It is also possible that the electron, after having escaped from the scintillator volume, may be scattered

---

[†] A <u>response function</u> of a liquid scintillator is regarded here as a pulse height spectrum measured for a known radiation field. The <u>lineshape</u> of the detector is the response function measured for mono-energetic radiation of a single type. A <u>response matrix</u> is a set of lineshapes measured for a range of incident energies.

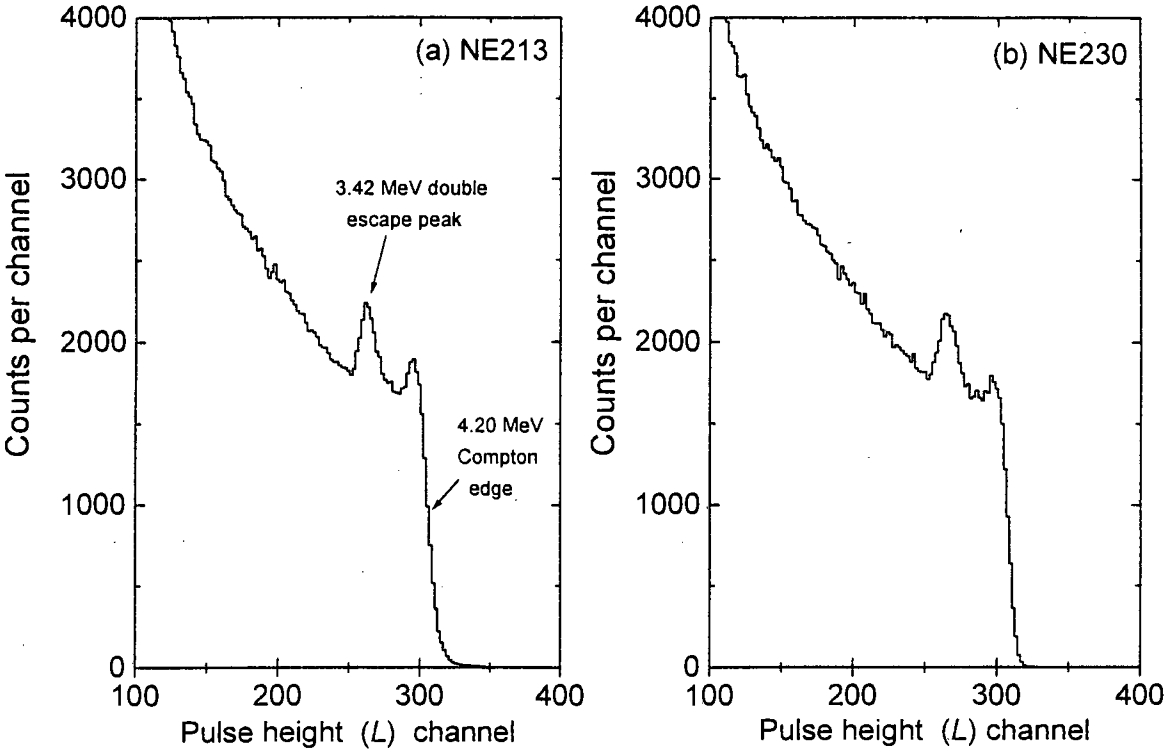

Figure 3-5 Pulse height response of (a) an NE213 liquid scintillator (40 mm ϕ × 30 mm) and (b) an NE230 liquid scintillator (40 mm ϕ × 30 mm) to 4.43 MeV photons from an AmBe source. Events associated with the detection of γ-rays in the detectors are separated from neutron events by pulse shape discrimination. The significant features are the 4.20 MeV Compton edge and the 3.42 MeV double escape peak.

back into the detector by the surrounding material, which will further affect the shape of the response function. These effects have been recently studied [No97] together with the contribution to the response function resulting from photons produced via neutron interactions in the metal casings of liquid scintillators.

Figure 3-6 shows an orthographic plot of events as a function of pulse height parameter L and pulse shape parameter S, measured by detector B (NE230) placed 1.20 m directly in front of the deuterium gas target bombarded by 4.7 MeV deuterons. Events associated with the detection of recoiling deuterons and electrons in detector B, as identified by the LINK through pulse shape discrimination, form two well-defined loci on the L-S plane. These neutron and γ-ray induced events are easily separated from each other by software windows as illustrated by

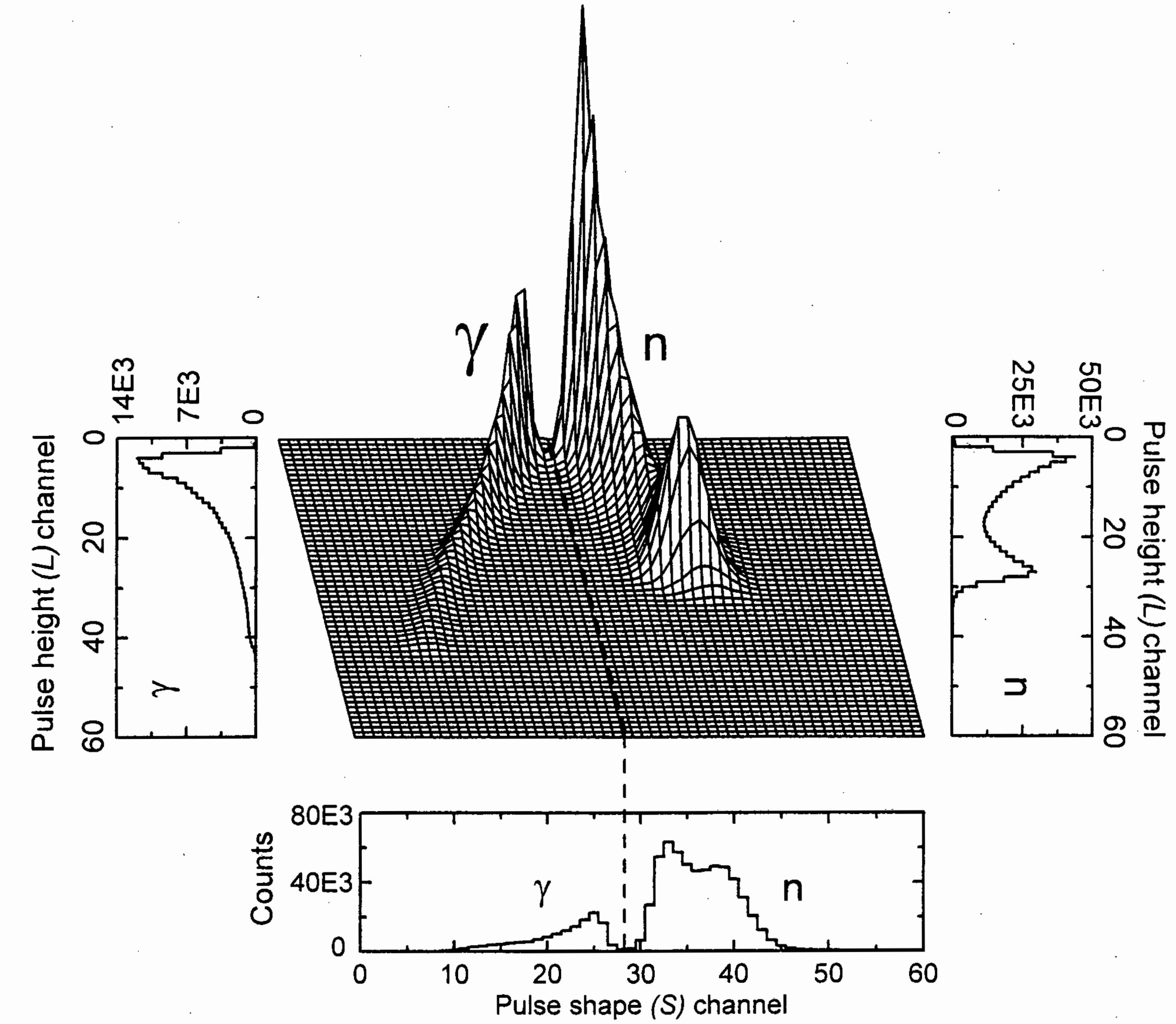

Figure 3-6 *Counts (vertical) as a function of pulse height parameter (L) and pulse shape parameter (S) for events in an NE230 liquid scintillator (40 mm φ × 30 mm) mounted at 1.20 m directly in front of a deuterium gas target (12 mm φ × 30 mm, 1.0 atm) which was bombarded by deuterons of energy 4.7 MeV. Loci associated with the detection of deuterons and electrons, recoiling from neutron- and γ-ray-induced interactions, respectively, in the scintillator are indicated. These loci are well separated on the L-S plane by pulse shape discrimination, illustrated by the projection of all the events onto the S-axis. The dotted line shows a cut used to select either neutron or gamma events which are shown as projections onto the L-axis.*

the two projections onto the *L*-axis. Also shown in figure 3-6 is the projection of all the events onto the *S*-axis, illustrating the excellent separation of the loci arising from the detection of neutrons and γ-rays in the scintillator, for the pulse height (L) threshold of 0.5 MeV (electron equivalent energy), which corresponds to a recoil deuteron energy of 2.2 MeV.

Figure 3-7 shows lineshapes measured at 0° using detectors A (NE213) and B (NE230) mounted at 1.20 m directly in front of the deuterium gas target which was bombarded by deuterons of energies 4.0 MeV and 4.7 MeV, respectively. The lineshapes in figure 3-7 are associated with the detection of neutrons of energies 6.8 MeV ((a) and (b)), and 7.5 MeV ((c) and (d)), selected by pulse shape discrimination (see figure 3-6), and show features expected [Bu97] for the respective detectors, notably the approximately flat pulse height distributions for detector A and the peaked distributions for detector B. The maxima in the lineshapes measured for detector B (figures 3-7(b) and (d)) arise from the enhanced probability for forward deuteron recoil from n-d elastic scattering events, the dominant detection mechanism in this scintillator at these energies. The half-heights of the upper limits (edges) of the pulse height spectra (broadened by the detector resolution), which correspond to forward recoil of protons in detector A, or deuterons in detector B, increase with neutron energy, as expected. The slight enhancements visible just below the upper pulse height edges are attributed to the effects of multiple neutron scattering within the scintillators.

The sharpness of the respective pulse height edges provide a measure of the energy resolution of the detectors for neutrons of that particular energy. These edges are broadened by photomultiplier statistics, the physical characteristics of the scintillator and by any non-uniformity in the efficiency for the transmission of scintillation light from different regions of the scintillator to the cathode of the photomultiplier. A quantitative measure of the energy resolution was obtained by differentiating the spectra $N(L)$ shown in figures 3-7(a)-(d) and plotting $-\mathrm{d}N(L)/\mathrm{d}L$ versus L (figures 3-7(e)-(h)). The edge resolution width, defined as the FWHM of the corresponding peaks, was determined to be about 5% for both detectors at these energies.

3.1.5 Estimates of data rates

The expected experimental count rates for the scattering studies were estimated. Consider the experimental arrangement described in Section 3.1.2 for the case of a uniform beam of monoenergetic neutrons irradiating solid mono-elemental cylindrical samples (65 mm ϕ × 110 mm), comprised solely of the nuclides ^{12}C, ^{14}N or ^{16}O, positioned vertically in the beam as indicated in figure 3-8. The counting rate $Y_j(\theta\ , E_n\,, E_o)$ in detector B due to neutrons which have been elastically scattered once and only once in the sample is given by [Ki70]

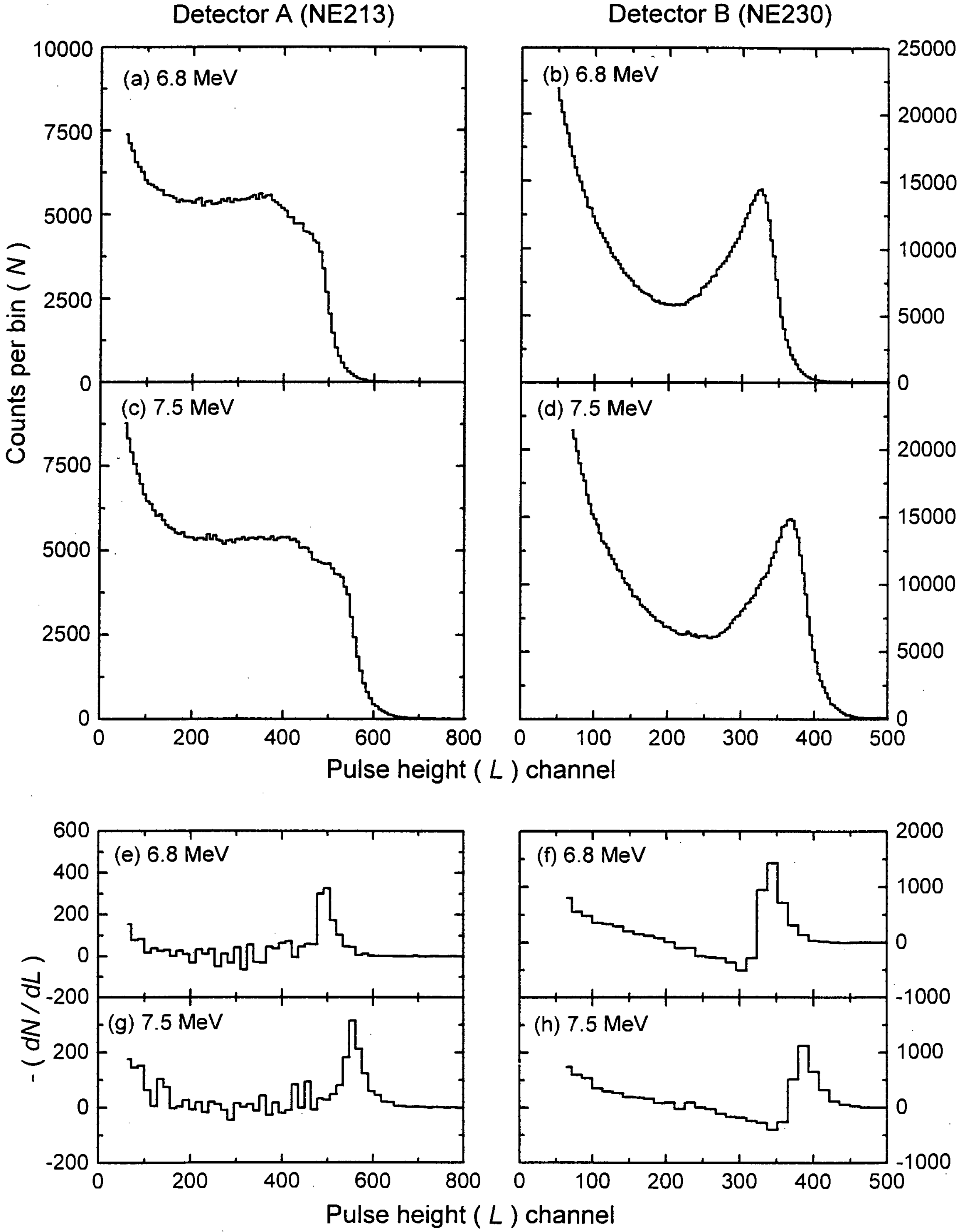

Figure 3-7 Lineshapes N(L) versus L measured by NE213 detector A (40 mm ϕ × 30 mm) and NE230 detector B (40 mm ϕ × 30 mm), for neutrons of energy 6.8 MeV and 7.5 MeV, as indicated. Events associated with the detection of neutrons in the detectors are separated from γ-ray events by pulse shape discrimination. Panels (e) to (h) show the corresponding differentiated lineshapes −dN(L) / dL versus L.

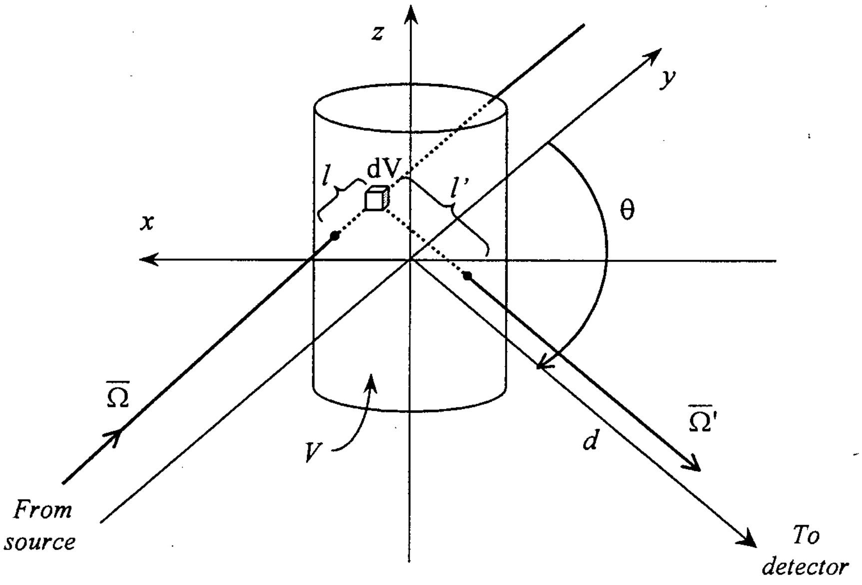

Figure 3-8 Neutron scattering from a cylindrical sample into a detector mounted at laboratory angle θ.

$$Y_j(\theta,E_n,E_o) = \frac{N_o\, n_j\, A\; \varepsilon(E_n)}{d^2}\int_V \exp\{-\Sigma_T(E_o)l - \Sigma_T(E_n)l'\}\;\sigma_j(\overline{\Omega}\cdot\overline{\Omega}',E_o)\,dV/r^2 \tag{3.2}$$

where:

E_o : Incident neutron energy

E_n : Scattered neutron energy

N_o : Number of neutrons irradiating the sample per unit time

n_j : Average nuclear areal density of the scattering sample comprised of nuclide j

$\varepsilon(E_n)$: Neutron detection efficiency of detector B for neutrons of energy E_n

d : Distance from the axis of the scattering sample to detector B

A : Area of detector B normal to the scattered neutron direction

θ : Laboratory angle of scattered neutron

$\overline{\Omega}$: Direction from the source to the collision point

$\overline{\Omega}'$: Direction from the collision point to the detector

$\sigma_j(\overline{\Omega}\cdot\overline{\Omega}',E_o)$: Differential cross section for neutron elastic scattering from nuclide j

$\Sigma_T(E_o)$: Total probability per unit path length for the incident neutron to interact in the sample before scattering

$\Sigma_T(E_n)$: Total probability per unit path length for the scattered neutron to interact in the sample before reaching detector B

l : Distance travelled in the sample by the incident neutron before scattering
l' : Distance travelled in the sample by the scattered neutron.
r : Distance from the source to the collision point
V : Sample volume

Corrections for the neutron source angular and intensity distribution may also be included [Ve75] in equation 3.2. Furthermore, it is assumed that the detector is sufficiently far from the sample such that the distance from the collision point to the detector may be considered to be constant and equal to d, with negligible error. Neutrons which have been scattered more than once in the sample contribute an additional counting rate to detector B. Multiple neutron scattering is complicated to model analytically [En71] since it is a non-linear function of local densities. However, the number of these events is expected to be small in comparison with single scattered events (see Section 3.3.1). It is also assumed that all neutrons scattered into detector B originate from the scattering sample, i.e. the detector is well shielded so that there is no background arising from neutrons scattered from outside the sample. In practice such a background is measured and subtracted, so should pose no complication to any analyses.

If the attenuation of incident and scattered beams are also regarded to be negligible, and the height h of the sample in the beam is much less than r, then equation 3.2 reduces to

$$Y_j(\theta, E_n, E_o) = N_o \, n_j \, \varepsilon(E_n) \, \sigma_j(\theta, E_o) \, \Omega \qquad (3.3)$$

where [Kn89]

$$\Omega = 2\pi\left(1 - \frac{d}{\sqrt{d^2 + a^2}}\right) \qquad (3.4)$$

and a is the radius of the detector.

Since $r \gg h$, the number of incident neutrons per second N_o incident on the sample is approximated [Ve75] by

$$N_o = S \, I \, \Delta E \, \Omega_s \qquad (3.5)$$

where S is the specific neutron yield for the ^{2}H(d,n)^{3}He reaction at 0° (see figure 3-9), I is the current of the deuteron beam (1.0 μA), ΔE is the calculated [Ji84] energy loss of the deuteron beam in the target, and Ω_s is the solid angle subtended by the sample at the target, given similarly by equation 3.4. Table 3-6 lists total elastic scattering yields $Y_j(\theta, E_n, E_o)$, calculated at

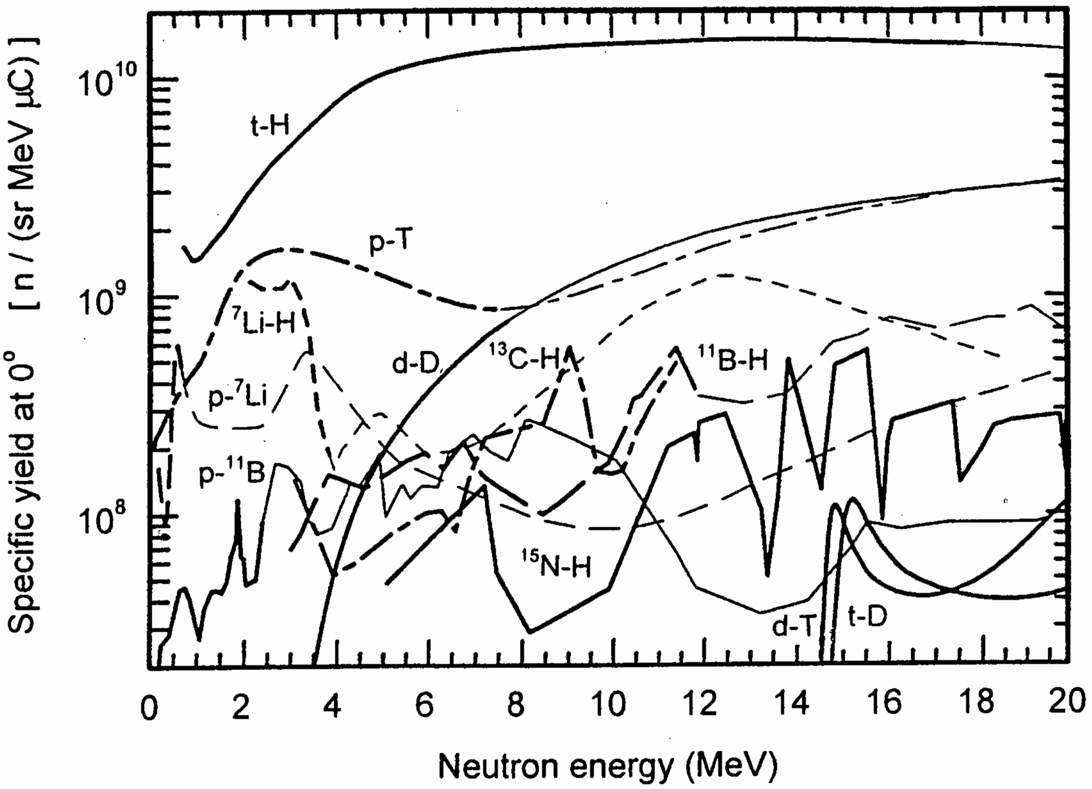

Figure 3-9 Energy dependence of the specific neutron yield calculated at 0° for monoenergetic neutron production up to 20 MeV [Dr94]. The thick portions of the curves indicate the truly monoenergetic energy ranges.

$\theta = 150°$ using equations 3.3 to 3.5, for a range of incident neutron energies E_o . The rates have been calculated for scattering samples comprised only of the nuclides ^{12}C, ^{14}N and ^{16}O, each having $3N_A$ scattering nuclides cm^{-2} where N_A is Avogadro's number. The differential scattering cross sections used in conjunction with equation 3.3 were those shown in figure 2-9 and the efficiency $\varepsilon(E_n)$ of the detector was taken from [Ve68].

Based on these calculations, it was decided that each scattering run should be completed over 120 minutes of running, representing about 7.2 mC of integrated beam current on target. This would yield approximately (0.7 - 5.0) × 10^6 detected neutrons at E_o = 7.5 MeV, depending of the species of scattering nuclide. At first impression, these data rates could seem prohibitively slow for a practical system, especially if a number of voxels of an extended sample need to be analyzed. However a number of improvements could be made would increase these data rates to well within the range which would be acceptable in a practical situation, such as an airport (see Chapter 7). For example, the present beam current of 1.0 μA could be increased to 20 μA, or more. Furthermore the solid angle subtended by detector B at 150° could be maximized in a practical FNSA system to a ring of liquid scintillator (see figure 7-4), obtained by rotating detector B around the neutron beam axis. This would improve the overall detection efficiency by more than a factor of 30. These improvements would reduce the detection time by an approximate factor of 600, i.e. 5.0×10^6 neutrons would be detected in less than 12 seconds. Of course, it is assumed here than the data acquisition system could handle such a rate approaching 1 MHz without significant dead time. This is not envisaged to be a difficulty since multiple LINKs and TACs could be used without complication and modern logic units which can handle trigger rates of over 2 MHz have already been reported [Ch95].

Table 3-6 *Estimates of scattering data rates $Y_j(\theta, E_n, E_o)$* #.

E_o (MeV)	N_o ($n\ s^{-1}$)	Scattering nuclide	$\sigma(150°)$ ($b\ sr^{-1}$)	E_n (MeV)	$\varepsilon(E_n)$	$Y_j(\theta, E_n, E_o)$ ($n\ s^{-1}$)
5.00	0.4×10^5	^{12}C	0.25	3.65	0.25	88
6.80	1.1×10^5	^{12}C	0.20	4.96	0.23	201
7.50	1.3×10^5	^{12}C	0.60	5.47	0.22	673
10.00	2.5×10^5	^{12}C	0.15	7.29	0.19	274
5.00	0.4×10^5	^{14}N	0.60	3.82	0.24	202
6.80	1.1×10^5	^{14}N	0.28	5.19	0.22	269
7.50	1.3×10^5	^{14}N	0.35	5.72	0.21	375
10.00	2.5×10^5	^{14}N	0.30	7.63	0.17	490
5.00	0.4×10^5	^{16}O	0.55	3.95	0.23	178
6.80	1.1×10^5	^{16}O	0.30	5..37	0.21	275
7.50	1.3×10^5	^{16}O	0.10	5.95	0.20	102
10.00	2.5×10^5	^{16}O	0.25	7.90	0.15	360

 # The calculations assume an 1.0 μA beam of deuterons incident on a 3.0 cm long deuterium gas cell (1.0 atm) producing a flux of N_o neutrons at 0° [Dr94] incident on scattering samples of ^{12}C, ^{14}N and ^{16}O, each having $3N_A$ nuclides cm^{-2}. The neutrons elastically scattered with energy E_n from the samples are detected by a single liquid scintillator (40 mm $\phi \times 30$ mm) mounted at $\theta = 150°$. The differential cross sections $\sigma(150°)$ are from [Ro91] and the detector efficiencies $\varepsilon(E_n)$ estimated from [Ve68].

3.2 Element analysis by neutron backscattering

3.2.1 Elastic scattering

In Section 2.1.1, it was suggested that if the energy of elastically backscattered (> 150°) neutrons can be measured sufficiently accurately then the kinematics of this process provides a basis for determining the mass and hence type of the scattering nuclide. In neutron elastic backscattering, as in Rutherford backscattering analysis, the energy loss diminishes steadily with increasing scatterer mass number A. Figure 3-10 shows the energy of elastically scattered neutrons as a function of mass number, calculated using equations 2.1 and 2.2 at $\theta = 45°$ and 150°, for the incident neutron energies of 6.8 MeV and 7.5 MeV. The mass numbers of the nuclides ^{12}C, ^{14}N, ^{16}O, ^{27}Al and ^{56}Fe are marked with dashed lines. It is seen from figure 3-10 that the energies of the neutrons backscattered by ^{12}C, ^{14}N and ^{16}O are separated from each other by approximately 4%, which is sufficiently different for pulse height measurements made by organic scintillators to discriminate between these nuclides.

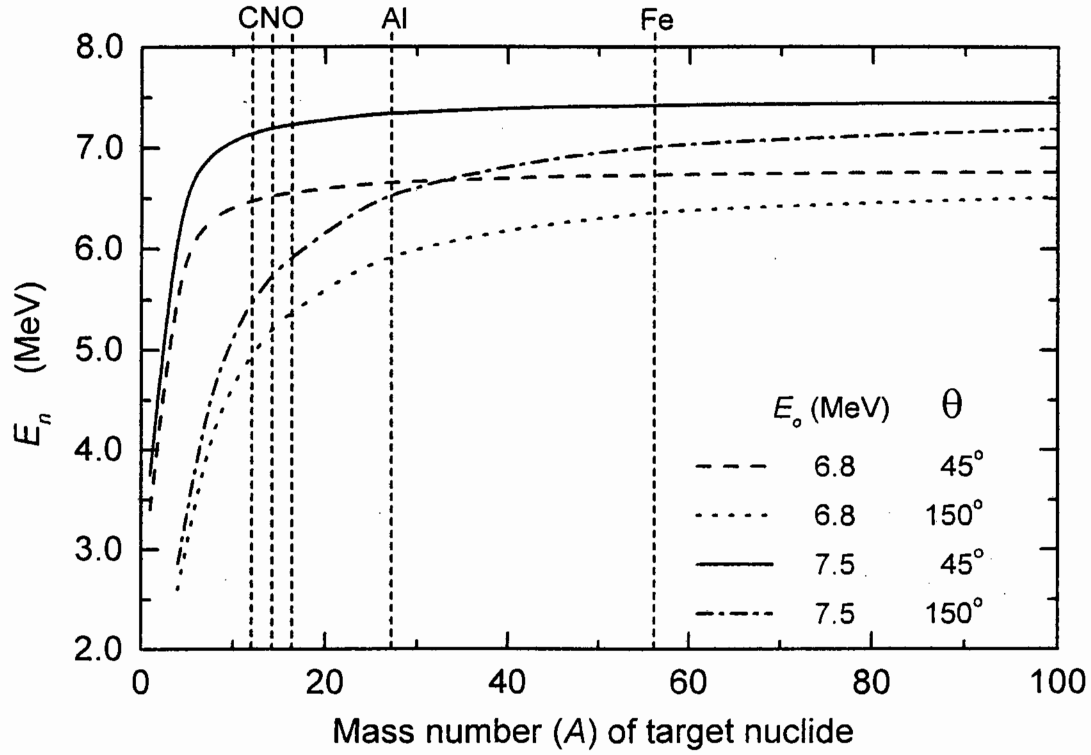

Figure 3-10 Energy of the scattered neutron (E_n) as a function of mass number (A) of the target nuclide calculated at laboratory angles (θ) of 45° and 150° for the incident neutron energies (E_o) of 6.8 MeV and 7.5 MeV. The dotted lines indicate the mass numbers of the nuclides ^{12}C, ^{14}N, ^{16}O, ^{27}Al and ^{56}Fe.

Figure 3-11 shows counts as a function of neutron time-of-flight parameter (T_n) measured by detector B (at 150°) for neutrons of energy 7.5 MeV scattered from the samples of (a) graphite, (b) liquid nitrogen and (c) water. Dotted lines in each figure illustrate background spectra measured for no sample (for the graphite), the empty Dewar (for the liquid nitrogen) and an empty aluminium container (for the water). For events within the time window W_T shown in figure 3-11(a), scattering response functions (pulse height spectra) were obtained (figure 3-12) for the three scatterers of graphite, nitrogen and water, after subtracting the appropriate background distribution from the spectrum measured with the scatterer in place. The fraction of background in the sample-in measurement varied between 5% and 20%. To facilitate

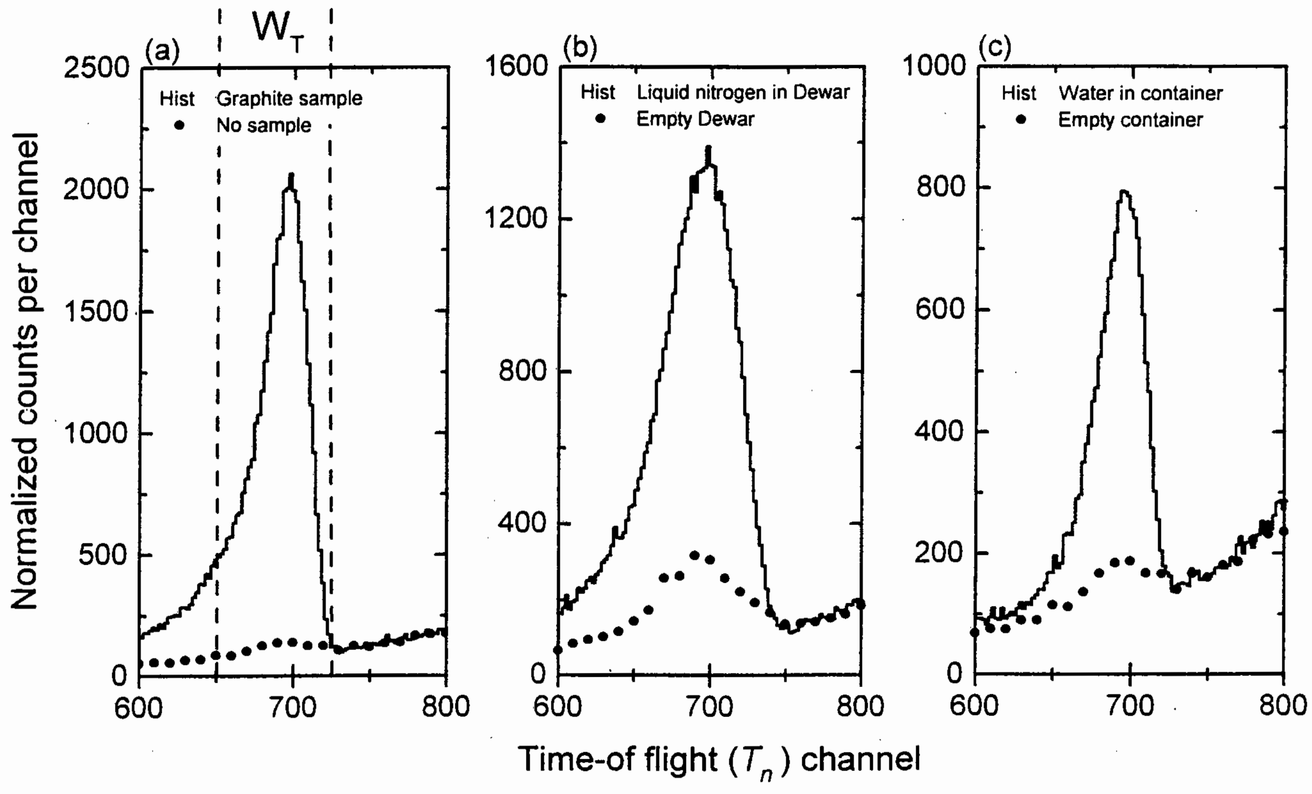

Figure 3-11 Counts as a function of time-of-flight parameter (T_n) measured by detector B (NE230, 40 mm $\phi \times 30$ mm) at 150° (see figure 3-1) for scatterers (histograms) of (a) graphite, (b) liquid nitrogen, and (c) water. Also shown are background spectra (dots) measured for: (a) no scatterer present; (b) the empty Dewar; and (c) an empty sample container. Each background spectrum has been normalized to the appropriate sample-in spectrum using the counts measured by the monitor detector (M). Also shown is the window (W_T) used to select events within the elastic scattering peak.

comparison of the edge position, the three spectra in figure 3-11 have been normalized to the same maximum number of counts. The pulse height distributions are similar to the lineshape measured at 0° for the NE230 detector (figure 3-7), indicating that they are mainly due to the detection of deuterons recoiling forward from n-d elastic scattering events in the scintillator. The forward recoil pulse height edges (upper limits) are seen to increase, as expected, from $L = 242$ (C) to $L = 255$ (N) to $L = 263$ (O), due to the increase in backscattered neutron energy with increasing mass number of the scatterer. The pulse height edges in figure 3-12 correspond to the forward deuteron recoils caused by neutrons of energy 5.46 MeV, 5.72 MeV and 5.92 MeV scattered from the nuclides ^{12}C, ^{14}N and ^{16}O, respectively.

Neutron spectrometers based on recoil detection in organic scintillators appear to be able to identify neighbouring light elements such as C, N, O by means of neutron elastic backscattering. However, as can be seen from figure 3-10, the energy variations between neutrons elastically backscattered from nuclides of mass number $A > 25$ are very small (< 2%). Therefore, unlike the case for the light nuclides, pulse height measurements using organic scintillators will not be able to distinguish between the neutrons elastically backscattered from heavier nuclides (A > 25). Nevertheless, such pulse height spectra may also include lower energy contributions from inelastically scattered neutrons, these energies being determined by

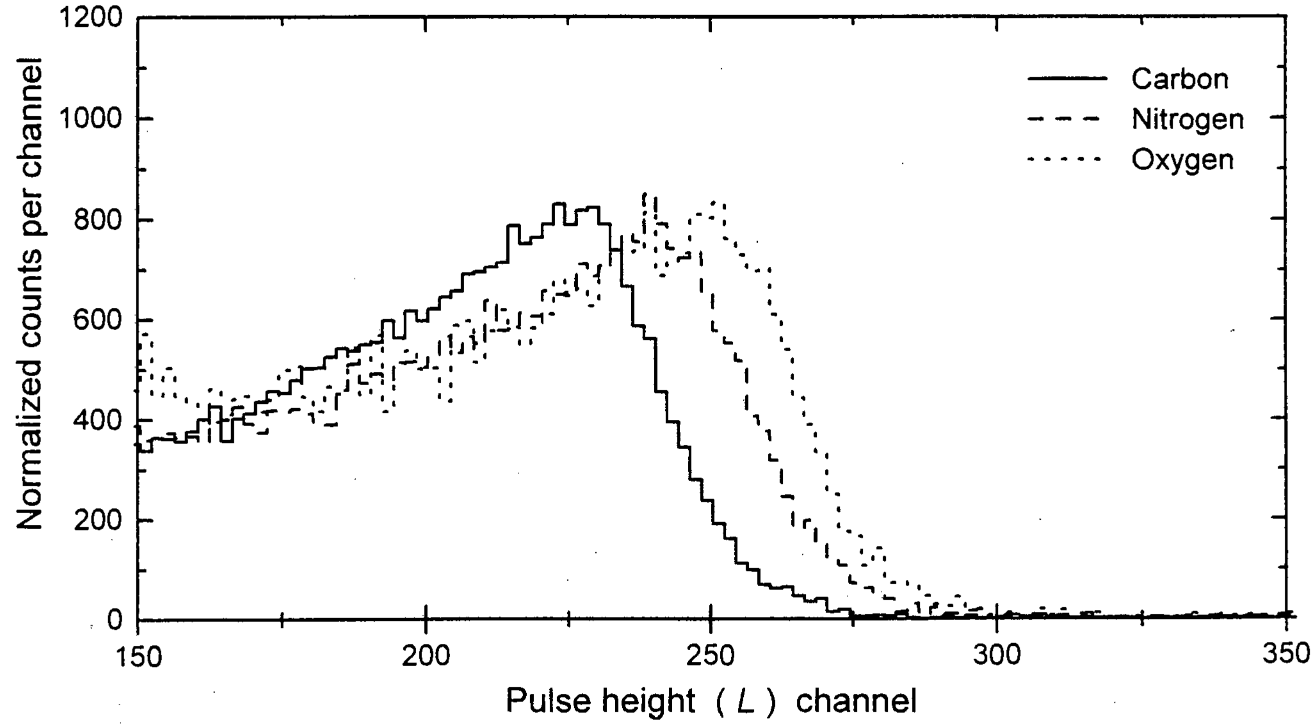

Figure 3-12 Response functions measured by detector B (NE230, 40 mm ϕ × 30 mm) at 150° for 7.5 MeV neutrons incident on scattering samples of graphite, liquid nitrogen and water. The data have been selected by the window W_T shown in figure 3-11 and normalized to the same maximum yield value.

the level structure of the target nucleus [Le78] and the incident neutron energy. These additional inelastic features could facilitate the identification of medium and heavy elements, as well as enhancing the identification of light elements.

3.2.2 Inelastic scattering

Figure 3-13(a) shows response functions measured by detector B at 150° for 7.5 MeV neutrons scattered from samples of aluminium and silicon. The spectra in figure 3.13(a) have been normalized to the same yield (approximately) for elastic scattering by adjusting each spectrum to the same number of counts at channel $L = 300$. The positions of the upper pulse height edges of the elastic components for the nuclides ^{27}Al and ^{28}Si are indistinguishable. However these response functions display distinctive structure at lower pulse height ($L < 225$), which is associated with inelastic neutron scattering. This makes it possible to distinguish these two elements despite the similarity of the elastic scattering components in their response functions. Figure 3-13(b) shows response functions measured under the same conditions for scattering samples of iron ($A = 26$) and lead ($A = 82$), each normalized to the same total scattering yield. The response functions for these two elements are also quite distinctive due to their different elastic and inelastic components.

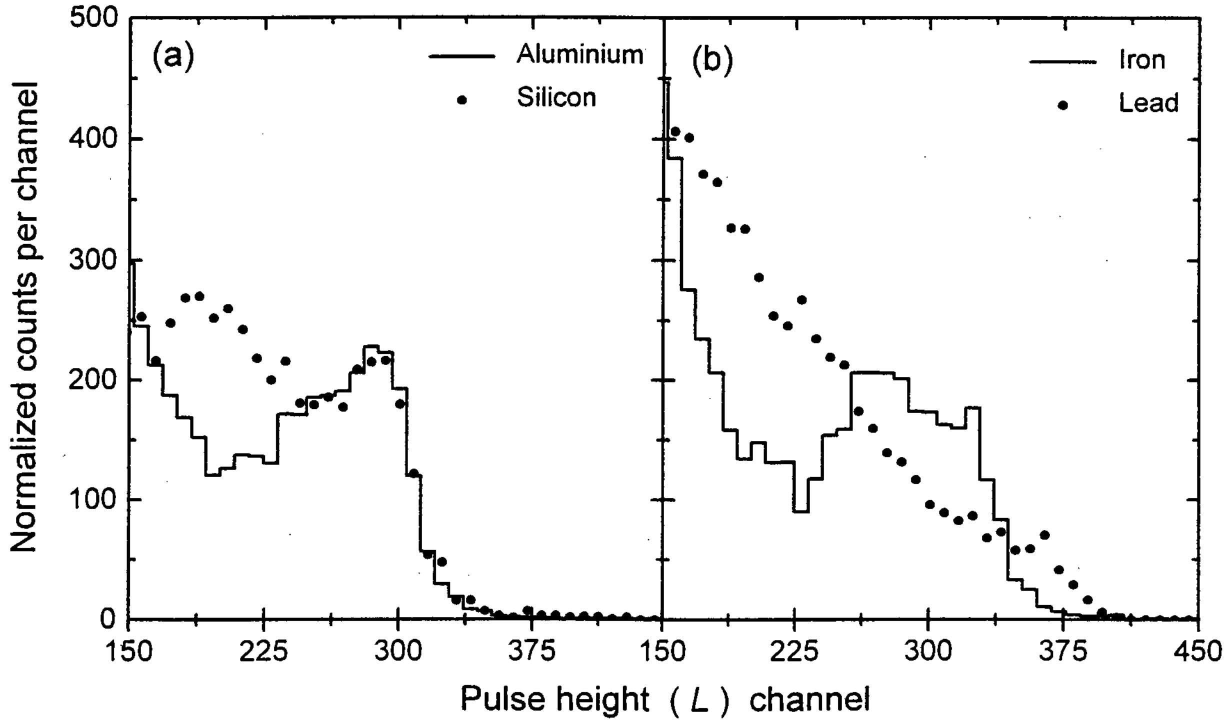

Figure 3-13 Response functions measured by detector B (NE230, 40 mm $\phi \times 30$ mm) at 150° for 7.5 MeV neutrons incident on scatterers of (a) aluminium and silicon , and (b) iron and lead. The data have been selected by the window W_T shown in figure 3-11 and normalized to the same yield at (a) $L = 300$ and (b) $L = 150$.

Inelastic scattering of 7.5 MeV neutrons on the light elements C, N and O was present in the measurements from which figures 3-11 and 3-12 were obtained. However, the time-of-flight windows and pulse height thresholds used to obtain figure 3-12 precluded inelastic edges from appearing in this figure. For other elements such as Al, Si, Fe and Pb (figure 3-13) elastic and inelastic neutron energies are closer to one another since lower-lying states in these nuclides are accessible to excitation. Inelastic components were therefore not excluded (for these elements) by the time window W_T shown in figure 3-11(a). Figure 3-14 shows a perspective display of neutron events as a function of L and T_n measured by detector B for 7.5 MeV neutrons scattered from the graphite sample. The event group labeled **I** is attributed to neutrons which scatter inelastically from the sample with energy 1.79 MeV, after populating the first excited state of ^{12}C at 4.43 MeV. This group is delayed relative to the elastically scattered

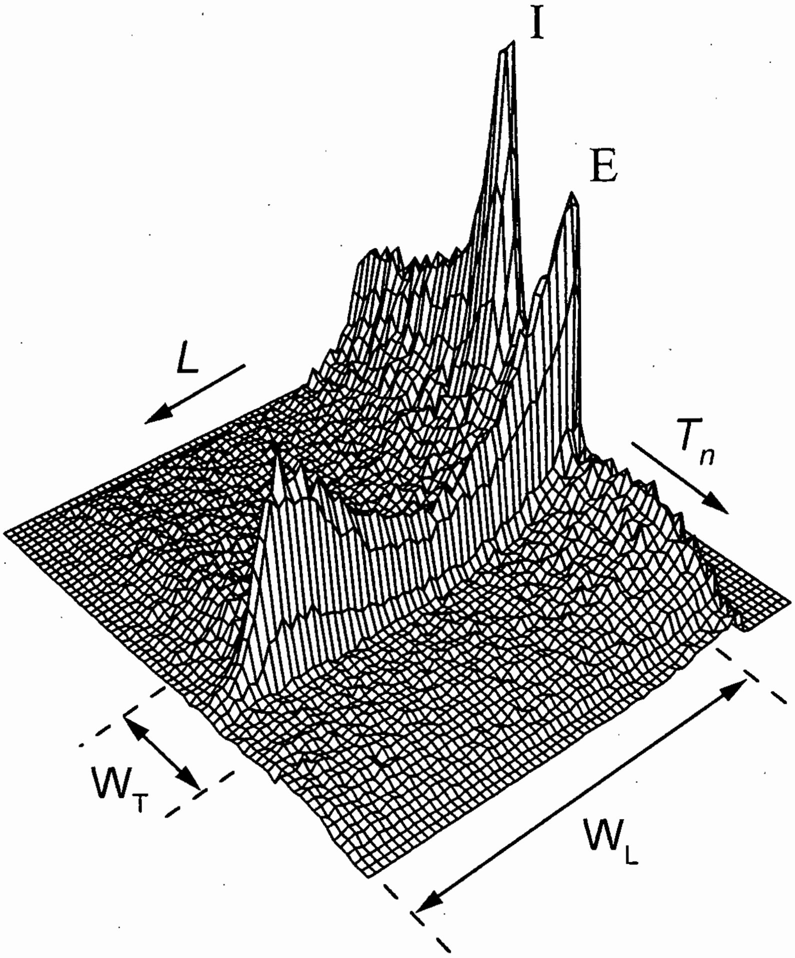

Figure 3-14
Counts (vertical) as a function of pulse height parameter L and time-of-flight parameter T_n, measured by detector B for 7.5 MeV neutrons incident on a graphite sample. The ridges are attributed to elastically scattered neutrons (E) and inelastically scattered neutrons (I) associated with excitation of the 4.43 MeV level of ^{12}C. The windows W_T and W_L are discussed in the text.

(5.46 MeV) neutrons, labeled **E**, due to the increased time-of-flight between scatterer and detector. The reduced scattered neutron energy is also responsible for the lower pulse height edge of the inelastic group. Inelastic scattering to the 0.72 MeV, 1.63 MeV and 2.31 MeV levels of ^{14}N (see figure 1-5) will produce features in the corresponding response function measured for ^{14}N. The 0.62 MeV neutrons from inelastic scattering to the 6.13 MeV level of ^{16}O fell below the pulse height threshold used for these experiments.

3.2.3 Energy dependence of backscattering from C, N and O

Figure 3-15 shows response functions measured for incident neutron energies of 6.8 MeV and 7.5 MeV scattered at 150° from the samples of graphite, nitrogen and water. The scales in figure 3-15 have been normalized so as to correspond to the counts that would be

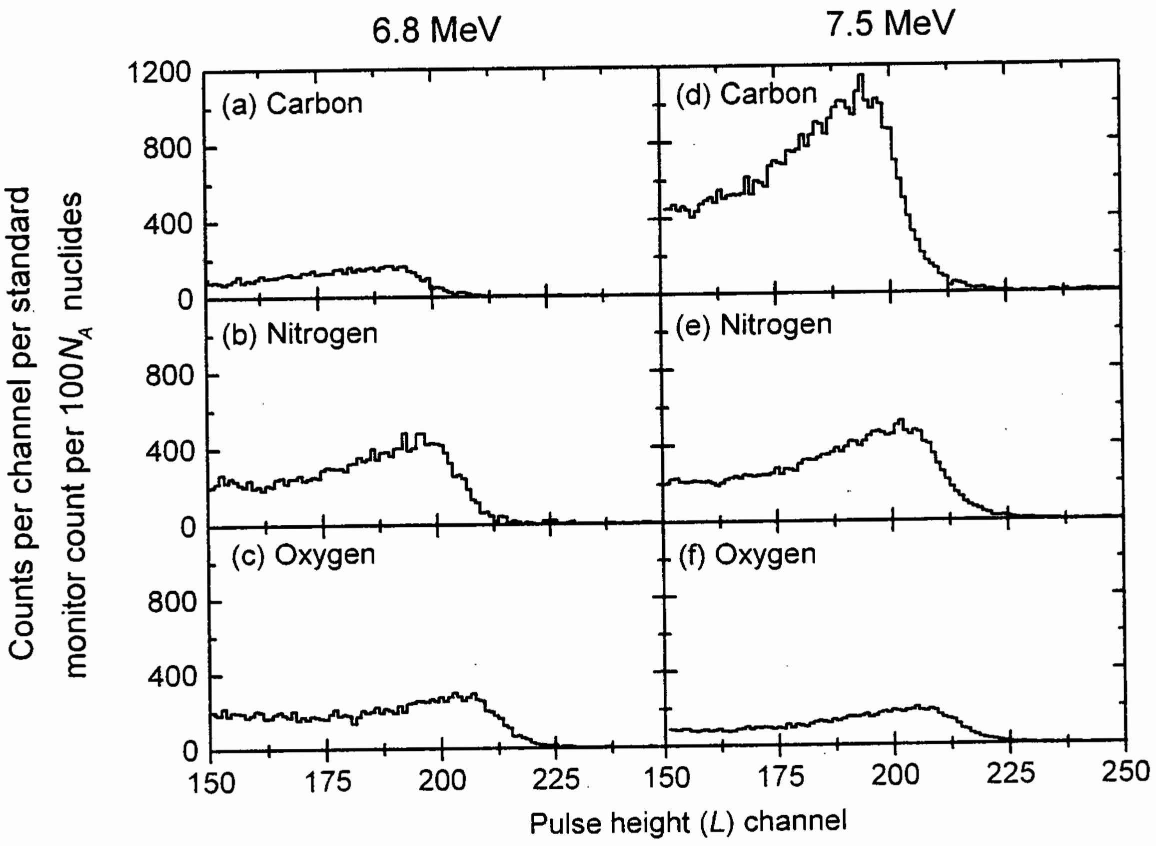

Figure 3-15 Response functions measured by detector B (NE230) at 150° for 6.8 MeV and 7.5 MeV neutrons incident on scatterers of: (a), (d) graphite; (b), (e) liquid nitrogen; and (c), (f) water. The data have been selected by the window W_T shown in figure 3-11 and the scales have been normalized so as to correspond to the counts that would be registered for a standard number of incident neutrons and to $100N_A$ target nuclei (^{12}C, ^{14}N or ^{16}O) in the scatterer.

registered for a standard number of incident neutrons (indicated by a standard count from the monitor M) and to $100N_A$ target nuclei (^{12}C, ^{14}N or ^{16}O) in the scatterer, where N_A is Avogadro's number. The intensities of these response functions provide a measure of the sensitivity of the system for detecting the scattering nuclide at each of these two energies. The measured intensities are proportional to the differential elastic scattering cross sections of the associated nuclides at $\theta = 150°$ at these incident energies (6.8 MeV and 7.5 MeV). The relative sensitivities for ^{12}C, ^{14}N and ^{16}O are consistent with data obtained from the time-of-flight measurements, described earlier in Section 2.3. The dominant feature in figure 3-15 is the enhanced yield for carbon at 7.5 MeV which is attributed to the resonance in the $^{12}C(n,n)^{12}C$ cross section at this energy (see figure 2-9).

3.3 Neutron scattering signatures for H, C, N and O

The pulse height spectra measured for neutrons elastically and inelastically backscattered from both light and heavy nuclides have been shown to be characteristic of the scattering nuclide, and hence are suitable for the elemental analysis of bulk samples. The anisotropies in the differential cross sections (figure 2-8) for neutron scattering are also distinctive for different scattering nuclides, therefore measurements made at a forward angle (e.g. 45°) used in conjunction with backscattering measurements may also be used to characterize the scatterer. In addition, scattering (other than multiple scattering) from hydrogen is kinematically confined to laboratory angles less than 90° (see equation 2.5) and is characterized (and therefore also distinguished) by a significant energy loss. For example, at laboratory angle 45° the neutron energy is halved after elastic scattering on hydrogen. Detector C (50 mm $\phi \times 50$ mm, NE213) was therefore installed at scattering angle 45° relative to the incident beam (see figure 3-1) in order to detect the neutrons scattered in this direction.

3.3.1 The scattering signature

The ridges in the L–T_n distributions of the type shown in figure 3-14, arising from the detection of neutrons which have been elastically and inelastically scattered from the same species of nuclide, suggest that a two-parameter analysis (L and T_n) could be useful to identify an unknown scatterer. Features of these ridges such as their locations (in L and T_n) and their intensity variation with L and T_n, depend on the kinematics of the scattering processes (elastic and inelastic), the geometry of the scatterer and detector system (figure 3-1), the detection efficiency of the scintillator for scattered neutrons of different energy and the differential scattering cross sections of the nuclide or nuclides in the scatterer. A set of measurements of the scattered neutrons at two energies and scattering angles leads to four L–T_n distributions (64 × 64 channels) and hence to 16k channels of data measured at two energies and two scattering angles. It can be seen, however, that the neutron scattering information most useful for identifying the scatterer is concentrated in a few regions of the L–T_n plane. A compact *scattering signature* was determined for each element (nuclide) by projecting selected sectors of the 2-parameter data onto the L-axis or the T_n-axis and then assembling the resulting set of L-components and T_n-components serially, into a single distribution (spectrum). The nuclide-specific information of the scattering signature is concentrated in two regions: firstly in the edge region of the projected pulse height spectrum observed for elastically backscattered neutrons (at 150°) selected by the windows W_T and W_L shown in figure 3-14; and secondly in the projected time spectrum selected by a low pulse height window applied to the neutron detector C, which detected neutrons scattered at 45°.

Figure 3-16 shows (as histograms) raw scattering signatures obtained from measurements using scattering samples of (a) graphite, (b) liquid nitrogen, and (c) water. Each signature in figure 3-16 contains components associated with neutrons scattered from the nuclides in the sample as well as components associated with the background. The signatures consist of two sections (see Table 3-7): channels 1-200 on the left, derived from the measurements at 6.8 MeV; and channels 201-400 on the right, derived from the measurements at 7.5 MeV. In each section the first 140 channels incorporate a component extracted from the projected L-spectrum measured by detector B (150°) and the last 60 channels incorporate a component extracted from the projected T_n-spectrum measured by detector C (45°). The extracted L-component extends from well below to well above the region in which pulse height edges are observed for scattering from ^{12}C, ^{14}N and ^{16}O. The extracted T_n-component includes peaks corresponding to both elastic and inelastic scattering. Each signature is thus a 400-channel distribution which contains energy and angular distribution information about the scattering of 6.8 MeV and 7.5 MeV neutrons on the nuclides of the associated sample. The count scales in figure 3-16 have been normalized so as to correspond to the counts that would be registered for a standard number of incident neutrons and to $100N_A$ target nuclei (^{12}C, ^{14}N or ^{16}O) in the scatterer. The solid and dashed curves in the figure are the results of fits to the data, described in Section 3.3.2 below. The background signatures (see figure 3-17) plotted as solid dots in figure 3-16 were obtained from measurements made using either an empty aluminium container or the empty Dewar at the sample position. In order to reduce the sensitivity of the unfolding analyses (Chapter 4) to the statistical fluctuations in these data, the background components were smoothed using a moving point polynomial method [Sa64]. These smoothed background scattering signatures are also shown in figure 3-17.

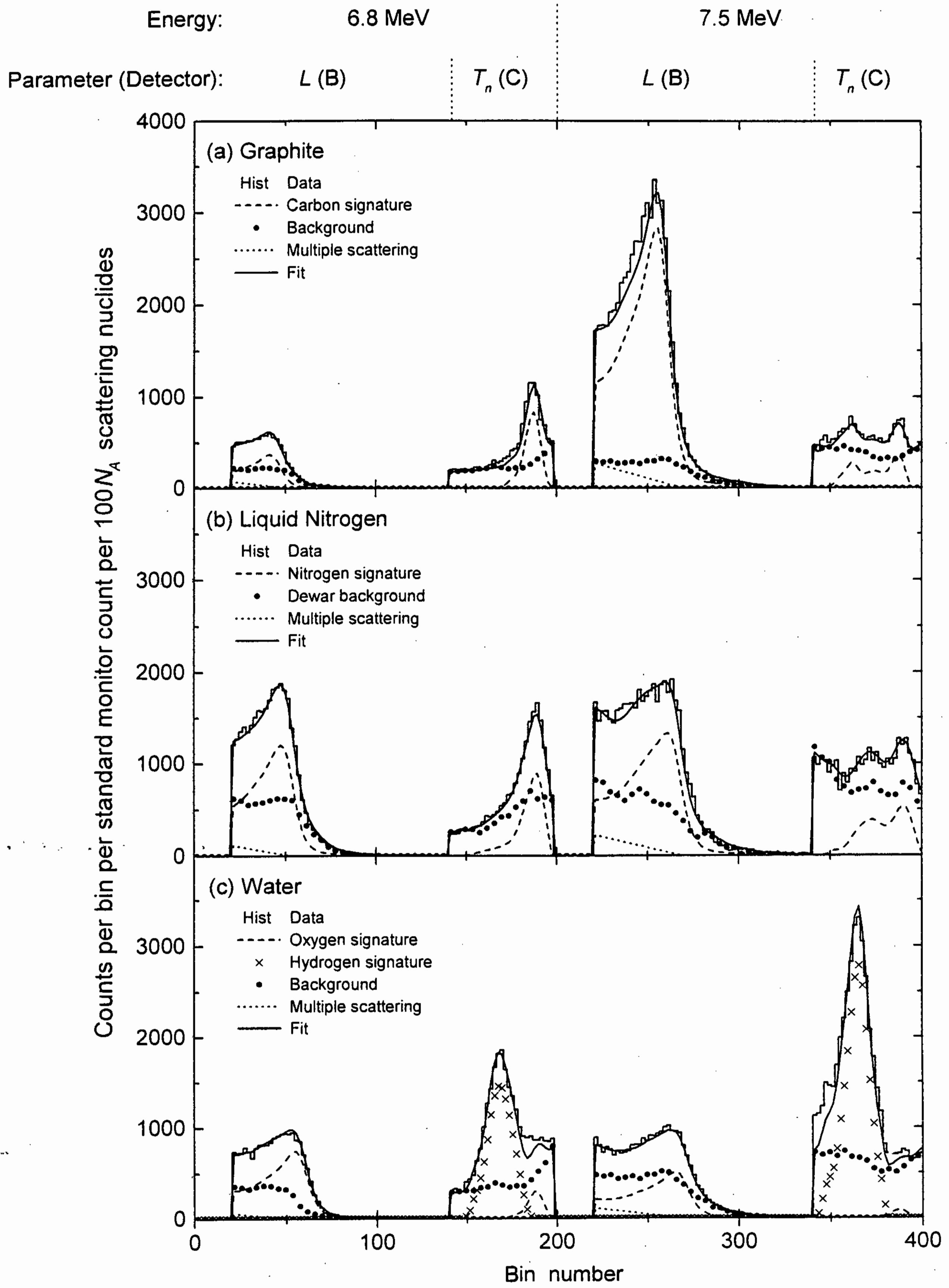

Figure 3-16 Raw scattering signatures (histograms) measured for (a) graphite, (b) liquid nitrogen and (c) water samples, and refolded fits (solid curves). Dashed curves show the C, N and O signature components and crosses in (c) show the H-signature component. Solid points and dotted lines show smoothed [Sa64] background and multiple scattering components. All measurements are normalized to a standard neutron monitor count and to 100N_A target nuclei in the scattering sample, where applicable.

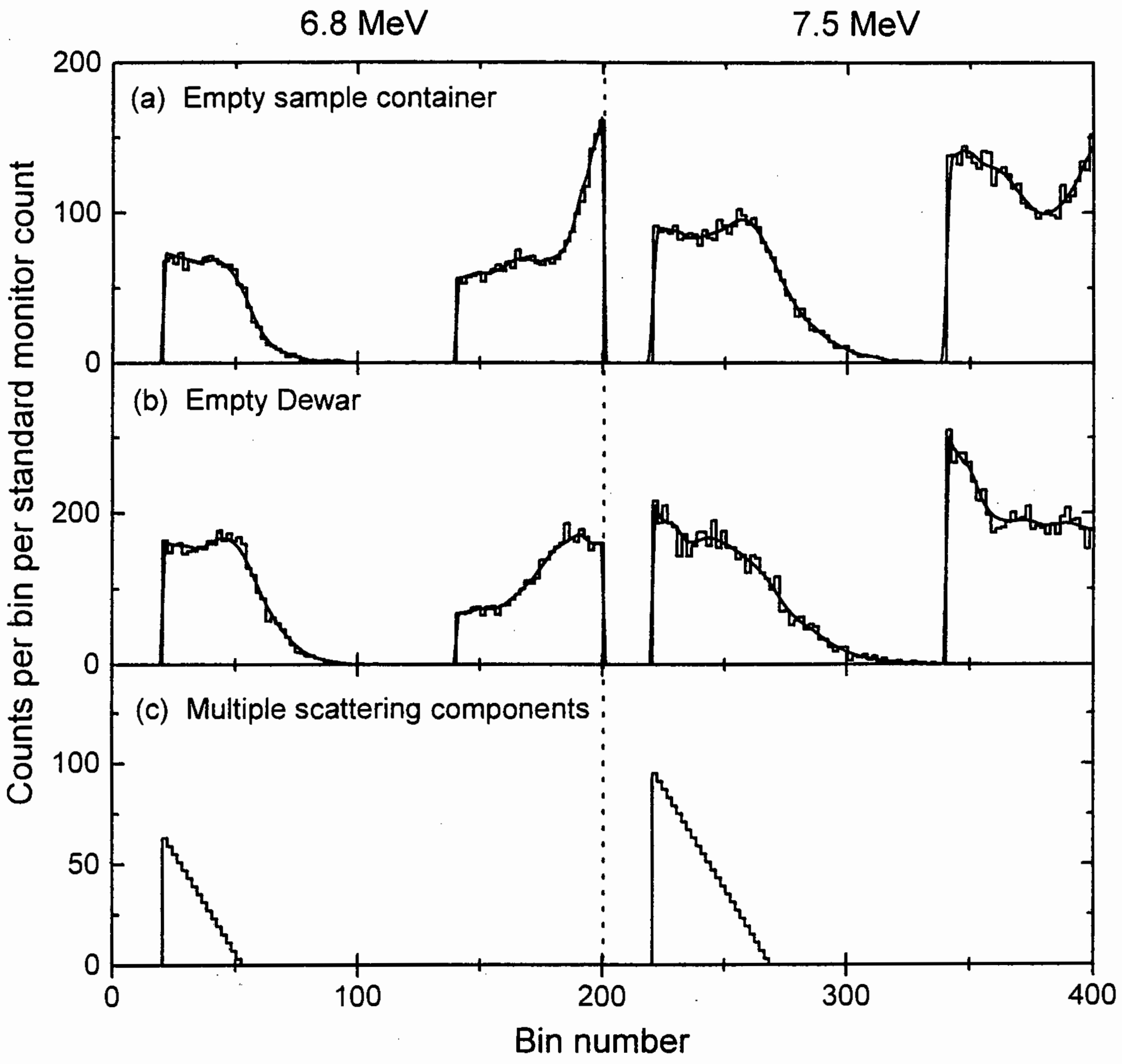

Figure 3-17 Measured (histograms) and smoothed [Sa64] scattering signatures for background scattering samples of (a) an empty sample container and (b) the empty Dewar. Also shown are (c) the straight line components used to model the multiple neutron scattering within the samples.

Additional components were introduced to model the contribution of multiple neutron scattering to each pulse height distribution in the scattering signature. Noting that multiple scattering may be expected to enhance the low energy region of the scattered neutron spectrum at the expense of the high energy region, components were chosen which decrease linearly (in the first order limit of a polynomial) with increasing L. These multiple scattering components are illustrated in figure 3-17(c) and shown as dotted lines in figure 3-16. The contribution of multiple scattering to the pulse height spectra was expected to be small due to the choice of thresholds used in the analyses.

Table 3-7 Components of the scattering signatures.

Channel number	**Energy**	**Parameter**	**Detector**	**Cut on parameter**
1 – 140	6.8 MeV	L	B	T_n
141 – 200	6.8 MeV	T_n	C	L
201 – 340	7.5 MeV	L	B	T_n
341 – 400	7.5 MeV	T_n	C	L

The raw scattering signatures in figure 3-16 illustrate some important features which underlie the FNSA technique for determining concentrations of the elements H, C, N and O in a scattering sample. Firstly, the small but significant increase of the edge pulse height on progressing from C to N and then to O can be seen, showing that backscattering measurements can resolve these elements from one-another. Secondly, after subtracting background, the change in intensity of both back- and forward-scattered neutrons with increase in incident neutron energy is seen to differ for the three elements. The projected T_n-components also vary with incident neutron energy in a way which is distinctive for the three different elements and the expected hydrogen peaks appear strongly in the signature measured for water shown in figure 3-16(c). The raw scattering signatures measured for the three samples shown in figure 3-16, and the background measurements (figure 3-17), provided data from which scattering signatures for the component elements, H, C, N and O, of these samples were derived. For the single-element samples, graphite and nitrogen, the C or N signature may be obtained, in principle, simply by subtracting the normalized background from the corresponding raw signature. A different procedure was followed, however, in order to obtain better statistical accuracy and to make some allowance for the effects of multiple neutron scattering on the measurements. Although the present discussion is focussed solely on the scattering measurements made by detector B (NE230), measurements were simultaneously made with detector A (NE213) as described in Section 3.1. The data measured by detector A are not presented here, although they indicated that this type of detector was also likely to be suitable for FNSA. A comparison between the relative performance of NE213 and NE230 for FNSA applications is presented in Chapter 5.

3.3.2 Construction of the scattering signatures

Each raw scattering signature in figure 3-16 was considered in two parts, corresponding to the 6.8 MeV and 7.5 MeV sections respectively. In fitting the graphite measurement (figure 3-16(a)) it was assumed that in the absence of multiple neutron scattering, the L-component of the *carbon* signature (each section) should have the same form as the lineshape (figure 3-7(b) or (d)) of detector B and could therefore be simulated by rebinning (re-distributing) this lineshape so as to match its edge pulse height to that observed in the scattering measurement (figure 3-16(a)). The L-component in each (raw) graphite signature (figure 3-16(a)) was therefore fitted by a sum of the following three components: the detector response function, rebinned as described above to represent the form of the carbon signature; the smoothed background function; and the linear component approximate the effect of multiple scattering. The T_n-component in each signature (from detector C at 45°) was fitted simultaneously with its associated L-component (from detector B at 150°). Gaussian functions were used to fit the elastic and inelastic scattering peaks in the T_n-components. The fitting procedure is described fully in Chapter 4. The results obtained for the 6.8 MeV and 7.5 MeV sections were then combined, giving the fit shown by the solid line in figure 3-16(a) and the carbon signature shown by the dashed line in the same figure.

The scattering signature for nitrogen was derived from the raw data (histogram) shown in figure 3-16(b) by following the same procedure as used for carbon, but with some important modifications demanded by the presence of inelastic neutron scattering in the signature. The contributions of these inelastic neutrons to the T_n-components in figure 3-16(b) were dealt with in the same way as for the lower energy inelastic neutrons in the carbon signature. Due to their higher energy however, the neutrons scattered inelastically from nitrogen encroached more strongly than those from carbon on the time window W_T (figure 3-14), thereby contributing small but significant proportions of low-energy neutrons to the L-components of the nitrogen signature (figure 3-16(b)). To allow for this effect, the data of figure 3-16(b) were fitted using L-components which included both elastic and inelastic contributions. The inelastic neutrons introduce additional edges at lower pulse height, due to their lower energy. The proportion of inelastic component required in the nitrogen signature was determined in the fitting and was found to be 5% at 6.8 MeV and 8% at 7.5 MeV. The dashed curve in figure 3-16(b) shows the scattering signature derived for nitrogen from the fitting.

The scattering signatures for hydrogen and oxygen were obtained from the raw data taken using the water sample, knowing that hydrogen makes strong and distinctive contributions to the T_n-components of the water signature (figure 3-16(c)) but no contribution to the L-components. The water signature was first fitted, following the same procedure as used for the carbon signature. The peaks due to hydrogen in the resulting fits (for 6.8 and 7.5 MeV respectively) were then identified and extracted to form the scattering signature for hydrogen[†]. The residual fit, after removal of these peaks, gave the scattering signature for oxygen. The components indicated by crosses and dashed lines in figure 3-16(c) show the signatures derived for H and O respectively. The proportions of multiple scattering determined from the fitting were 5% for C, 6% for N and 15% for O. The larger multiple scattering proportion measured for oxygen was expected in view of the presence of hydrogen in the water sample.

3.3.3 The HCNO scattering matrix

The 400-channel scattering signatures for the four elements H, C, N and O are shown together in figure 3-18. The signature for H is reduced by a factor of 2 relative to that shown in figure 3-16(c), due to the 2:1 ratio of H:O nuclei in water. The scattering signatures in figure 3-18 are combinations of projected L-spectra and projected T_n-spectra which embody, in a relatively compact form, the salient L and T_n features of the two-parameter distributions (16k pixels), such as those shown in figure 3-14. Each signature contains energy and angular distribution information about the scattering of 6.8 MeV and 7.5 MeV neutrons on the nuclides of the associated elements. The scattering signatures for the four different elements shown in figure 3-18 exhibit distinct individual characteristics. For example, the hydrogen signature is unique in having zero intensity in channels 1-160 and 201-360; a consequence of the kinematics of n-p elastic scattering, as previously explained. The backscattered L-components (channels 1-160 and 201-360) for C, N and O display upper limits which increase systematically with incident beam energy and with target mass number A, as expected from the kinematics of neutron backscattering. The L-components of the carbon signature show a strong dependence on the incident neutron energy, increasing in intensity with the energy change from 6.8 MeV to 7.5 MeV. The intensities of the corresponding components in the oxygen signature exhibit a weaker energy-dependence in the opposite direction. The low-energy forward-scattered components (channels 161-200 and 361-400) of carbon and nitrogen display characteristic inelastic scattering contributions. All of these features are consistent with expectations based on nuclear data such as differential cross sections [IAEA, Ro91] and excited state energies [Le78, Lo81], which were important guiding considerations in the choice of the incident neutron energies used, i.e. 6.8 MeV and 7.5 MeV.

[†] An improved method for obtaining the scattering signature for hydrogen was used in later studies (Chapter 5), based on measurements using samples of water and liquid oxygen.

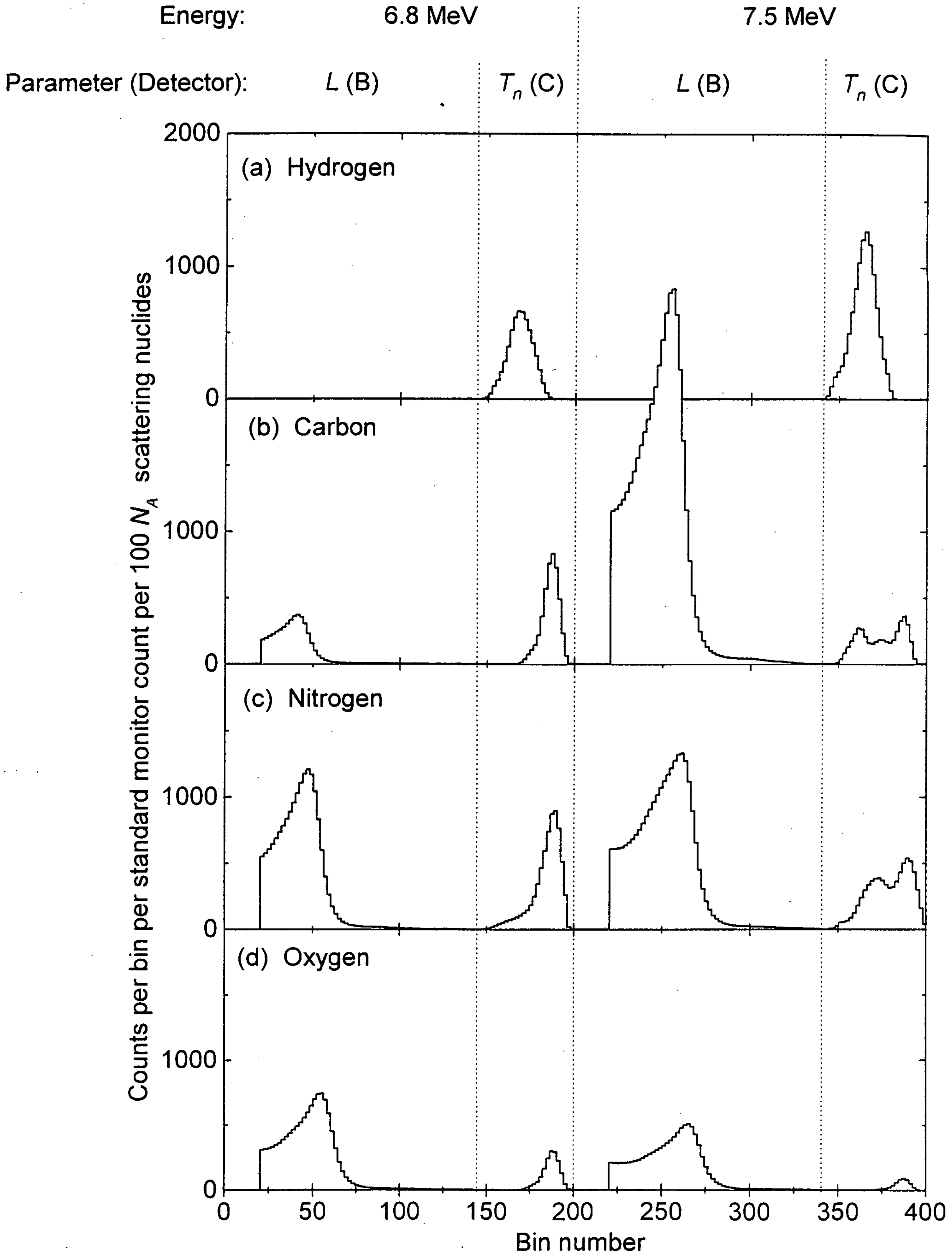

Figure 3-18 Neutron scattering signatures for the elements H, C, N and O. The scales have been normalized to the standard neutron monitor count and to 100N_A scattering nuclei.

The distinctive features present in the scattering signatures for the elements H, C, N and O make them well-suited for unfolding analyses. The scattering signatures shown in figure 3-18, the smoothed background signatures and the linear multiple scattering components (figure 3-17), together formed a *scattering matrix.* The next chapter describes how this scattering matrix was used to unfold raw scattering signatures measured for scattering samples of unknown composition, in order to determine the proportion, or atom fraction, of each element in the scatterer.

Chapter 4

Unfolding scattering signatures

Scattering signatures for the elements H, C, N and O have been derived from pulse height and time-of-flight measurements made at two incident neutron energies and two scattering angles. The distinctive features of these scattering signatures, which are specific to the scattering nuclide, makes them suitable for unfolding analyses. Raw scattering signatures derived from scattering measurements on compounds or materials composed from the elements H, C, N and O will be linear combinations of the scattering signatures for the constituent element (figure 3-18) and appropriate background components (figure 3-17). A deconvolution of such a raw scattering signature should therefore lead to the proportions of each element present in the scattering sample.

4.1 Particle spectrum unfolding

Techniques for the unfolding of measured multichannel distributions have mainly developed in two application areas: the determination of the energy spectra recorded by recoil detectors with fast neutrons, and the selection of the peaks present in spectra recorded by γ-ray spectrometers. The pulse height spectrum that is recorded from any radiation detector is the convolution of its inherent response function and the energy distribution of the incident radiation. Often the purpose of making the pulse height measurements is to obtain information about the energy spectrum of the incident radiation. This process generally involves solving the basic system of linear integral equations [We89]

$$z_i = \int_0^\infty R_i(E)\,\phi(E)\,dE \qquad \text{for } i = 1 \text{ to } m \tag{4.1}$$

which represent a model of the measurement. The z_i denote the input measurands, for example data given in terms of a recorded pulse height frequency distribution. The kernels $R_i(E)$ are the response functions of the measuring system which are assumed here to include the effects of limited energy resolution of the detector. The spectrum parameters $\phi(E)$ can be considered as the average fluence values in the intervals between the energies E_i and E_{i+1}. The subscript i is related to the channel number of the measuring system having m channels in total.

Mathematically, equation 4.1 is a degenerate case of the Fredholm integral equation of the first kind [We95], which can be transformed in a variety of ways [Pu93, We89, We95] into the discretised matrix equation

$$\mathbf{z} = \mathbf{R}\,\boldsymbol{\Phi}. \tag{4.2}$$

Equation 4.2 represents a system of linear equations which must be solved for the column matrix $\Phi = (\phi_1 \ldots \phi_n)^T$ where the superscript T indicates transposition. Data values are assumed to be given for both the column matrix $\mathbf{z} = (z_1 \ldots z_m)^T$ of the input measurands and the response matrix $\mathbf{R} = R_{ij}$ $(i = 1 \ldots m\ ;\ j = 1 \ldots n)$. The matrix elements z_i, ϕ_j and R_{ij} are always non-negative otherwise they would not have any physical meaning. The response matrix **R** is assumed to be known with negligible uncertainty, however, the column matrix **z** usually possesses a statistical uncertainty that is expressed by the covariance matrix $\mathbf{S_z}$. If **z** is a measured pulse height (multichannel) spectrum, then $\mathbf{S_z}$ is diagonal, with elements assuming independent Poisson distributions of the event frequencies. The statistical uncertainties in the measured pulse height spectra will propagate through the unfolding calculation and give rise to corresponding variances in the calculated energy spectrum.

A unique solution Φ cannot generally be obtained by simply inverting equation 4.2. Instead, a best estimate of Φ may be determined by seeking a minimum in the weighted sum of residuals χ^2 where [Be69]

$$\chi^2 = \sum_i W_i \left(z_i - \sum_j R_{ij}\phi_j \right)^2 \tag{4.3}$$

and the weighting factors W_i are often chosen to be inversely proportional to statistical variance of each data point. The process of minimizing this sum of residuals amounts to a least squares fitting to the measured data. There exist many unfolding algorithms based on the least squares method which have been realized in codes such as LOUHI [Ro80], STAY'SL [Pe77], SAND-II [Mc67] and FERDOR [Bu65]. Although the least squares approach is very powerful, there are a number of inherent difficulties [Ma97]. For example, in order to produce consistent solution spectra, many of these codes require some prior, or *a priori*, information, for example in the form of a pre-calculated fluence vector Φ_0 with an uncertainty matrix $\mathbf{S}_{\Phi 0}$. However, if $\mathbf{S}_{\Phi 0}$ contains large uncertainty components, non-physical results such as negative elements of the solution vector may result. Furthermore, many established least squares codes have evolved from algorithms which were written before the availability of cheap, fast computers, with the result that uncertainties are often handled in a cumbersome or non-transparent way. With the advent of modern computer hardware, an alternative to least squares deconvolution has become a viable option, namely the Monte Carlo method.

4.2 The MIEKE Monte Carlo code

Bayesian probability theory [Ja90, Sk89] provides a general and consistent framework for logical inference and has been applied successfully in various data analysis problems that are statistical in nature, for example the deconvolution of PIXE and RBS spectra [Fi98, Pr98]. Although the Bayesian formalism is well-grounded theoretically [Sk91], the generality of the technique causes relatively simple problems to become mathematically demanding to solve analytically. This difficulty can be overcome in the context of spectrum unfolding by making realistic approximations and assumptions and applying a Monte Carlo method in which not the most probable fluence (minimum χ^2), but its expectation value from a certain probability distribution is evaluated. It is then possible to construct an *a posteriori* probability density of the fluence using Bayes' theorem [Je67, Ja90]. The solution spectrum is then defined as the expectation value of Φ, denoted by $\langle\Phi\rangle$, which can be calculated from this probability density. Here the term "a posteriori" characterizes the knowledge level after each step or cycle of the unfolding calculation.

The MIEKE Monte Carlo code [Ma85, We95], part of the HEPRO spectrum unfolding package [†] [Ma94, Ma97], was chosen for the present studies. The algorithm in the MIEKE code

---

[†] Available from Physikalisch-Technische Bundesanstalt (PTB), Bundesallee 100, Braunschweig, Germany. The package includes unfolding codes based on a variety of algorithms as well as tools for spectrum adjustment such as Gaussian broadening and spectrum refolding.

is based on simple probability arguments [Ti88, Ti93] and requires a probability distribution [We89] for randomly selecting spectra. The distribution is needed to numerically describe the actual state of incomplete knowledge of the true spectrum to be determined. In the MIEKE code, a probability density is developed [see Appendix A] by an importance sampling method for the resulting spectral fluence so that expectation values with confidence intervals can be assigned. Using information theory [Le89, Ja90] it is possible to describe a statistical system of a multidimensional random variable x by a probability density $P(x)$ and for which the expectation value of the so-called entropy

$$S = -k \int P(x) \log(P(x)) dx \tag{4.4}$$

has a maximum value [We95]. Using this principle of maximum entropy [Ja57], a probability density for Φ can be constructed [We87, We89] of the form

$$\begin{aligned} P(\Phi) &= C_0 \exp\left(-\frac{\beta}{2}\chi^2(\Phi)\right) && \text{for all } \Phi_i \geq 0 \\ P(\Phi) &= 0 && \text{for } \Phi_i = 0 \end{aligned} \tag{4.5}$$

where C_0 is a normalization constant to be determined from the constraint that

$$\int P(\Phi) \mathrm{d}\phi_1 \ldots \mathrm{d}\phi_n = 1. \tag{4.6}$$

The parameter β is analogous to a temperature in statistical mechanics and is determined from the condition that the expectation value of χ^2, defined as

$$< \chi^2 > = < (\mathbf{z} - \mathbf{R}\Phi)^{\mathrm{T}} \mathbf{S}_{\mathbf{z}}^{-1} (\mathbf{z} - \mathbf{R}\Phi) >, \tag{4.7}$$

should be equal to the number of degrees of freedom involved, namely the number of channels m in the spectrum **z**. When $\beta = 0.5$, $P(\Phi)$ is equivalent to the likelihood expression used in Bayes' theorem (see Appendix A) if a normal distribution is assumed for the measured data [Ma85].

The MIEKE code makes use of the probability density of equation 4.5 and a Monte Carlo importance sampling algorithm is used to calculate expectation values (see Appendix A). The basic idea used to approximate the expectation values is to average over a set of Φ vectors taken from near the region of maximum probability [Wo68]. The computing algorithm consists of performing a sampling random walk in the n-dimensional space spanned by the n axes of Φ, and then certain Markov-chain probabilities [Wo68] are used to produce successive sets of fluence vectors in each iteration.

The Monte Carlo method of unfolding [Ma85, We95], as realized in the MIEKE code, has several advantages: it requires no special model needing prior information as do other some methods [Mc67, Ti88] and it extracts the maximum information from the data. A consistent treatment of the uncertainties is also produced. The MIEKE code has successfully been used in a number of applications, including the unfolding of the responses of ^{3}He detectors to neutrons [Di93] and NE213 detectors to photons [Bu93]. In particular, it has been used with success for the determination of energy spectra of the measured counts from Bonner sphere detectors. This application is an example of the so-called 'few channel' unfolding problem and represents an undetermined case of equation 4.2, since the neutron fluence values must be calculated from the counts of a small number of Bonner sphere detectors before the dose equivalent can be determined [Ma88]. In such situations the least squares approach is not always suitable since it could lead to numerical difficulties [Ma88] when inverting equation 4.2.

4.3 Tests of FNSA on HCNO compounds

4.3.1 Measurements

Raw scattering signatures of the same form described in Section 3.3 and illustrated in figure 3-18 were derived from pulse height and time-of-flight measurements using scattering samples of methanol, ammonium nitrate, ammonium acetate and acetamide (see Table 3-3). These compounds were chosen because they were readily available in pure form, are easy and safe to handle, and provided a variety of combinations of the elements H, C, N and O. The raw scattering signatures for these compounds were derived from measurements made under the same experimental conditions as for the scattering signatures for elements and backgrounds described in Section 3.3. Therefore the proportions of the elements within these compounds may be determined through a deconvolution of each raw scattering signature into its constituent elemental and background components.

4.3.2 Fits to HCNO compounds

The matrix equation 4.2 may be written in the form

$$z_i = \sum_{j=1}^{n} R_{ij} \phi_j \tag{4.8}$$

where the column matrix $z_i = (z_1 \ldots z_m)^T$ is now taken to represent the raw scattering signature measured for the test HCNO sample and the matrix $\mathbf{R} = R_{ij}$ $(i = 1 \ldots m\, ; j = 1 \ldots n)$, which is now referred to as the *scattering matrix*, was constructed to include the following: $j = 1$ to 4, the scattering signatures for the elements H, C, N and O (figure 3-18); $j = 5$ and 6, the smoothed signatures (figure 3-17(a)) based on background measurements made at 6.8 MeV and 7.5 MeV respectively; and $j = 7$ and 8, the linear functions (figure 3-17(c)) which were designed to model multiple scattering contributions at 6.8 MeV and 7.5 MeV respectively. The scattering matrix **R** therefore comprised $j = 1$ to 8 columns (elements and backgrounds) and $i = 1$ to 400 rows (signature channels). Each MIEKE unfolding analysis determined expectation values and standard deviations for the n coefficients ϕ_j which gave the "best" fit to the scattering signature z_i of the particular sample.

Figures 4-1(a) to (d) show raw scattering signatures (histograms) derived from measurements of neutron scattering from the four test compounds, each normalized to the standard number of monitored incident neutrons. Also shown in each figure are refolded MIEKE fits (solid curves) to the raw signatures, together with the constituent components of each fit: the H, C, N and O scattering signatures (figure 3-18) indicated by crosses, solid circles, triangles and open circles respectively; and background signatures and multiple scattering components indicated by dashed and dotted curves respectively. The linear multiple scattering components contributed approximate proportions of 5% to the fits. Since the measured scattering signatures for the elements H, C, N and O were normalized so as to correspond to a scatterer containing $100N_A$ nuclei of the element j, the fitting factor ϕ_j determined in the analysis indicated the presence of $100\,\phi_j N_A$ nuclei of this element in the particular test scattering sample. The total number of nuclei in the HCNO scattering sample is thus given by

$$N_{tot} = 100\ N_A \sum_{j=1}^{4} \phi_j \tag{4.9}$$

and the atom fraction a_j for element j in the sample is given by

$$a_j = \frac{\phi_j}{\sum_{j=1}^{4} \phi_j}. \tag{4.10}$$

The mass M of the scattering sample, in kg, is given by

$$M = 0.1 \sum_{j=1}^{4} \phi_j A_j \tag{4.11}$$

where A_j is the mass number of nuclide j.

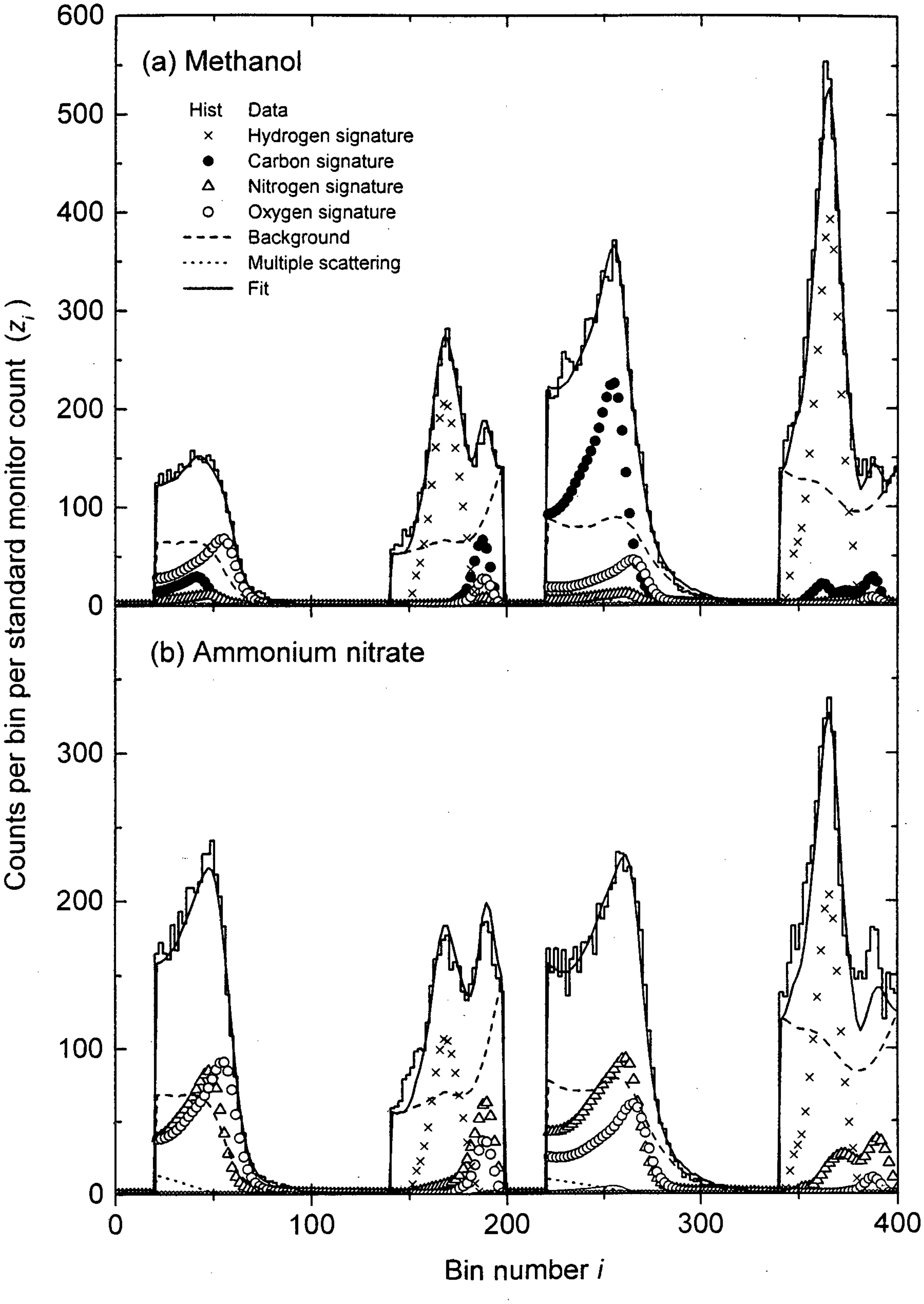

Figure 4-1 *Measured raw scattering signatures (histograms)* z_i *and refolded MIEKE fits (solid curves) for samples of (a) methanol and (b) ammonium nitrate. The H, C, N and O components determined in the fitting are shown by crosses, solid circles, triangles and open circles respectively. Dashed and dotted curves show the smoothed backgrounds and linear multiple scattering components.*

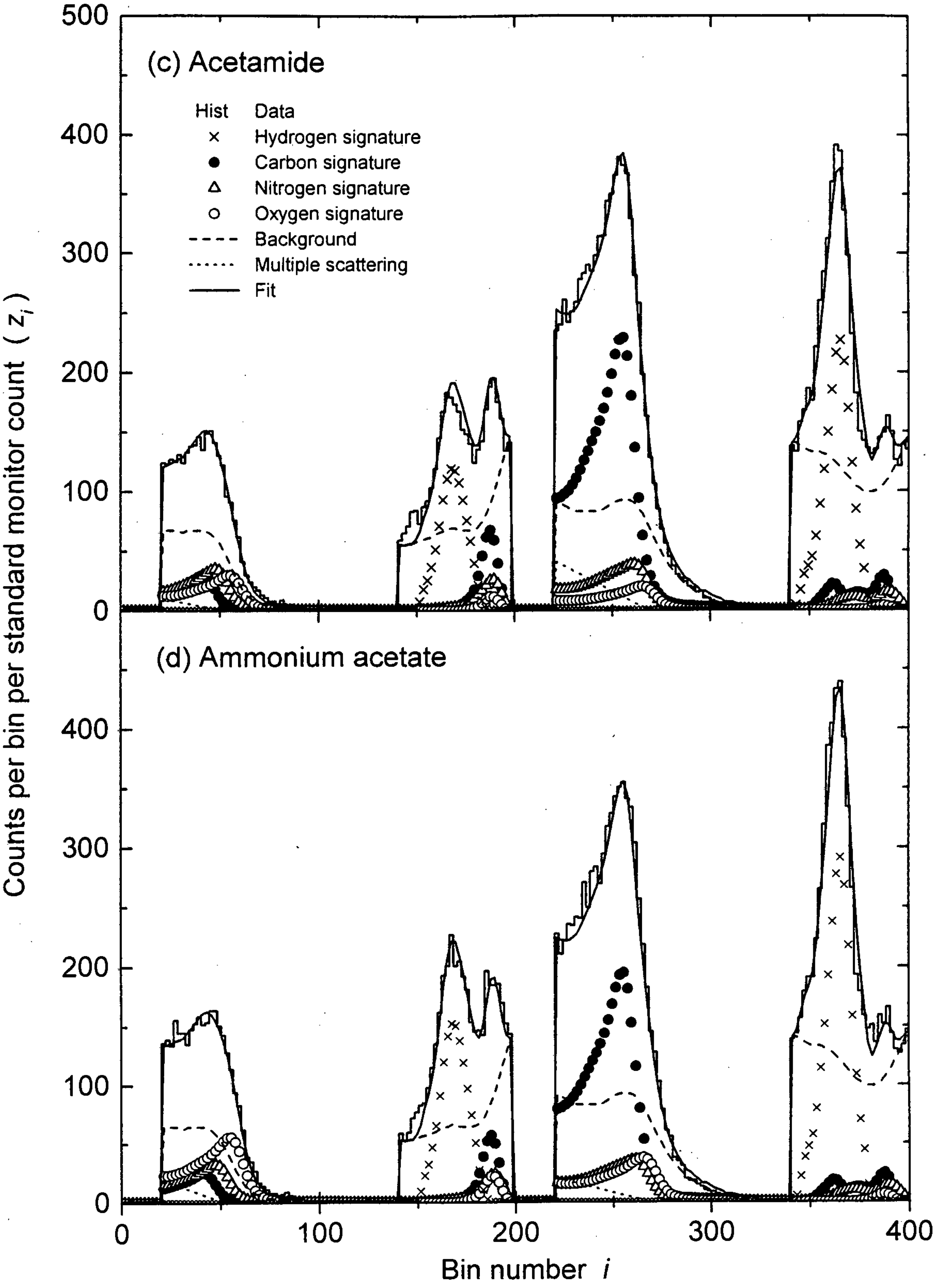

Figure 4-1 continued. Measured raw scattering signatures (histograms) z_i and refolded MIEKE fits (solid curves) for samples of (c) acetamide and (d) ammonium acetate. The H, C, N and O components determined in the fitting are shown by, crosses, solid circles, triangles and open circles respectively. Dashed and dotted curves show the smoothed backgrounds and linear multiple scattering components.

4.3.3 Results

Atom fractions and sample masses determined from equations 4.10 and 4.11, are listed in Tables 4-1 and 4-2 respectively, together with known values of a_j and M determined from the chemical formulae and by weighing respectively. Figure 4-2 compares atom fractions (points) determined from the unfolding analyses with theoretical values (histograms). The atom fraction values are measured to within two standard deviations of the known values for both a_j and M for all four test samples. These results demonstrate that the combination of scattering signature measurements of the type described in Section 3.3 with the unfolding analysis available through use of the code MIEKE is very effective for identifying and measuring concentrations of the elements H, C, N and O.

Table 4-1 Atom fractions measured from unfolding analyses for four HCNO test compounds. Values in square brackets are calculated from the empirical formulae.

Sample	***Atom fraction a_j***			
[Formula]	***H***	***C***	***N***	***O***
Methanol [H_4CO]	0.633(24) [0.667]	0.163(10) [0.167]	0.018(8) [0]	0.186(12) [0.167]
Ammonium nitrate [$H_4N_2O_3$]	0.455(23) [0.444]	0.003(3) [0]	0.198(8) [0.222]	0.345(25) [0.333]
Acetamide [H_5C_2NO]	0.544(12) [0.555]	0.246(24) [0.222]	0.088(15) [0.111]	0.122(18) [0.111]
Ammonium acetate [$H_7C_2NO_2$]	0.574(45) [0.583]	0.172(10) [0.167]	0.067(17) [0.083]	0.187(10) [0.167]

Table 4-2 Sample masses determined from the unfolding analyses and weighing.

Sample compound	***Sample mass M (kg)***	
	Experiment	***Weighing***
Methanol	0.285(13)	0.288
Ammonium nitrate	0.311(15)	0.298
Acetamide	0.220(15)	0.212
Ammonium acetate	0.264(13)	0.272

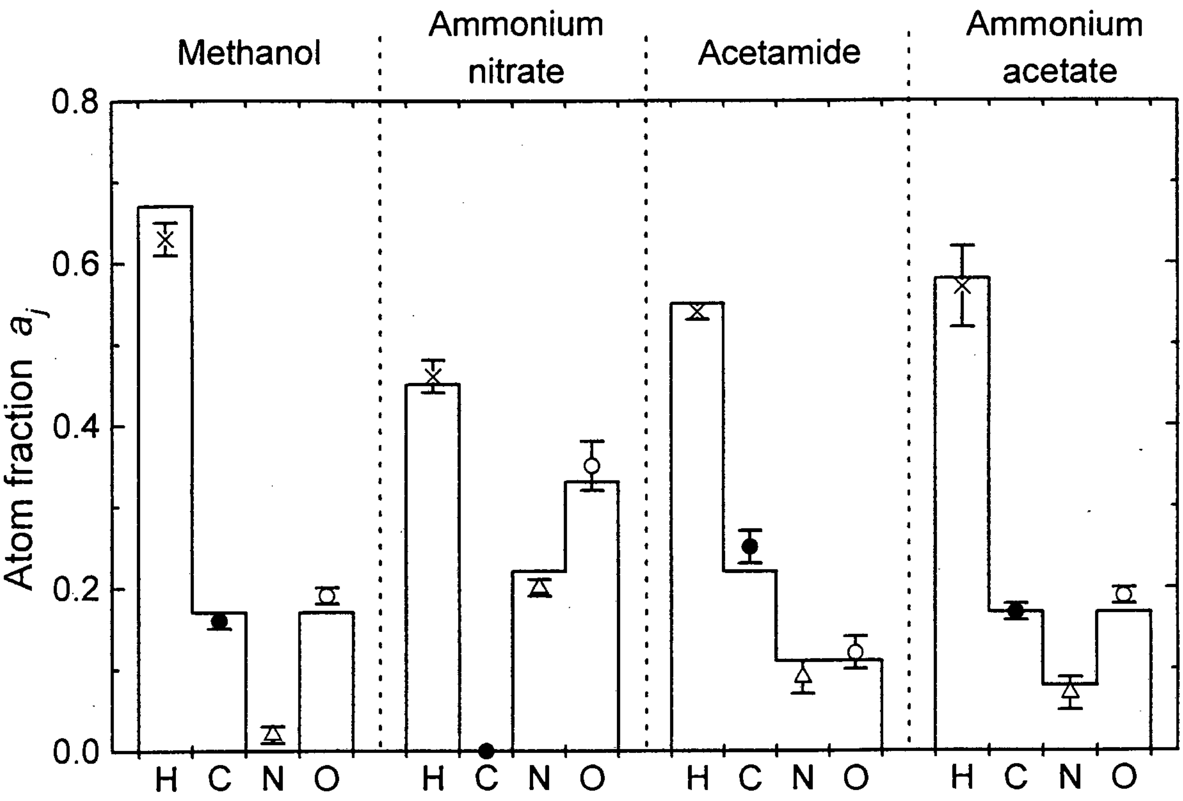

Figure 4-2 *Atom fractions a_j, calculated (histograms) from stoichiometry and measured (points) from unfolding analyses, of the elements hydrogen (crosses), carbon (solid circles), nitrogen (triangles), and oxygen (open circles); comprising the four test compounds of methanol, ammonium nitrate, acetamide and ammonium acetate.*

The time required to complete the interrogation of a typical package, for example of volume 0.5 m^3, will clearly be a critical consideration in determining whether a FNSA system is suitable for practical implementation. Part of this time is related to the computer analyses of the measurements. The computing time for the MIEKE code depends quadratically on the number of channels in the scattering signature [Ma94]. It was determined empirically that 100 000 Monte Carlo realizations of the scattering signatures were sufficient for the expectation values of $\phi_j \pm \Delta\phi_j$ to converge to six significant figures in a consistent fashion. This translated to a real computing time of approximately 600 seconds on a Pentium PC (133 MHz, 32 MB RAM). This may appear to be a prohibitively lengthy time to analyze each voxel of an object of size 0.5 m^3 in this way. However, it is envisaged that this time may be significantly reduced by both improving the computing power and applying a faster unfolding algorithm[†], which may be achieved [We89, We95], for example, by using alternative forms of the probability density function (equation 4.5). Furthermore, in a practical situation such as the search for contraband at airports, the type of unfolding analysis described here would not need to be completed for *all* voxels of the object (suitcase). Regions of enhanced scattering would first be located by some alternative method (see Chapter 6) which would result in only a few number of voxels within the extended object possibly needing to be analyzed in this way.

The results in figure 4-2 suggest that the FNSA method, or possibly a variation of this method based on a differently defined signature, could be developed into a useful (and perhaps faster) non-intrusive neutron interrogation system for small packages. Further work (Phase 2, see Table 3-1) was undertaken to explore this possibility, including investigations of the effect of additional elements (other than H, C, N or O) in the sample on the measurement of H:C:N:O concentrations, effects arising from the attenuation of neutrons in the interrogated material before and after scattering, and techniques that could be used to locate different scattering centres in an extended sample volume.

[†] There exist other Monte Carlo codes, such as MLMHE3 [Av95] and BUNTO [Lo84], which differ in their computing demands and handling of uncertainties. No attempt was made to determine the most time-efficient unfolding method, although it is recognized that this is an important issue in a practical situation.

Chapter 5

Identification of materials

The atomic concentrations of hydrogen, carbon, nitrogen and oxygen in small samples (0.2 - 0.3 kg) have been measured to an accuracy of a few percent. Pulsed neutron beams of energies 6.8 MeV and 7.5 MeV were used to irradiate the samples and the scattered neutrons were detected at both forward (45°) and backward (150°) angles. Scattering signatures for the elements H, C, N and O were derived from time-of-flight and pulse height measurements and were used to unfold raw scattering signatures measured for samples of unknown elemental composition, in order to determine the atom fraction of each element in the samples.

The exploratory studies (Phase 1, see Table 3-1) were mainly confined to measurements on materials composed exclusively of H, C, N and O. The ultimate objective of this work, however, is to determine whether the Fast Neutron Scattering Analysis technique can be developed to a level which will be useful for the non-intrusive identification of small quantities of contraband hidden among materials composed of any common elements, in packages of volume up to about 0.5 m^3. With this in mind, further scattering studies were undertaken (Phase 2, Table 3-1) to investigate the following: (a) the effect of additional elements (other than H, C, N or O) in the sample, on the measurement of H:C:N:O concentrations; (b) the relative performance of NE230 and NE213 detectors for FNSA application; (c) the effects of neutron interactions in any other material close to the sample, especially material in the incident neutron beam, or between the sample and the detectors; (d) the effect of sample position (along the beam) on the signature measurement; and (e) alternative ways for defining scattering signatures which are more effective and/or simpler for element identification.

5.1 Scattering measurements

The neutron production and data acquisition system for the Phase 2 studies was similar to that described in Section 3.1, although the experimental arrangement was extended in a number of ways. The shadow shield used for the Phase 1 studies was replaced by a wall consisting of sections of natural iron and borated paraffin wax, constructed to shield all detectors against neutrons emanating directly from the target (see figure 5-1). Circular apertures of diameters 2.5 cm and 10 cm were constructed in the iron and wax sections, respectively, which provided a collimated neutron beam of approximate cross sectional area of 30 cm^2 at the sample position (1.50 m from the target). An 1 mm copper plate (CS) was positioned as shown in figure 5-1 to scatter neutrons out of the beam into the monitor detector M (NE213, 50 mm ϕ × 50 mm) mounted within the shielding wall.

In order to accumulate data alternately at two energies without operator intervention, the neutron beam energy was cycled between 6.8 MeV and 7.5 MeV by rotating an 11 μm Havar foil in and out of the deuteron beam (see figure 5-1). The foil (4.0 cm ϕ) was mounted on a light aluminium frame in an evacuated chamber approximately 10 cm upstream from the target. When in the beam it degraded the energy of the deuteron beam entering the target cell from 4.7 MeV to 4.0 MeV. The cycling of the Havar foil was controlled by a logic module which counted neutrons detected by the monitor detector (M). After a pre-set number of counts was reached, a slave unit in the experiment vault was signaled to activate a motor attached to an arm which rotated the frame holding the Havar foil via a pulley. After the frame was rotated through 180°, a microswitch caused the motor to stop and a signal was returned to the logic control module to reset its internal counter. The rotating of the Havar foil took less than 3 seconds during which time the acquisition system was paused by a busy signal from the control module. The frequency of energy changing was typically of the order of 2 minutes, depending on the deuteron beam current. The mean square angle of divergence $<\theta^2>$ of the 4.0 MeV deuteron beam transmitted by the 11 μm Havar degrader was calculated to be 0.62° using [Ma69]

$$<\theta^2> = 1.3\times10^{-23}\,\frac{z^2}{E^2}\,N\,t\,Z^2\,\ln\left(\frac{E}{Z^{\frac{4}{3}}z}3.7\times10^4\right) \tag{5.1}$$

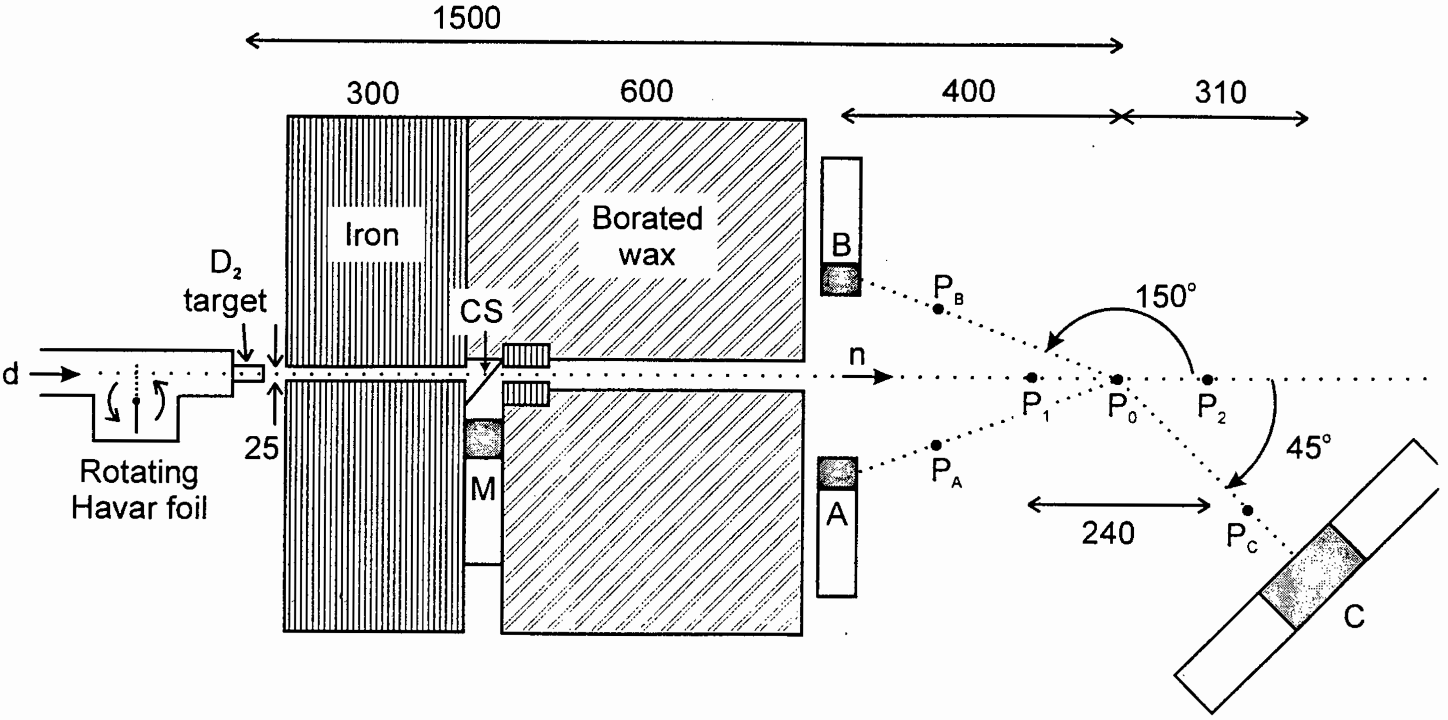

Figure 5-1 Schematic diagram of the arrangement used for the Phase 2 scattering measurements. An aperture in the iron and borated paraffin wax shielding wall provided a collimated beam at the scattering positions (P_1, P_0 and P_2). The incident deuteron beam energy was cycled between 4.0 MeV and 4.7 MeV by rotating an 11 μm Havar foil in and out of the beam. A copper plate CS scattered neutrons into the beam monitor detector M. Point to point distances are in mm.

where E is the incident beam energy in MeV, z is the atomic number of the incident beam particles, Z is the atomic number of the degrading material, N is the number of nuclei in the material per cm^3 and t is the thickness of the material in centimetres. It was estimated that multiple Coulomb scattering in the Havar foil spread the incident deuteron beam from approximately 0.5 cm ϕ to 0.7 cm ϕ before entering the target cell.

One or more scattering samples were mounted with their centres at the positions P_1, P_0 or P_2, 12 cm apart (see figure 5-1), and the scattered neutrons were detected by liquid scintillators at mounted forward and backward scattering angles. Detector A (NE213, 40 mm ϕ × 30 mm) and detector B (NE230, 40 mm ϕ × 30 mm) were positioned at scattering angle 150°, each on either side of the collimator in the horizontal plane defined by the beam height. Scattering data were measured simultaneously with detector A and detector B in order to compare the relative performance of NE213 and NE230 scintillators for FNSA applications. As a first step towards the use of large detector volumes, a NE213 detector of dimensions 13 × 13 ×

7 cm^3 replaced the smaller detector mounted at 45°, described in Chapter 3. Each of the two glass faces (see figure 5-2(a)) of this detector were optically coupled to two RCA-8850 photomultipliers. The anodes of the four photomultipliers were linked to form a single output signal and the high voltage supplies of the individual photomultipliers were adjusted to match their gains. Figure 5-2(b) shows lineshapes measured with detector C mounted at 0°, in a similar way described in Section 3.1.4, for neutrons of incident energy (i) 6.8 MeV and (ii) 7.5 MeV. The enhancements in the lineshapes adjacent to the upper pulse height edges are attributed to multiple scattering in the detector. These are more pronounced for this detector than for the lineshapes measured for detectors A and B (figure 3-7), since these detectors are much smaller in volume (less than one tenth) than detector C. For the scattering studies, the (new) detector C was positioned at scattering angle 45° with its square face facing P_0. The distances between P_0 and the centres of detectors A, B and C were 42.5 cm, 42.5 cm and 44.0 cm, respectively.

The scattering samples studied included carbon (graphite), liquid nitrogen, liquid oxygen, aluminium, sulphur, iron and lead, and compounds of these elements with one-another and with the elements hydrogen, lithium and boron (see Table 3-4). Measurements were made with one, two or three scattering samples in the neutron beam and also with scattering materials at various positions outside the incident neutron beam, where they might affect signals recorded by the detectors. The data taken using additional material in or outside the beam were analyzed so as to determine the effects of this material on the scattering signatures. Unless indicated to be otherwise, all measurements referred to below were made using a single scattering sample centred at position P_0, with the axis of the sample aligned with the axis of the incident neutron beam. Exceptions to this configuration were the liquid nitrogen and liquid oxygen samples, which were contained in a spherical Dewar flask of inner diameter 100 mm. Backgrounds were measured using either no sample or an empty sample container at the appropriate position (P_0, P_1 or P_2) and all measurements were normalized to the same incident neutron flux based on the counts recorded by the monitor M. Each run was typically completed during 90 minutes, representing about 6.5 mC of integrated beam current on target.

The data acquisition system was essentially the same as that described in Section 3.1.3, except that an additional LINK 5010 PSD unit was introduced which processed the anode signals from detector C. The anodes of detectors A and B were coupled together and fed into a common LINK unit. The signals from the dynode outputs from each photomultiplier were used to code the events from each detector via a pattern register. All in all, six pattern register bits were used to code the events measured by each of the four detectors (A, B, C and M) at the two energies of 6.8 MeV and 7.5 MeV. The data were written (see Section 3.1.3) in multiparameter, event-by-event mode to disk for later off-line analysis.

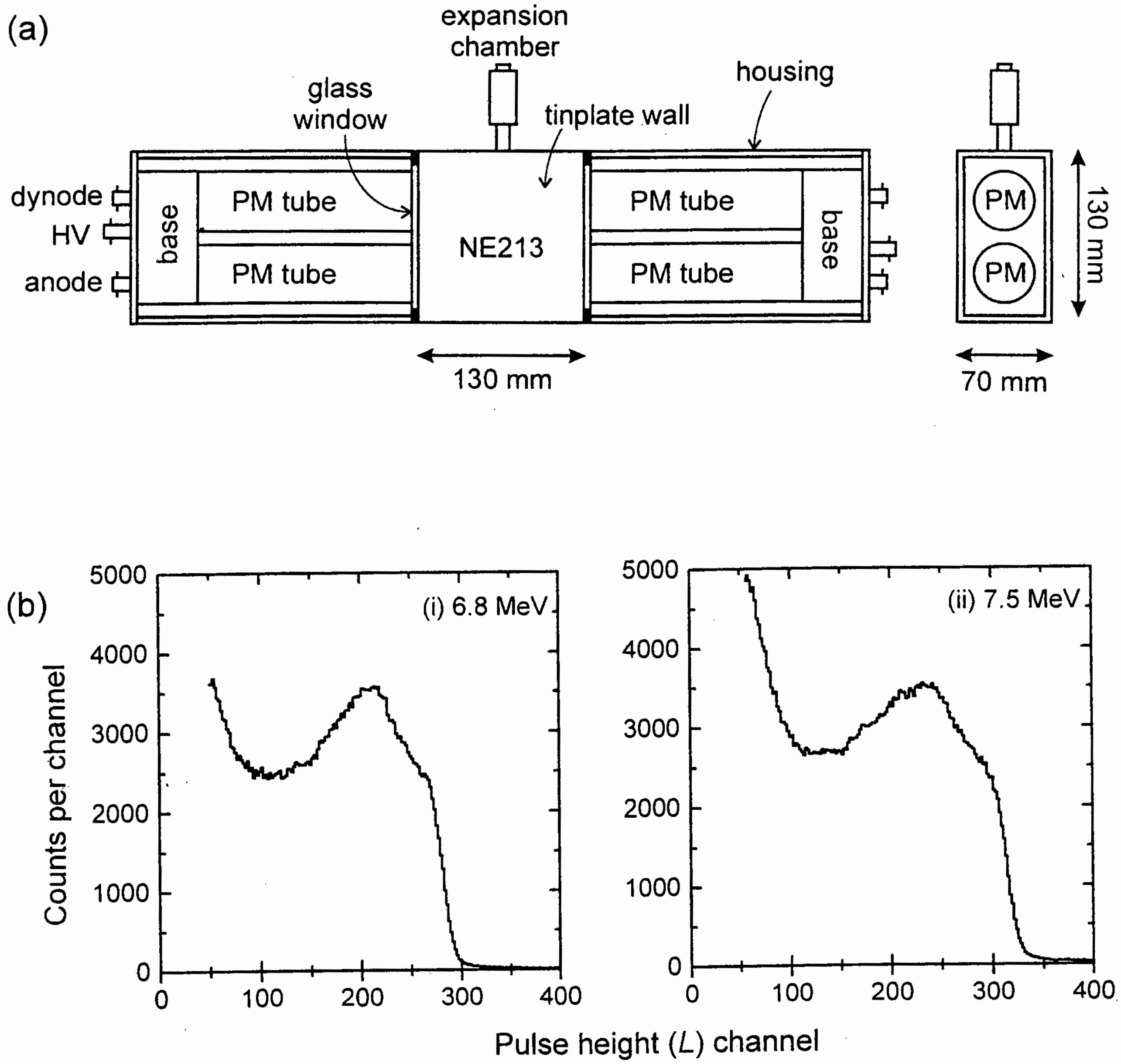

Figure 5-2 (a) Schematic diagram of detector C. The two glass windows of the NE213 cell of dimensions 13 cm × 13 cm × 7 cm are each optically coupled to two RCA-8850 photomultipliers. Outputs from the four photomultipliers anodes are coupled together and fed to a single LINK PSD unit.

(b) Lineshapes measured by detector C for neutrons of energy (i) 6.8 MeV and (ii) 7.5 MeV. Events associated with the detection of neutrons in detector C were separated from γ-ray events by pulse shape discrimination

5.2 Single scattering samples

5.2.1 L–T_n distributions for HCNO scattering

Figures 5-3 to 5-5 show plots of event density as a function of parameters L and T_n, measured by detectors B (150°) and C (45°), for the graphite, liquid nitrogen and water scattering samples, and for an empty sample container and the empty Dewar mounted at P_0. The data in these figures have been normalized to the same number of incident neutrons as monitored by detector M, and the T_n-scale in each figure represents 1.43 ns/channel. A number of features of neutron scattering important to FNSA are illustrated in figure 5-3 which shows counts as a function of parameters L and T_n, measured in detector B (figure 5-3 (a) and (b)) and detector C (figure 5-3 (c) and (d)) for neutrons scattered elastically and inelastically from the graphite sample. Events attributed to elastic scattering form a strong ridge at $T_n = 33$ in figure 5-3(a) and $T_n = 37$ in figure 5-3(b). Elastically scattered neutrons of incident energy 7.5 MeV arrive at detector B before those of incident energy 6.8 MeV, resulting in the observed shift in T_n. In addition, the upper pulse height edge of the elastic ridge stretches up to $L = 23$ at 6.8 MeV and $L = 27$ at 7.5 MeV, corresponding to elastically scattered neutrons of energies 4.96 MeV and 5.47 MeV, respectively. The elastic scattering yield measured at 150° is seen to be about four times greater at 7.5 MeV than at 6.8 MeV, as predicted by the differential cross section for $^{12}C(n,n)^{12}C$ (see figure 2-9). The low pulse height component at $T_n = 29$ in figure 5-3(b) is attributed to neutrons of incident energy 7.5 MeV which scatter inelastically, populating the 4.43 MeV level of ^{12}C, and arriving at B with energy 1.76 MeV. This peak is not visible in figure 5-3(a) since it falls below the pulse height threshold. The strong ridge present at $T_n = 50$ in figures 5-3(a) and (b) is a background component resulting mainly from neutrons transmitted through the shielding wall.

Important features may be also observed in the distributions measured by detector C (45°) at 6.8 MeV (figure 5-3(c)) and 7.5 MeV (figure 5-3(d)). The events associated with elastic scattering form the strong ridge at $T_n = 40$ at 6.8 MeV and $T_n = 46$ at 7.5 MeV. The elastic yield at 45° is similar at both incident energies, however the inelastic component is stronger at 6.8 MeV ($T_n = 17$) than at 7.5 MeV ($T_n = 28$). The inelastic component is also better separated from the elastic component at 6.8 MeV due to the longer neutron flight times at the lower energy. It is evident from figure 5-3 that the ratios of the forward-to-background scattering yields are different for the elastic and inelastic components measured at 6.8 MeV and 7.5 MeV.

Figure 5-4 shows L–T_n distributions measured at 7.5 MeV for the empty sample container by (a) detector B at 150° and (b) detector C at 45°. The important features present in figure 5-4(a) are ridge at $T_n = 50$ attributed mainly to neutrons transmitted through the shielding, and the low pulse height time-independent component present at all T_n, arising from neutrons scattered from the general environment. The background measured by detector C displays a broad distribution at $T_n < 54$, together with a low pulse height component at all T_n. The differences in the background distributions measured by detectors B and C are attributed to their different volumes, geometries and positions.

Figure 5-4 also shows L–T_n distributions of the scattering yield measured at 7.5 MeV for the water sample by (c) detector B and (d) detector C. The edge of the elastic scattering ridge (T_n =37) stretches up to L = 31 (5.90 MeV) for oxygen while only to L = 28 (5.47 MeV) for carbon (figure 5-3(b)) as expected from the kinematics of elastic scattering. Furthermore, a strong component is observed in the distribution measured for water at 45°, marked by the arrow H in figure 5-4(d), arising from the neutrons scattered from the hydrogen in the water. The arrow L_H shows the maximum pulse height that is observed for this hydrogen ridge, at this laboratory angle and incident neutron energy. The T_n and L coordinates of the hydrogen ridge are governed by the kinematics of n-p elastic scattering, which reduce the scattered neutron energy to half the incident neutron energy at this detector angle. A strong hydrogen component will be present in distributions measured for all hydrogen-rich materials, and is generally separated in time from both the elastic and inelastic scattering components of all other elements, situated between these two components on the L–T_n plane. The presence of hydrogen in the scatterer contributes nothing (in first order) to the spectrum recorded by the detectors at backward angles (e.g. figure 5-4(c)) since neutrons from n-p elastic scattering are kinematically confined to forward angles.

Figures 5-5(a) and (b) show L–T_n scattering distributions measured at 7.5 MeV for liquid nitrogen in a 10 cm diameter Dewar flask. The upper pulse height edge of the elastic component measured at 150° ($T_n = 37$ in figure 5-5(a)) stretches to a pulse height channel between the edges of the carbon (figure 5-3(b)) and oxygen (figure 5-4(c)) elastic components. A weak component is present at T_n = 32 in figure 5-5(a) and at T_n = 32 in figure 5-5(b) attributed to inelastic scattering from the low levels of ^{14}N. Figures 5-5(c) and (d) show the L-T_n distributions measured by detectors B and C, respectively, for the empty Dewar flask. The narrow ridges which are resolved in figure 5-5(c) at T_n = 33 and $T_n = 38$ are attributed to neutrons scattering from the front and back faces of the 10 cm diameter Dewar. The component centred at T_n = 26 in figure 5-5(d) is ascribed to neutrons inelastically scattered from the silicon nuclides in the glass Dewar.